

AD-A131 175

DEVELOPMENT AND EXPLORATION OF THE CORE-CORONA MODEL OF  
IMPLoding PLASMA LOADS(U) JAYCOR ALEXANDRIA VA  
J GUILLORY ET AL . 01 JUL 80 JAYCOR-TPD-200-80-001-DFR

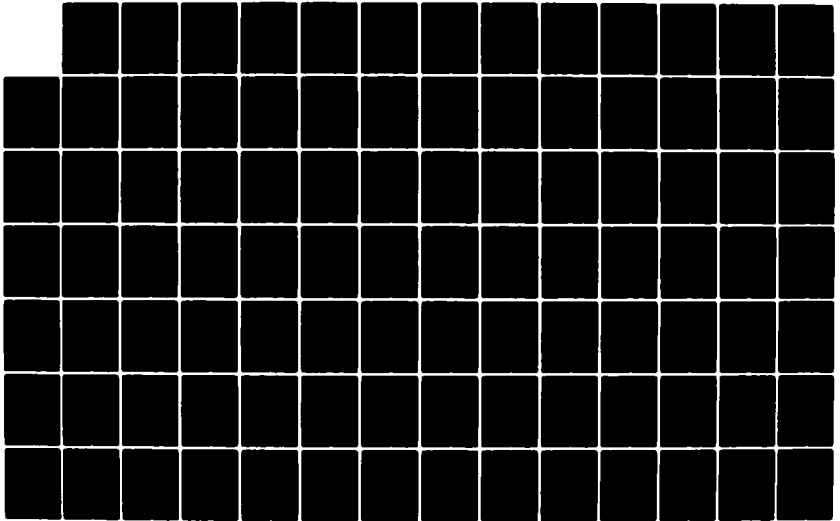
1/2

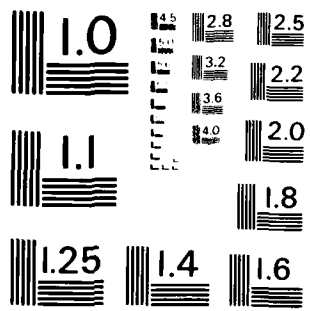
UNCLASSIFIED

DNA-5234F DNA001-79-C-0189

F/G 18/3

NL





MICROCOPY RESOLUTION TEST CHART  
NATIONAL BUREAU OF STANDARDS-1963-A

AD-E 301181

12

DNA 5234F

ADA 131175

# DEVELOPMENT AND EXPLORATION OF THE CORE-CORONA MODEL OF IMPLODING PLASMA LOADS

JAYCOR  
205 South Whiting Street  
Alexandria, Virginia 22314

1 July 1980

Final Report for Period 5 February 1979-5 March 1980

CONTRACT No. DNA 001-79-C-0189

APPROVED FOR PUBLIC RELEASE;  
DISTRIBUTION UNLIMITED.

DTIC FILE COPY

THIS WORK WAS SPONSORED BY THE DEFENSE NUCLEAR AGENCY  
UNDER RDT&E RMSS CODE B323079464 T99QAXLA01470 H2590D

Prepared for  
Director  
DEFENSE NUCLEAR AGENCY  
Washington, DC 20305

DTIC  
ELECTE  
AUG 8 1983  
S B

83 06 29 108

Destroy this report when it is no longer  
needed. Do not return to sender.

PLEASE NOTIFY THE DEFENSE NUCLEAR AGENCY,  
ATTN: STTI, WASHINGTON, D.C. 20305, IF  
YOUR ADDRESS IS INCORRECT, IF YOU WISH TO  
BE DELETED FROM THE DISTRIBUTION LIST, OR  
IF THE ADDRESSEE IS NO LONGER EMPLOYED BY  
YOUR ORGANIZATION.





UNCLASSIFIED

SECURITY CLASSIFICATION OF THIS PAGE (When Data Entered)

20. ABSTRACT (Continued)

tures with an order-of-magnitude accuracy. With the inclusion of the improved opacity model, very appropriate radiation pulsewidths and amplitudes are also produced, first by the zero-D model and code and now by the 1-D version. The small, fast computer program also makes predictions concerning the time-dependent current partition between core and corona.

UNCLASSIFIED

SECURITY CLASSIFICATION OF THIS PAGE (When Data Entered)

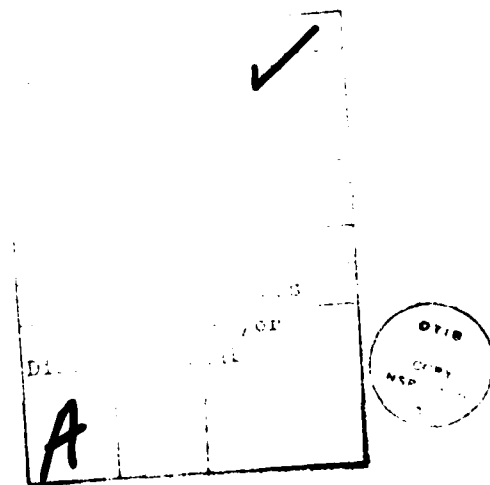
## TABLE OF CONTENTS

<u>Section</u>	<u>Page</u>
LIST OF ILLUSTRATIONS	3
I. OVERVIEW OF CONTRACT EFFORT AND RESULTS	5
A. Program Overview Directions and Objectives	5
B. Relation to Past Work	8
C. Principal Tasks	10
D. Summary of Results	12
E. Caveats	17
F. Relation to Other Analyses	19
1. PI	20
2. Maxwell	22
3. NRL (Mosher) Scaling	23
4. $S^3$	24
5. SAI	25
II. STARTING POINT: QUASI-STATIC CORE-CORONA EQUATIONS	27
A. Core Equations	27
B. Original Radiation Emission Model	30
C. Corona Equations	31
D. Coronal Temperature and Electron Deposition in the Core	33
III. MODIFICATION AND EXPLORATION OF THE ZERO-D CORE-CORONA MODEL	35
A. Equations Determining Coronal Parameters	36
B. Original Quasi-Static Code	38
C. Explicitly Time-Dependent Model	40
D. Self-Consistency of the Model Assumptions	50
E. Explicitly Time-Dependent Code Results and Evaluation	52

	<u>Page</u>
IV. SELF-SIMILAR 1D CORE-CORONA CALCULATION	55
A. Mathematical Model for Self-Similar Core Compression	59
1. Basic Requirements	59
2. Application to Strictly Radial Geometry	65
3. Modifications to the Core-Corona Energy Exchanges	72
B. Improvements in Radiation Modeling	74
C. Time-Dependent Self-Similar Code SPLAT	75
1. Operation and Structure of SPLAT	75
2. Description of Subroutines and Functions	82
3. SPLAT Program Flow	90
4. Advantages and Disadvantages	94
V. SCALING AND GUIDELINES BASED ON CORE-CORONA MODEL AND CODES	95
A. Interpretation of Code Results	95
1. Initial Conditions	95
2. Classes of Implosion Trajectories	96
3. Illustrations of the Dynamics	99
4. General Comparison of Zero-D and 1D Formulations	105
B. Analytic Modeling for Scaling Laws	107
1. Collapse Phase Models	108
2. Simplified Assembly Model	109
3. Radiation Scaling Model	115
REFERENCES	118

## LIST OF ILLUSTRATIONS

<u>Figure</u>		<u>Page</u>
1	Evolution of the Implicit- $T_2$ Model	39
2a	Annulus Evolution and Radiated Power in the Explicit- $T_2$ Model	53
2b	Thermodynamic Variables and Circuit Response	54
3a,b	Two "Initial" Ion Density Profiles for Different SPLAT-1D Code Runs	97
4a	Simple Collapse (SC) Evolution of $r_i$ , $r_m$ , $b$ , $I$ , and $P_{rad}$ .	100
4b	Pause-and-Collapse (PC) Evolution of $r_i$ , $r_m$ , $b$ , $I$ , and $P_{rad}$ .	101
5.	Generator Voltage vs Time for $\alpha = 1.2$	103
6.	Frequency-Integrated Radiative Yield vs Generator Rise-Rate Multiplier $\alpha$ .	104



*Handwritten scribble*

## I. OVERVIEW OF CONTRACT EFFORT AND RESULTS

### A. Program Overview, Directions and Objectives

This program has as its primary objective the quantitative exploration and generalization of the core-corona model of imploding plasma load dynamics (Refs. 1, 2), in close collaboration with radiation physics and modeling work ongoing at NRL (Refs. 3-8).

As a qualitative summary, one may say that the core-corona model arises from four physical considerations, all interrelated. The first assumption is that of a sharp density falloff in the outer regions of the annular plasma load. The transition region between the dense core plasma and the halo of corona plasma surrounding it is associated with a change from classical to anomalous resistivity, due to the onset of marginally stable microturbulence in the low density corona plasma. The modes comprising the turbulence are driven unstable by the electric field (i.e., the generator voltage) which attempts to drive the electron drift speed above a threshold value, but the resulting current is held to a marginally stable intensity by the enhanced resistivity which results from the instability. The model invokes current-driven ion acoustic turbulence for this mechanism. The instability sets in once the current-induced drift speed exceeds the coronal sound speed ( $v_{d,e} > c_s$ ), and it develops quickly to a nonlinear stage of ion acoustic turbulence. The constraint of constant current density across the core-corona boundary implies a tendency for the outer plasma to heat. The ohmic dissipation is nearly constant or slightly enhanced due to greater resistivity, but the radiative losses fall due to the density drop. Such a picture is physically sensible due to the large axial electric fields in wire plasma generators, which can quickly excite a tenuous outer plasma to instability in the earliest phases of the implosion.

The second assumption is that the high-density annular wire/plasma core stops a penetrating coronal electron in distances short compared to the core dimensions, so that the coronal heating can couple to the core and soften the implosion. However, it is important to note that coronal electrons will not tend to execute straight orbits into the core, due to the large magnetic fields in the current carrying zone on the core surface. Previous decoupling energy estimates (Ref. 1), based on a simple test particle picture, may be too pessimistic and criteria taking the magnetic fields into account have now been included.

A third ingredient in the core/corona equations is an isothermal corona, and for this one must assume the corona to be sufficiently limited in space that equilibration to an isothermal pressure balance can be established rapidly as the core annulus implodes. The corona continuously re-establishes its pressure balance as the transition interface moves inward. This requires the coronal scale height  $r_0(T_2)$  to be such that  $r_0(T_2)/c_s(T_2) \ll \tau_{imp}$ , with  $c_s$  the sound speed at  $T_2$ , the coronal electron temperature, and  $\tau_{imp}$  a time scale characteristic of the implosion process. When disturbances moving at the local sound speed can traverse the corona quickly, the pressure balance maintains a vanishing coronal radial velocity field, and turbulent or classical relaxation processes can maintain an isothermal system.

The final constraint in the original core-corona model equations was that of quasi-static heat balance between

ohmic heating in the corona,  
net deposition of hot electron energy into the core, and  
coronal radiative losses

Under the present program, this constraint has been relaxed. The quasi-static requirement has now been removed by generalizing the original equations, because it was found that during the collapse phase the heat transfer from core to corona was too rapid to allow the quasi-static determination of coronal temperature. In addition, the flux of energy from the core to the corona has been included, because as the collapse occurs this flux becomes important; and opacity functions have been used to better describe the radiative losses. Corona radiative loss is included although it is usually a small effect on the energy balance. The detailed physics of these upgrades and their improvement of the quantitative modeling of the system are discussed in the Sections III, IV, and V of this report.

The interrelations among these four assumptions, as relaxed in the present work, represent time-dependent tests of the model's viability. The model has shown some ability to predict the collapse radii and temperatures with a gratifying order-of-magnitude accuracy. With the inclusion of the improved opacity model, very appropriate radiation pulsewidths and amplitudes are also produced, first by the zero-D model and code and now by the 1-D version. The small, fast computer program also makes predictions concerning the time-dependent current partition between core and corona.

Scaling laws are presently under development with the assistance of this code. These will provide design optimization information and information on the limitations of such radiation sources.

## B. Relation to Past Work

The JAYCOR theoretical program in support of the NRL exploding wire effort has provided very significant new directions in which to seek quantitative explanation of the wire array radiation pulse and scaling, and quantitative models of some of these new phenomena are now being developed and tested under the program. In its first stage, as an NRL subcontract, the program provided preliminary descriptions of two important new physical processes which had not been considered in previous attempts to model the radiation output: the siphoning-off of current to a low-density hot corona during peak compression, and the possibility of diode-region behavior at necked-off constrictions in the assembled plasma. Both of these new physical elements have the potential to significantly revise the earlier theoretical modeling of the radiation from the assembled plasma.

In its more recent stage, as a JAYCOR program funded by DNA, the emphasis is on exploring the coronal effects, developing and using analytic modeling and a small computer code (an order of magnitude smaller and faster than the existing MHD code, which does not treat the corona). In this stage of the program, there is an unprecedented and very successful close interaction between the NRL and JAYCOR physicists. This quantitative exploration of the Tidman-Colombant core-corona model has already brought to light the sensitivity of the model's output to the time development of coronal temperature and to the opacity model used to describe the core radiation. Thus, the plasma and radiation physics are being integrated in a way that seems to hold considerable promise for finally understanding the radiation pulse time-scale and scaling with experimental observables.

This report describes the logic and some of the output of this work. Starting from the Tidman-Colombant equations of the core-corona model (Ref. 1), these equations were generalized and solved iteratively. When this procedure frequently failed to give solutions, the equations were further generalized to account dynamically (rather than implicitly) for the time dependence of the coronal temperature and ionization state. This is the stage at which results were reported in the semi-annual report (Ref. 2). When this zero-dimensional treatment was observed to give anomalously high coronal temperatures because mass flow into the corona could not be properly included (Ref. 2), it was generalized further to include a one-dimensional (radial) grid of density  $n(r)$  in the core, which was advanced in a simple Lagrangian fashion using a local self-similarity law discussed in Section IV of this report. This allows a consistent treatment of particle flow from core to corona, which keeps coronal temperatures at reasonable values and prevents unphysical explosive expansion of the corona to large spatial extent.

This important physical improvement, however, was achieved at the expense of certain new headaches of code design that are inherent in dealing with the localized forces and compressions essential to a 1-D model. For example, the code now successfully damps round-off induced ringing of coronal current and temperature, and treats in a simple but useful way the transition from locally self-similar implosion to assembly on the axis. The 1-D code still gives slightly shorter higher-power radiation pulses than the experiments, but we believe that this results from axial dependence of the fields in the experimental geometries, and consequent time-delay of the compression at increasing distances from the cathode, features not shared by the mathematical model.

As improved computation of K and L shell radiative yields and opacities have become available from the NRL group (Refs. 6-8 and subsequent work), we have incorporated these via analytical fitting functions good to better than 10%.

Finally, using the explicit spatial structure in  $n(r,t)$ , one can calculate more precisely the expected radiative losses from the plasma. The linkage of this model to radiation transfer codes presently operating at NRL is then a relatively simple matter and is already underway. Since our experience has demonstrated the extremely tight coupling between the evolution of the radiative energy losses and the evolution of the plasma, the use of more precise radiative transport and ionization dynamics is crucial to any serious evaluation of the model's utility.

#### C. Principal Tasks

This program has as its primary objective the quantitative exploration and generalization of the core-corona model of imploding plasma-load dynamics (Ref. 1), in close collaboration with radiation physics and modeling work ongoing at NRL.

Its principal tasks have been:

- Investigation of the conditions of validity of the original quasi-adiabatic core-corona equilibrium relations.
- Examination and modification of the core-corona energy transfer equation and the generator-plasma coupling equations.

- Development of a code using those relations to test quasi-equilibrium.
- Generalization to an explicitly time-dependent code to describe the more general problem where the original equations were inapplicable.
- Incorporation of the improved modeling of radiation and radiation escape.
- Further improvement and generalization to correct an unphysical excessive coronal heating. As implemented, this involved generalizing the code to allow a radial density profile, advanced in a "locally self-similar" way on a Lagrangian grid.
- Exercising the code(s) to observe their advantages, limitations, and physical implications.
- Derivation of heuristic scaling laws based on the computations (yield and timescales vs. generator parameters and initial conditions).
- Use of computational results as guidelines for simple analytic approximations and modeling.
- Simultaneous derivation of simplified analytic models, to allow algebraic scaling laws governing the approximate dependence of yield and timescales on generator parameters and initial conditions.
- Maintaining close working contact with both radiation computation efforts and 1-D hydro code efforts (WHYRAC, WHYRAD) at NRL.
- Presenting results and cataloging the behavior and caveats of the model(s).

Virtually all of these tasks stand accomplished. We note, however, that we are still not satisfied that the behavior of the codes represent actual physical consequences, and scrutiny and testing of the code will be continuing under the 1980 funding.

D. Summary of Results

This section provides a summary of our conclusions from coordinated analytic and computational development over the past twelve months. Where indicated, some of these conclusions are tentative (See the following Section E on caveats). Many follow from the fundamental physics of the problem and are on rather more secure ground. But we hesitate to apply our quantitative scaling laws based on the code behavior to present experiments, because of the axial time-dependence of the compressions observed in those experiments.

We wish to highlight the following conclusions:

- The quasistatic approximation (Ref. 1) for describing the coronal temperature tends to fail upon plasma assembly. The explicitly time-dependent treatment (Sec. III) is more useful.
- A single short radiation pulse is observed, over a timescale apparently equal to the sum of the assembly time and the radiative cooling time at peak density. The assembly timescale depends on the thickness of the annular plasma core and its peak collapse speed.
- A tenuous, extended corona surrounding the bulk of the collapsing plasma may reduce peak collapse velocities slightly by removing

some of the  $J \times B$  force to larger radii, and the force reduction may quickly increase on assembly if the core heats the corona. This reduces the magnitude of the "notch" in the total current.

- On the other hand, a more dense corona of smaller spatial extent may rob an appreciable fraction of the  $J \times B$  force throughout the implosion, i.e., the coronal current may in this case be an appreciable fraction of the total current at all times. This can occur if current is excluded from most of the core plasma by its high conductivity.
- Implosion trajectories ( $r$ ,  $n$ ,  $T$ , etc. as functions of time) are observed which either bounce and collapse (BC), pause and collapse (PC) or simply collapse in a monotonic way (SC). With the removal of coronal overheating that resulted from the zero-D model, (and with the modified radiation package) the simulated plasma no longer bounces to large radii.
- There are preliminary indications that as the generator pulse timescale is shortened, the radiative energy yield first increases, and then decreases (See Figure 6). The decrease may be due to pre-compression of the plasma by the fast rising field, before assembly.
- For fast collapse speeds and low initial temperatures just prior to assembly, plasma momentum can drive the density to values for which the radiated power exceeds the input rate of energy from assembly. The plasma then cools rapidly once assembly is complete, and need not bounce appreciably.

- Two competing effects influence the extent of plasma bounce after collapse: high implosion velocities tend to give more bounce for intermediate peak densities, but they also tend to drive peak densities higher, and thus increase the abrupt radiative energy loss that quenches the bounce.
- At the highest peak densities, the balance of line, recombination, and Bremsstrahlung radiation shifts toward Bremsstrahlung because of excited-state quenching.
- "Refrigerative" collapse to near-solid densities and low temperatures is probably a real physical phenomena, insofar as a second pulse of low-temperature radiation often cools the plasma until its density reaches condensation values.
- Since diode impedances usually hold up after plasma assembly, the behavior of the diode current after assembly should be quite different depending on whether the plasma coalesces uniformly or in beads along the axis. (Such problems will be considered during the 1980 effort.)
- The calculation of particle flux from core to corona was improved so as to be consistent with the energy flux  $Q_{12}$ . As a result of this correction, the coronal temperature  $T_2$  remains at more reasonable values (a few KeV), and the coronal current fraction  $1 - \beta$  tends to be lower for given initial profiles. This in turn acts in the direction of shortening the collapse time and in-

creasing the final collapse velocities. Only larger and/or denser coronas can slow the collapse appreciably by robbing the core of JxB force. With the coronal electron temperatures thus lowered, we do not see the coronal blowoff ("exploding corona") observed in earlier code runs.

Collisional quenching of the line radiation at high density ( $n_I \sim 10^{21} \text{ cm}^{-3}$ ) is now included in an approximate way. The quenching at these densities is assumed to be so rapid that above a critical density of order  $10^{22}$  no line radiation is emitted. Continuum radiation is assumed blackbody-limited at the highest densities and a continuum opacity estimate is inserted at intermediate densities. Especially for the higher final collapse velocities, the compressed density exhibited by the code can eventually reach the critical value in a large fraction of the core, so that in this approximation late-time line radiation is emitted only from an outer layer of the core, and in lesser amounts from the (hotter) corona. As the outer regions of core plasma collapse onto this blackbody central region, they accrete as they radiate their energy. This may help explain the discrepancy between certain simple scaling laws based on full-volume radiating arrays (Ref. 5) and observed experimental trends (Refs. 6, 7). Line radiation leakage from the core with a finite rate would then combine with semi-transparent radiation escape from the diminishing envelope mass, with continuum radiation, and

with frequency-dependent opacity effects, to give the final radiation pulse profile.

Further light will be shed on this question as the self-consistent radiation/ionization model of Duston et al (under development) is tested and incorporated into the SPLAT code, but the most recent runs with the present radiation package indicate that:

- (1) Continuum radiation, because it escapes, contributes an appreciable part of the radiation.
- (2) The rise time of the radiation pulse is governed by the implosion velocity upon collapse.

We also emphasize that motional effects allowing greater escape of line radiation have not yet been included in the SPLAT-1D Code. The inclusion of these effects, however, would only increase the tendency of radiative collapse and cooling.

The tendency of the assembled plasma to reach high densities ( $\approx 10^{20} \text{ cm}^{-3}$ ), cool rapidly by radiation, and have negligible energy remaining for bounce or radiation thereafter, provides a more physical interpretation of the singular "refrigerative collapse" idealization (Ref. 18). The actual "collapse" may often be delayed by collisional quenching, which stores energy in thermal energy and allows it to be radiated away only at the continuum rate. Motional broadening would tend to restore some of the otherwise-trapped line radiation, but probably cannot greatly affect the collisional quenching.

### E. Caveats

We caution that the modeling described in this report is still in its developmental stages and is continuing under the 1980 funding, alongside investigations of noncylindrical behavior.

It is also possible that another physical mechanism must be found to account for the diversion of some of the JxB work either into plasma thermal energy rather than implosion kinetic energy, or into kinetic energy of the outer layers of plasma, delayed somehow in their arrival on axis.

Since the classical viscous stress on the fluid core can only restructure the radial momentum density into a preferred profile resembling the locally self-similar solutions discussed in Section IV, the use of classical viscous behavior to slow the speed of implosion is a self-limiting process. In order to directly store momentum imparted by surface forces one must create a steep gradient in the radial flow field  $V_r(r,t)$ . This will generate a very unstable situation and may even force multi-streaming within the fluid, which will in turn produce an enhancement of the effective viscosity coefficient and redistribute the momentum over the entire core plasma. Once redistributed, this momentum sets the implosion speed of the entire core plasma. In calculating the implosion speed using the present model, which assumes an infinitely fast redistribution of the momentum density, one has already anticipated the end result of the dissipative process detailed above. The result is that given surface forces can never produce a slower

core implosion (than that presently calculated) unless momentum density is allowed to build up in the outer layers of the plasma and remain there on a time scale characteristic of the entire run-in phase. Even a modest classical viscosity would force a significant redistribution of this momentum, to say nothing of the effects of multistreaming.

On the other hand, if a second degree of freedom were excited in any attempt to induce radial motion, then the momentum imparted to this additional mode would represent momentum unavailable to the radial motion, and the general speed of implosion would be reduced for any time history of the external driving fields. A good possibility for such a second degree of freedom, and one which we propose to explore through drift-kinetic theory, is the excitation of vortex streets or convective cells in the  $(r,z)$  plane. Convective instabilities are known to exist for field geometries similar to those of Z-pinch plasmas (Refs. 16, 17), and there is good reason to believe that the strongly magnetized electron fluid in the outer regions of the core could be excited into a vortex street layer by radial E-fields arising as electrons respond to local  $J \times B$  forces and drag the ions behind. Such a coupling of radial accelerations and vortex excitation would diminish the radial momentum transferred to the denser core regions and slow the implosion directly. Subsequent dissipation of the vortex motion would act as a late contribution to the thermal energy and participate in lengthening the radiation pulse.

If such motion is favored in these systems, the impact on the radiation pulse length could be significant. In the present core/corona model the pulse width is a very sensitive function of the implosion velocity. In general, all mechanisms which tend to lower the implosion speed will also lengthen the radiation pulse, weaken the current notch, and produce the peak radiation from a cooler, less dense plasma.

The 1-D locally self-similar code gives bounce dynamics in much better qualitative agreement with experiment than the zero-D code. At the high densities achieved in the simulated plasma assembly after the main radiation pulse, the continuum alone could (without opacity) radiate away sufficient energy to abolish or greatly reduce the magnitude of the bounce.

#### F. Relation to Other Analysis

In the past year, some analyses of imploding plasma radiation sources have been, and are being carried on independently at other laboratories.

Physics International (PI), Maxwell Laboratories (MLI), the Naval Research Laboratory (NRL), Systems Science, and Software (S<sup>3</sup>), and Science Applications, Inc. (SAI) have all produced relevant papers on various aspects of the implosion and radiation modeling. In this section of our overview, we give brief comparisons of some of these analyses with our own (which is discussed more fully in Section II through V below).

### 1. Relation to PI Analysis

The Theoretical effort at Physics International (Ref. 20) has involved heuristic scaling laws based on experimental results, optimization and scaling of the coupling of generator and plasma (without corona), and the 1-D Lagrangian MHD Code SM/RAD. A brief and necessarily partial summary is as follows: Experimentally, the radiative yields above about 1 keV seem to scale roughly with the square of the peak current (as expected since the peak implosion speed scales roughly as  $J \times B$ ), with lower values for gas puff loads than for wire loads (as expected because peak densities should probably be lower for the gas puffs).

To calculate a simple scaling of radiative yield, PI assumes:

- (i) a massive array with inductance constant during the current rise;
- (ii) that the circuit is crowbarred at peak current;
- (iii) that the final kinetic energy is the difference between inductively stored energy at peak current, and that at peak compression.
- (iv) that the radiated energy is the sum of the peak implosion kinetic energy and the inductive energy of the fields;

- (v) that the ratio of initial to final radii of the array is fixed independently of the machine parameters
- (vi) that the voltage pulse has a simple parabolic shape.

These assumptions give a scaling of the radiated energy  $\epsilon_R$  as  $\bar{V}^2 t_r Z_g^{-1} R(b)$  where  $b \equiv 2\mu_0 \ln(r_o/r_f)(Z_g t_r)^{-1}$  and  $R(b)$  rises from about 0.6 to  $b = 0$  to saturation at  $R = 1.3$  when  $b > 2$ ; i.e.,  $R(b)$  is roughly proportional to  $Z_g^{-1}$  until  $Z_g$  drops below some critical value. Here  $t_r$  is the generator voltage rise time and  $\bar{V}$  is the peak voltage.

The 1-D SM/RAD Code uses Braginskii transport coefficients and flux-limited thermal conductivity, but uses a variable multiplier on the electron-ion collision rate (usually set at 10 to 50 to give reasonable timescales). As does our own code, it starts from an ionized cylindrically symmetric plasma, and does not describe the early time history of the plasma formation. The arbitrary multiplier has the effect of making the resistivity of the entire plasma larger by an order of magnitude, and allowing complete penetration of the current into the (core) plasma. There is no coronal plasma. One difference then, is that our JxB force occurs more on the outside, while that in the PI 1-D Code is more distributed through the core plasma.

The results of the SM/RAD Code runs for an initial array radius of 0.5 cm indicate a bounce of most of the plasma mass out to about 0.2 cm after assembly, leaving low density on axis. By contrast, although the JAYCOR SPLAT code has a very crude collection algorithm for slowing the interpenetrating plasma streams on axis during assembly, the qualitative effect achieved is that of assembling the plasma at the axis rather than bouncing it off itself.

The SPLAT and SM/RAD Codes both appear to give very short assembly periods, on the order of 2ns.

## 2. Relation to Maxwell Analysis

In the work of Katzenstein (Ref. 7), a figure of merit is optimized over the field of parameters. The figure of merit is the ratio of  $d(KE)/dt$  at the end of the run-in phase to the power that the generator could supply to an impedance-matched load. The numerator is just the power dissipated by the motional impedance  $L$ . The report does not deal directly with the magnitude or time scale of the radiation pulse at peak compression, nor does it predict the dynamics and timescale of core-plasma assembly at the axis. The ohmic resistance of the load is neglected in comparison with the motional resistance resulting from time-varying inductance  $L$  during collapse, and the internal energy and pressure of the plasma during run-in are neglected compared to its kinetic energy. As in the present work, the plasma is assumed to be cylindrically symmetric and roughly uniform axially, and the voltage  $V_g(t)$  across the plasma is taken as given.

Both the usual Z-pinch geometry and a  $\Theta$ -pinch geometry were considered in the Maxwell analysis.

By comparison, the present report focuses in more detail on the physical processes in the usual Z-pinch mode and does not consider the  $\Theta$ -pinch mode. It concentrates on the effects of the corona of plasma surrounding the dense plasma implosion: robbing the core plasma of its current and its thermal energy near peak compression, allowing a longer cooler radiation pulse from the dense core plasma and reducing the magnitude of the dip in total current at peak compression. The present work is not per se an optimization of the coupling of plasma load to generator, but provides the computational basis for direct optimization of radiation output and spectrum, without the intermediary of a figure of merit unrelated simply to radiation output. While the equations in the JAYCOR Code (developed under this Contract) are more involved and numerous than those of the Maxwell circuit analysis, the code is still much faster and simpler than the usual MHD Codes required to model the core dynamics, and provides the coupling of the coronal plasma effects, which cannot easily be modeled by MHD Codes.

### 3. Relation to Mosher Energetics Analysis

Mosher (Ref. 3) has made a useful analytic estimate of titanium K-line radiation as a function of the kinetic energy  $\epsilon_k$  of implosion (per unit length) just prior to collapse, the average radius  $\underline{a}$  of the imploded plasma, and the mass (per unit length)  $m$  of the load. Radiation is assumed "black-body" at temperatures below a critical value and optically thin above this value. The line radiation decreases monotonically with temperature above this critical temperature (about 50eV). There is no corona in the model.

K-line radiation, upon reaching 2.5keV, rises abruptly as a function of implosion kinetic energy above a threshold which depends on the ratio of kinetic-energy-thermalization power to peak radiated power. Conclusions include: advantage of decreased load mass and recommendation of longer pulse and implosion times.

In contrast, our present still-preliminary computational work appears to indicate that the time-integrated radiative yield has a maximum as the generator rise time is varied, first rising with increasing rise time as the peak implosion speed is increased, but then falling once the generator rise time is fast enough to heat the plasma earlier in the assembly phase and force its expansion before as high a density is achieved. The dynamics of the plasma motion in our code are purposely somewhat oversimplified and probably do not describe plasma density profiles very accurately, especially for very fast generator pulses, but those profiles are mostly unimportant to the radiative yield. The experimentally observed radiation pulses are still somewhat longer than those given by our code, but that corresponds well to the evidence of sequential compression of different axial points at different times.

#### 4. Systems, Science & Software

The S<sup>3</sup> group has been carrying out 2-D hydrodynamic modeling of imploding wire arrays (Ref. 10), as a result of their conclusion that 1-D modeling gives unrealistically high plasma densities and excessively short radiation pulses. The DELTA code is designed to provide accurate description of an angular sector of an imploding array, using a triangular grid and moving with arbitrary velocity. The code thus combines features of the Lagrangian (co-moving), and Eulerian (fixed grid) representations, and the equations of motion are thus

written with the nonlinear ( $V^2$ ) terms expressed as convolutions. An artificial viscosity is invoked to damp the large oscillations that would otherwise occur unstably in the code.

Although the code may be expensive to run for times comparable with the implosion time, it appears to be highly useful in describing the growth of important azimuthal asymmetries in the early phases of collapse (first 10 nanoseconds). These asymmetries then can be preserved and magnified during the remaining collapse, and are one strong candidate to account for the observed slower assembly times.

By contrast, the JAYCOR effort has been devoted to finding whether other mechanisms, such as the coronal blowoff plasma, could account for the observed slower assembly times. Our preliminary indication, still clouded somewhat by code difficulties, is that other processes besides the corona may be necessary, but there is no reason to assume anomalous resistivity in the bulk of the imploding plasma.

Other 2-D studies by S<sup>3</sup>, modeling the collapse of a cylindrical array of thin filaments, show the development of helical shape to the filaments, and there is little doubt that this mechanism can be active in a large number of observed shots. There appear also to be some shots not displaying obvious corkscrew geometry at assembly, and it was the JAYCOR mission to explore a possible model of their behavior, as affected by low-density current-carrying plasma blowoff, but not azimuthal perturbations.

## 5. SAI/NRL/JAYCOR

Bloomberg (SAI), Colombant (NRL), and Goldstein (JAYCOR) (Ref. 11), address (i) the early-time behavior of the plasma as the plasma current channels are established and the skin currents formed, (ii) the qualitative prediction of double-diode effects when axial beading of the assembled plasma occurs, and (iii) the original core-corona model.

We believe that each of these areas has a high probability of being important to the modeling of the implosion and radiation dynamics. The early-time development, although not yet described in adequate completeness, determines the 'initial' state of core/corona profile, current-carrying layer size, and thicknesses of core and coronal regions. These parameters then are important in selecting among the various classes of implosions and radiation trajectories, as discussed below in Section V. The present JAYCOR program, however, has not dealt with the early time history, but postulates reasonable outcomes as initial conditions to the modeling of the later-time behavior.

The formation of localized axial 'diode-like' gaps, with consequent axial acceleration of ions and electrons, is also a likely candidate to explain several important effects, and we will be carrying on a more detailed modeling to follow-up on this topic in the coming (1980) contract year. This report covers the first year of exploration, generalization, and testing of the core corona model discussed in (iii), and originally formulated in Ref. 1.

## II. STARTING POINT: QUASI-STATIC CORE-CORONA EQUATIONS (Ref. 1)

The full radial dynamics of imploding plasma loads is expensive to treat with 1D hydro-codes (such as the NRL axi-symmetric code WHYRAC) due to the high Alfvén and anomalous diffusion speeds that occur in the low density corona. But a simpler model was constructed by dividing the plasma into two idealized regions, namely the core (region 1) and corona (region 2).

### A. Core Equations.

The high-density core is treated as a spatially uniform-density fluid,  $\rho_1(t)$ , with classical plasma conductivity and Joule dissipation. The corona surrounds the core and consists of low density plasma driven by the axial field  $E_z$  in a marginal micro-instability state so that the electron axial drift velocity is approximately the sound speed in the corona. (The turbulence level in the corona adjusts to give an electron-wave scattering frequency,  $\nu_{ew}$ , for which this is true.) Further, the corona is assumed to adjust its structure on a time scale short compared to the dynamical evolution times of the implosion.

Although the B field diffuses rapidly through the turbulent corona, it diffuses relatively slowly into the classical core. The resulting partition of total current between core and corona is determined self-consistently, with the result that the coronal Joule dissipation can be larger than the core Joule dissipation. The coronal temperature  $T_2$  is, however, limited by micro-turbulent diffusion (thermal conduction). The radius  $a(t)$  is the boundary between these regions.

In region I ( $b \leq r \leq a$ ), one has the fluid velocity

$$V(r) = \frac{a\dot{a}}{r} + \frac{\dot{\rho}_1}{2\rho_1 r} (a^2 - r^2), \quad (1)$$

where  $\rho_1$  is the core density, and  $b$  is the inner radius of the core annulus. Various models for  $\dot{\rho}_1/2\rho_1$  are possible. We determine this quantity by the choice

$$\frac{d}{dt} (a - b) = c_1 \equiv \left( \frac{Z T_1}{A m_p} \right)^{1/2}. \quad (2)$$

This gives, in the core,

$$V(r) = \dot{a} \left( \frac{b}{r} + \frac{r}{a} \right) (1 + b/a)^{-1} + c_1 \frac{b}{a} \left( 1 - \frac{b^2}{a^2} \right)^{-1} \left( \frac{r}{a} - \frac{a}{r} \right), \quad (3a)$$

$$= A_1 r^{-1} + A_2 r \quad (\text{defining } A_1 \text{ and } A_2) \quad (3b)$$

which allows the annular shell thickness to expand at the sound speed during the run-in phase, but keeps the radial velocity of the inner edge,  $V(b)$ , finite at collapse on axis.

During the run-in phase ( $b \neq 0$ ), the force balance and energy equations of the core are

$$\begin{aligned} \frac{M}{(a^2 - b^2)} \frac{d}{dt} \left\{ A_1 \ln\left(\frac{a}{b}\right) + \frac{A_2}{2} (a^2 - b^2) \right\} &= -\pi p_2 + \frac{M}{(a^2 - b^2)} \left( \dot{a} c_1 - \frac{c_1^2}{2} \right) \\ &- \frac{2I_1^2}{c^2 (a^2 - r_i^2)^2} \left[ \frac{1}{2} (a^2 - r_i^2) - r_i^2 \ln\left(\frac{a}{r_i}\right) \right] \end{aligned} \quad (4)$$

and

$$\begin{aligned} \frac{3M}{2m_i} \frac{\partial}{\partial t} [Z_1 T_1 + \epsilon(Z_1)] = & - 2\pi p_e (aa - bb) + Q_{1,2} - P_{\text{rad}} \\ & + \frac{I_1^2}{\pi\sigma(a^2 - r_i^2)} + \frac{3M}{2m_i \tau_e} (T_I - T_1) \end{aligned} \quad (5)$$

$$\begin{aligned} \frac{3M}{2m_i} \frac{\partial T_I}{\partial t} = & - 2\pi p_I (aa - bb) - \frac{M}{m_i} \frac{\partial}{\partial t} \left[ A_1^2 \frac{2n a/b}{a^2 - b^2} + A_1 A_2 \right. \\ & \left. + \frac{1}{2} A_2^2 (a^2 + b^2) \right] - \frac{3MZ_1}{2m_i \tau_e} (T_I - T_1) \end{aligned} \quad (6)$$

where  $\sigma$  is the core conductivity

$T_1$  is the core electron temperature

$T_I$  is the core ion temperature

$\epsilon$  is the energy invested in ionization to degree  $Z_1$

$p_e, p_I$  are the core electron and ion pressures

$\tau_e$  is the electron cooling time,  $10^{12} A T_1^{3/2} / Z_1^2$

$M = \pi\sigma_1(a^2 - b^2)$  is the total shell mass/cm and (7)

$I_1$  is the total current flowing in the core.

The constants  $A_1$  and  $A_2$  are defined in Eq. (3b). It was assumed that the total core current  $I_1$  is uniformly distributed over a skin depth  $a - r_i$ , i.e.,

$$J = \frac{I_1}{\pi(a^2 - r_i^2)}, \quad B = \frac{2I_1(r^2 - r_i^2)}{rc(a^2 - r_i^2)}, \quad (8)$$

where

$$a \geq r \geq r_i = \max \begin{cases} b \\ a - \left(\frac{c t}{4\pi\sigma}\right)^{\frac{1}{2}} \end{cases} \quad (9)$$

Once the inner edge of the core annulus has reached the axis, one has  $b = 0$ ,  $\dot{b} = 0$ ,  $A_1 = 0$ , and  $A_2 = \dot{a}/a$ , so  $V = \dot{a}r/a$ . The momentum equation (4) then becomes

$$M\ddot{a} = -2\pi a(p_2 - p_1) - \frac{4I_1^2 a}{c^2(a^2 - r_i^2)^2} \left[ \frac{1}{2}(a^2 - r_i^2) - r_i^2 \ln\left(\frac{a}{r_i}\right) \right] \quad (10)$$

where now  $p(a) = p_2$  and  $p(0) = p_1$ .

#### B. Original Radiation Emission Model

The radiation emission term  $P_{\text{rad}}$  in Eq. (5) is in general a complicated function of the plasma parameters, geometry, and atomic species. For the production of radiation, Ref. 1 used an expression

$$P_{\text{rad}} = \pi(a^2 - b^2) (P_{\text{Br}} + P_{\text{rec}} + A_T P_\lambda)$$

where  $A_T$  is a temperature-dependent factor that accounts for reabsorption of the line radiation,  $P_\lambda$ . The Bremsstrahlung and continuum recombination radiation  $P_{\text{Br}}$  and  $P_{\text{rec}}$ , together with the average ion charge state  $Z$ , follow from expressions used in earlier work. Only a few dominant lines for the plasma atomic species in question were included in  $P_\lambda$ , e.g., averages over K and L shell lines for Al wires together with the opacity factor  $A_T$ , were provided by Davis and Jacobs (Ref. 4).

C. Corona Equations

Assuming  $T_e = T_2 \gg T_1$  the original equations for the quasi-static corona were

$$T_2 \frac{\partial n_e}{\partial r} = - \frac{1}{c} jB \quad (11)$$

$$j = \frac{c}{4\pi} \frac{1}{r} \frac{\partial}{\partial r} (rB) \quad (12)$$

where the current density  $j$  is along the  $z$  direction. The marginal instability current is

$$j = ec_s n_e \quad (13)$$

and the ion sound speed given by

$$c_s = \left( \frac{Z_2 T_2}{A m_p} \right)^{1/2} \quad (14)$$

for ions of atomic weight  $A$  and charge state  $Z_2(T)$  in the corona. These pressure balance equations can then be integrated. Defining the symbols

$I_2$  = total coronal current in amps

$I_1$  = total core current in amps

$T_2$  = coronal electron temperature in KeV

$A, Z_2$  = atomic weight and coronal ion charge state

$a$  = radius separating regions 1 and 2

$$c_s = 3.1 \cdot 10^7 (Z_2 T_2 / A)^{1/2} \text{ cm/sec}$$

$$\lambda_D = 2.35 \cdot 10^4 (T_2 / n_0)^{1/2} ,$$

the total coronal current, field and electron density distributions, and characteristic scale height  $r_0$  are given after some algebra as

$$I_2 = \frac{\Lambda^2}{[(2I_1 - I_B)^2 + 2\Lambda^2]^{1/2} + (2I_1 - I_B)} \quad (15)$$

with

$$\begin{cases} \Lambda = 1.4 \cdot 10^{-3} (a n_0 T_{\text{keV}})^{1/2} \text{ amps} \\ I_B = 6.45 \cdot 10^4 T_{\text{keV}} A / Z_2)^{1/2} \text{ amps,} \end{cases} \quad (16)$$

and

$$n_B = \frac{y_1 + y_2 \left(\frac{r}{r_0}\right)^\eta}{1 + \left(\frac{r}{r_0}\right)^\eta} , \quad (17)$$

$$n_e = \frac{2 x n_0 \left(\frac{r}{r_0}\right)^{\eta-2}}{1 + \left(\frac{r}{r_0}\right)^\eta} , \quad (18)$$

where

$$\eta = 2 \left\{ \left[ 3.1 \cdot 10^{-5} I_1 \left(\frac{Z_2}{A T_2}\right)^{1/2} - 1 \right]^2 + 9.65 \cdot 10^{-16} a^2 \left(\frac{Z_2 n_0}{A}\right) \right\}^{1/2}$$

$$x = 0.518 \times 10^{15} A \cdot \eta^2 / a^2 n_0 Z_2 \quad (19)$$

$$y_{1,2} = 6.45 \times 10^3 \left(\frac{T_2 A}{Z_2}\right)^{1/2} (-1 \pm \eta/2)$$

$$r_0 = a \left\{ x - 1 - \sqrt{x^2 - 2x} \right\}^{-1/\eta} = \text{coronal scale height.}$$

D. Coronal Temperature and Electron Deposition in the Core

The electron temperature required in the above formulas must be derived as an approximate solution to the energy equation. Having chosen the corona far enough out that radiation losses are small, we have

$$\frac{1}{r} \frac{\partial}{\partial r} (r q_{er}) = j E_z = - n_e c_s E_z \quad (20)$$

where  $q_{er}$  is the radial heat flux. Integrating radially this gives

$$I_2 E_z = 2\pi a q_{er} \equiv - Q_{12} \quad , \quad (21)$$

i.e., since the corona is quasi-static its total Joule heating is balanced by microturbulent diffusion of energetic electrons into the core. (It was assumed that these electrons have long mfp's compared with the core thickness,  $a-b$ , so that even though  $B$  is roughly laminar in the core they would drift and deposit their energy throughout the core region via collisions.) On this basis the radial heat flux in a corona of scale height  $r_0$  was then derived:

$$q_{er} \approx \frac{3}{2} n_e T_2 v_e \lambda_{ew} \left( 1 + \frac{\Omega_e}{v_{ew}} \right)^{-2} \quad , \quad (22)$$

with  $\Omega_e$  a typical value of the electron gyrofrequency  $eB(r)/mc$  in the core.

Thus an approximate expression for  $T_2$  was given as:

$$T_2 \approx \frac{2}{3} r_0 e E_z \left( 1 + \frac{\Omega_e}{v_{ew}} \right)^2 \quad . \quad (23)$$

(It turns out that during run-in the corona is unmagnetized, i.e.,  $v_{ew} > \Omega_e$ , but at assembly the reverse tends to be true.)

It must be noted that Eq. (23) is not really an explicit equation for  $T_2$  because  $r_0$  depends on  $n(n_0, a, T_2, I_1)$  and  $x(n_0, a, Z_2(T_2))$ , and  $\Omega_e/v_{ew}$  depends on  $n_0, a, T_2$  and  $I_1$ . Also, note in formulas (21) and (23) that  $E_z$  is independent of  $r$  in the corona. This follows from the quasi-static assumption for which  $\nabla \times \underline{E} \approx 0$ .

The  $q_{er}$  equation (Eq. (22)) has since been replaced by a more general expression, and  $T_2$ , the time-dependent corona temperature, is determined by a more general procedure than Eq. (21).

### III. MODIFICATION AND EXPLORATION OF THE ZERO-D CORE-CORONA MODEL

In the first quarter of the present contract several modifications to the original core-corona model were examined (Ref. 3) as a means to a more physical treatment of the energy transfer between the two regions. First, a different result for  $q_{12}$  was obtained by (i) assuming the transition region at  $r = a$  to be small compared to an electron "mean free path" in either the classical or turbulent region, and (ii) calculating the net heat flux across the boundary using a simple Krook model for the relaxation process in either region. The result above (Eq. 23) is an analogy to the classical heat flux obtained from a temperature gradient, but here the corona is isothermal and the correction to the heat flux must come from a treatment of the electron density gradient. When the Krook model is applied consistently in both regions, one finds.

$$q_{12} = \hat{r} (8\pi m_e)^{-1/2} \left\{ n_1 T_1^{3/2} - K n_2(a) T_2^{3/2} \right\} \quad (24)$$

$$\text{with } K \equiv 1 - \frac{5}{2} \pi^{1/2} \tau_{ew} v_{t2} (1 + \tau_{ew}^2 \Omega_2^2)^{-1} \left| \partial_r \ln n_2(r) \right|_{r=a} \quad (25)$$

The effective coupling to core parameters through the  $n_1 T_1^{3/2}$  term was previously neglected and represents the required heat flux of cooler core electrons which drift into the corona. The inward electron flux, the  $n_2(a) T_2^{3/2}$  term, reflects the lowest order correction from the perturbed coronal distribution function in the presence of a spatial gradient in number density and a local azimuthal magnetic field,  $\Omega_2$ .

Since the coronal radiation is small, a useful first approximation was to ignore radiation originating in the corona and require quasi-static energy balance, with almost all the coronal ohmic heating going into the core via

$$Q_{12} \equiv 2\pi a q_{12}:$$

$$E_z I (1 - \beta) = - Q_{12} = - 2\pi a (8\pi m_e)^{1/2} \left\{ n_1 T_1^{3/2} - K n_2(a) T_2^{3/2} \right\} \quad (26)$$

#### A. Equations Determining Coronal Parameters

In terms of the coronal shape parameters  $\eta$  and  $\delta$ , one can express  $|\partial_r \ln n_2(r)|_{r=a}$  as  $\frac{2}{a} \left[ 1 - \eta/2 + \eta/(1+\delta) \right]$ . If one chooses to measure  $T_1, T_2$  in keV,  $I$  in MA,  $E_z$  in MV/m,  $r_i$  and  $a$  in units of  $10^{-2}$  cm,  $n_1, n_2$  in units of  $10^{20}$   $\text{cm}^{-3}$ , then the Krook model correction factor  $K$  is

$$K(E_z, I, \beta) = 1 - \frac{2.07(Z/A)^{1/2} T_2 \left[ 1 - \eta/2 + \eta/(1+\delta) \right]}{a E_z \left[ 1 + 3.84 \times 10^4 (Z/A) I^2 \beta^2 T_2 / a^2 E_z^2 \right]} \quad (27)$$

The corona density at the boundary,  $n(a)$ , is given by

$$n_a = 8I / e\pi c_s (a^2 - r_i^2) \quad (28)$$

Defining

$$g \equiv (r_i/a)^2 \left[ 1 - (r_i/a)^2 \right]^{-1} \quad (29)$$

one can consider Eq. (26) an equation for  $\beta$ , the current fraction in the core. In terms of  $g$  and  $\beta$  we can write

$$\eta(g, \beta) = \frac{2}{1-\beta^2} \left\{ 1 + 4 g \beta + 2 (1 + 2g^2) \beta^2 + 4 g \beta^3 + \beta^4 \right\}^{1/2} \quad (30)$$

$$\delta(g, \beta) \equiv \left(\frac{r_0}{a}\right)^\eta = \frac{[1 - 2\beta - (1+2g)\beta^2 + (1 - \beta^2) \eta(\beta)]^2}{\beta(1-g)(1+g\beta)(1-\beta^2)} \quad (31)$$

Eq. (26) for  $\beta$  then takes the form

$$\beta = a_0 - a_1 \beta K(E_z, I, \beta) \left[\frac{1 - \beta^2}{1 + g\beta}\right]^2 \quad (32)$$

where  $a_0 \equiv 1 + (26.6 T_1^{3/2} n_1 a/E_z I)$ , and (33)

$$a_1 \equiv 4.09 \times 10^4 \frac{a(Z/A)^{1/2}}{(a^2 - r_i^2)} (I/E_z) \quad (34)$$

The relation (32) for  $\beta(T_2, g)$  can be inverted uniquely to give  $T_2(\beta, g)$ . With the units just defined for  $T_2$  and  $I$ , this gives

$$T_2 = 239 \left(\frac{I^2 Z}{A}\right) \left[\frac{1 - \beta^2}{1 + g\beta}\right]^2 \quad (35)$$

When there is a solution to (32) it can be obtained through iteration, by formally solving

$$\frac{1 - \beta^2}{1 + g\beta} = \zeta(\beta) \equiv \left(\frac{a_0 \beta^{-1} - 1}{a_1 K(E_z, I, \beta)}\right)^{1/2} \quad (36)$$

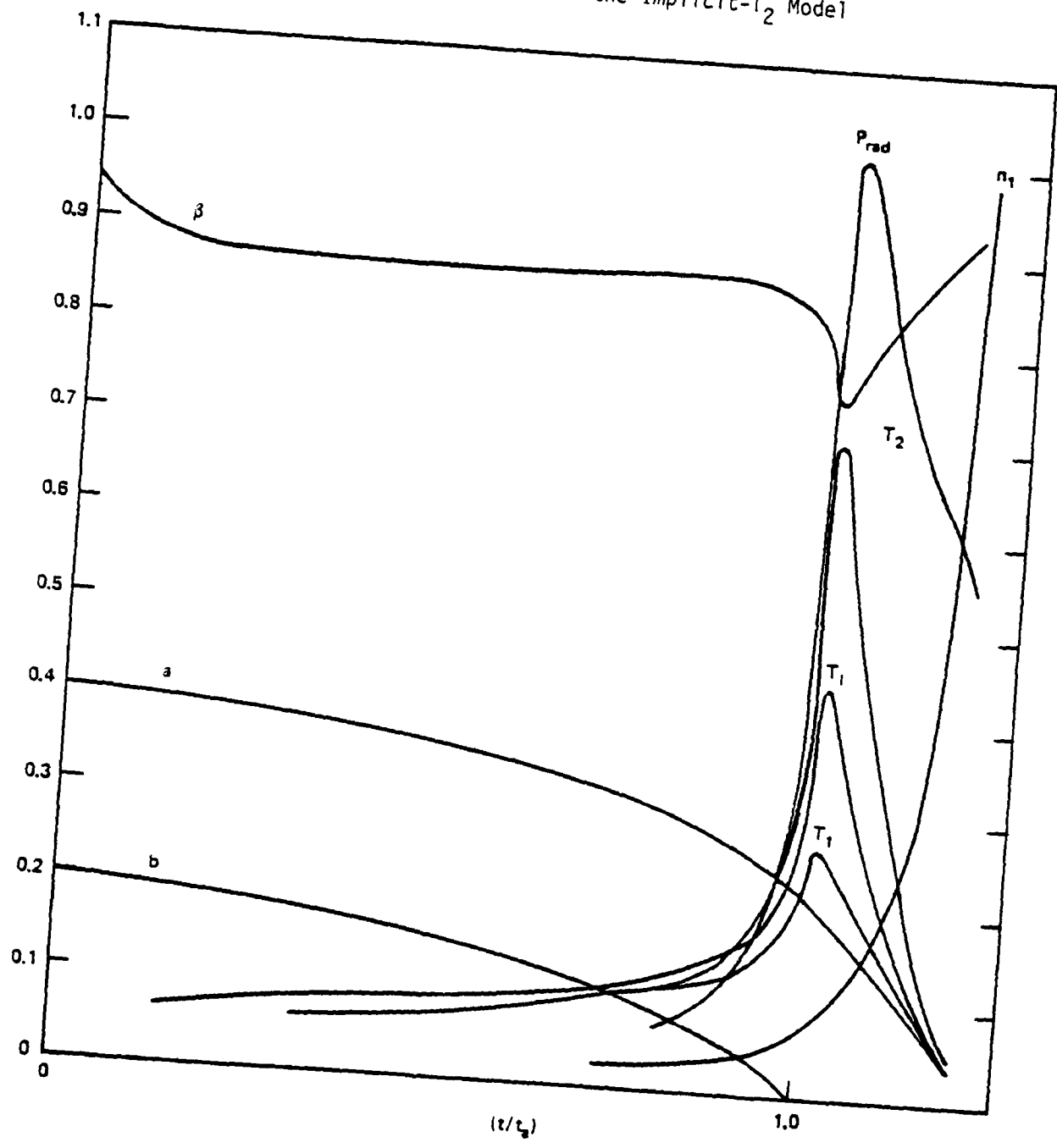
for  $\beta$ , as if  $\zeta$  was a constant, and then using the  $\beta$  value produced to re-evaluate  $\zeta(\beta)$ . Such a simple contraction technique will converge uniquely to the lowest  $T_2$  solution of (32) available, if a solution exists. A failure of the heat balance relation is signaled by the production of negative or complex  $\beta$  in the process of solving (36).

## B. Original Quasi-static Code

A quasi-static code was written to solve these pressure-balanced equations, coupled with Eqs. (4) - (10) for the kinematics and a radiation package for the core. But as the code development progressed, it became clear that such an implicit scheme for the calculation of corona temperature based on Eq. (26) was inadequate because corona heat balance tended to fail at peak compression. The primary source of this difficulty is the inclusion of the heat flux outward (from core to corona) in addition to the inward flux (from corona to core) originally used by Tidman and Colombant. In many cases this heating of the corona by the core is a significant contribution to the overall energy transport as the model plasma becomes more tightly pinched. When it is dominant, the corona has no effective channels for heat loss (its radiation output is small in general) and a quasi-static heat balance,  $(Z_2 \dot{T}_2 + \dot{Z}_2 T_2) = 0$ , cannot be obtained.

A typical time evolution of the model using the quasi-static  $T_2$  scheme is shown in Figure 1. The implosion is driven by the slow ramp in generator voltage and the time scale is in units of the assembly time, the time for the annulus to close. As the implosion proceeds,  $T_1$ , the ion temperature (taken identical in core and corona), becomes somewhat larger than the core electron temperature,  $T_1$ , and the corona electron temperature  $T_2$ , peaks near 14 keV. The current tends to decrease at or after assembly due to the strong impact of the implosion velocity on the effective inductance of the plasma. The most striking feature of this scenario is the sharp rise in plasma density that occurs after the short prepulse of radiation. It is this steep density rise that is responsible for the loss of heat balance and, in this case, also indicates a core plasma headed for a refrigerative collapse. The evolution of the current partition fraction  $\beta$  also indicates this collapse in that, after a sharp dip at  $t/t_a \sim 1$ , the current again accumulates in the core,

Fig. 1. Evolution of the Implicit- $T_2$  Model



increasing the inward magnetic force, while  $T_1$  (and the outward pressure) decays.

Such behavior is not seen in experiments, and an important test of this model is its capability to avoid a refrigerative collapse. Anomalous resistivity of the corona can be a physically plausible mechanism for softening the pinch, but only if the time sequence of heating is calculated properly. In a dynamic sense, one seeks corona behavior which will tend to rob the core of its current as the implosion progresses and thus weaken the forces driving the plasma inward. However, once the outward heat flux mentioned above enters the model, this property tends to be unattainable in the quasi-static model just when it is needed most, because of the constraint of quasi-static corona heat balance. For this reason the implicit  $-T_2$  scheme has been discarded and an explicit calculation of  $d(Z_2 T_2)/dt$  utilized instead. Such a modification has a significant impact upon the mathematical structure of the model, as discussed below, and upon its behavior as discussed in the following section.

### C. Explicitly Time-Dependent Model

The time evolution of corona electron energy  $Z_2 T_2$  can be calculated in a manner analogous to that used in treating this quantity within the core plasma. If the net heat flux from the core into the corona (per unit length) is denoted  $Q_{12}$  and the direct radiation originating from the optically thin corona is denoted  $P_{2,r}$  then one writes

$$\dot{U}_2 = IE_2(1 - \beta) + Q_{12} - P_{2,r} \quad (37)$$

as the rate of change for corona internal energy per unit length, when the net power loss or gain is calculated as shown on the right and distributed over the entire corona plasma. This simple form presumes that  $E_2$ , the average field

within the corona plasma, is not a function of radius, a constraint that will also be used in the circuit relation. Let  $N_2$  denote the total number of ions per unit length in the corona,  $Z_2$  the charge state. Then one has

$$\frac{d}{dt} (Z_2 T_2) = \frac{1}{N_2} \left\{ I(1-\beta) E_z + Q_{12} - P_{2,r} \right\}. \quad (38)$$

[In the implicit -  $T_2$  version of the model, this relation was replaced by the constraint  $\frac{d}{dt} (Z_2 T_2) \equiv 0$ .] The ingredients for the evaluation of Eq. (38) are determined by the nature of the corona pressure balance - specified uniquely by the parameters  $T_2$ ,  $I$ , and  $g = (r_i^2/a^2) (1-r_i^2/a^2)^{-1}$ .

$$\text{Defining } \alpha \equiv 2 c T_2 / e c_s \quad (39)$$

(with  $c_s$  the sound speed in the corona), and

$$\beta_0 \equiv \alpha / I, \quad (40)$$

we consider  $\beta$  as a function of  $g$  and  $\beta_0$ . Then  $\delta$  is given by

$$\delta = \frac{(\eta/2 + 1 - 2\beta/\beta_0)}{(\eta/2 + 2\beta/\beta_0 - 1)} \quad (41)$$

Here  $\eta$  is the exponent determining the rate of decay of density with increasing  $r$  in the corona, while  $\delta$  is the parameter determining the offset relative to  $r = a$  in the corona profile. In particular, the corona electron density profile is given by

$$n(r) = n_a \frac{(1 + \delta)^2 (r/a)^{\eta-2}}{[\delta + (r/a)^\eta]^2} \cdot n_a = \frac{I_1}{e \pi c_{s,2} (a^2 - r_i^2)} \quad (42)$$

Given  $Q_{12}$  as determined above, one need only calculate  $N_2$  and  $P_{r,2}$  using the proper corona profile in order to complete the evaluation of Eq. (38).

The total number  $N_2$  at fixed  $T_2$ ,  $I$ , and  $g$  is simply

$$N_2 \equiv 2\pi Z_2^{-1} \int_a^\infty dr r n(r) ,$$

i.e. 
$$N_2 = \frac{\pi a^2 n_a}{Z_2} \cdot \frac{2[1 + \delta]}{\eta} . \quad (43)$$

The coronal radiative loss is more tedious but does not make a large contribution. Assuming an optically thin corona, the volume emission rate over all frequencies  $P_{\text{rad}}(n, T, Z)$  can be evaluated at  $(n_a, T_2, Z_2)$  and then scaled downward by  $[n(r)/n_a]^2$  as one integrates over the isothermal corona region. This yields

$$P_{2,r} = \int_a^\infty dr_1 2\pi r_1 P_{\text{rad}}(n_a, T_2, Z_2) \left[ \frac{n(r_1)}{n_a} \right]^2$$

Using Eq. (42), this can be written as

$$P_{2,r} = P_{\text{rad}}(n_a, T_2, Z_2) \cdot F(a, \delta, \eta), \quad (44)$$

where

$$F(a, \delta, \eta) \equiv 2\pi a^2 \frac{[1 + \delta]^\eta}{\eta} \int_1^\infty dx \frac{x^{1-2/\eta}}{[\delta + x]^\eta} \quad (45)$$

or

$$F(a, \delta, \eta) = \frac{2\pi a^2}{3} \left( \frac{1 + \delta}{\eta} \right) \times \left[ 1 + \frac{1 - 2/\eta}{2 + 2/\eta} (1 + \delta)^{1-2/\eta} {}_2F_1 \left( \begin{matrix} 2 + 2/\eta \\ 3 + 2/\eta \end{matrix} \middle| \frac{\delta}{1 + \delta} \right) \right] \quad (46)$$

using the hypergeometric function  ${}_2F_1(a_c b|Z)$ . The present version of the code calculates the values of  $N_2$ ,  $Q_{12}$ ,  $P_{2,r}$  at each time step using Eqs. (27), (28), (30), (37), and (40 - 46), and forms the explicit derivatives  $\frac{d}{dt}(Z_2 T_2)$  using Eq. (38). The corona radiation loss  $P_{2,r}$  is small compared with that of the core. It is only large enough to make a 1-5% change in the energy bookkeeping at earlier phases of the implosion. But despite its forbidding appearance, it is reasonably economical in the code.

The first analytic impact of the explicit treatment in evolving  $T_2$  is a modification of the previous circuit relation to include the direct effects of corona heating and magnetic energy. In this simple model (Ref. 3) the circuit consisted of an effective generator impedance,  $Z_g$ , in series with an inductive and resistive load,  $L_D \dot{I} + V_{p\ell} (I, R_{p\ell}, L_{p\ell})$ . Here  $L_D$  represents the diode inductance and  $V_{p\ell}$  the plasma voltage must be calculated using the core/corona plasma model configuration. If one imposes a driving generator voltage  $V_g(t)$ , (such as the fit to machine parameters due to J. Katzenstein (Ref. 13)), then the total current  $I(t)$  and all other plasma variables must satisfy

$$V_g(t) = I(t)Z_g + L_D \dot{I}(t) + R^* I + \frac{2\ell}{c^2} \frac{d}{dt} \left[ \int_a^{r_w} dr_1 \frac{I(r_1)}{r_1} \right] \quad (47)$$

Here Faraday's law is used to equate the line integral of  $E_z$  and the change in magnetic flux through a rectangle  $r: (a \leq r < r_w), Z: (-\ell/2 \leq Z \leq +\ell/2)$ ,  $\ell$  being the discharge length. If the inner radius is chosen at  $r = a$ , then the resistive contribution ( $j_a \eta_c \ell$ ) can be arranged into an effective resistance  $R^* = \frac{B \ell \eta_c}{(a^2 - r_i^2)} - \frac{2 \beta \ell \dot{a}}{c^2 a}$  with  $\eta_c$  the usual transverse Spitzer resistivity of the classical core plasma, suitably time dependent. This is so because the

current density  $j(r)$  is taken roughly independent of  $r$  within the skin depth of the core plasma,  $r_i \leq r \leq a$ . Within the corona, the current density is not proportional to  $E_z$ , and the overall plasma 'resistance'  $V_{p\ell}/I(r)$  must include a contribution from the anomalous resistivity in the corona. Since this resistivity must itself depend on  $E_z$  (and so on  $V_{p\ell}$ ) a linear relation  $V_{p\ell} \sim IR$  is impossible. In short, the corona, while resistive, has been assumed to be marginally stable with  $V_{d,e} = c_{s,2}$ . Such a "drift speed limiter" behaves as a constant current source rather than as a resistor in the usual sense.

In order to use Eq. (47), one must now explicitly calculate the inductive contribution using  $I(r_1: r_1 > a)$  and collect all terms according to their coefficients,  $\dot{I}$ ,  $I$ , etc. If the corona solution for  $I(r_1)$  is substituted directly, one obtains

$$\int_a^{r_w} dr_1 \frac{I(r_1)}{r_1} = 2n \left(\frac{r_w}{a}\right) I - \frac{c\alpha}{2} \ln(1 + \delta), \quad (48)$$

approximating  $r_w \gg r_c$ , the largest effective coronal radius. The circuit relation now becomes,

$$V_g(t) = I Z_g + L_D \dot{I} + R^* I + \frac{d}{dt} \left\{ I \frac{2\ell}{c} \ln\left(\frac{r_w}{a}\right) - \frac{\ell}{c} \alpha \ln(1 + \delta) \right\}. \quad (49)$$

Expressing all derivatives within the brackets in terms of changes in fundamental model parameters,  $\dot{\alpha}$ ,  $\dot{\delta}$ ,  $\dot{g}$ , and  $\dot{I}$ , one has

$$\begin{aligned}
V_g(t) = & Z_g \dot{I} + L_D \dot{I} + I \left\{ R^* - \left( \frac{2l\dot{a}}{c^2 a} \right) \right\} \\
& + \dot{I} \left\{ \frac{2l}{c^2} \left[ 2n \left( \frac{r_w}{a} \right) - \left( \frac{\beta + \frac{(1 + \beta g/2)}{1 + \beta_0 g/2\beta}}{1 - 2 + 4(\beta/\beta_0)} \right) \left( 1 + \eta^{-1} \frac{d\eta}{d\beta} (\beta - \beta_0/2) \right) \right] \right\} \\
& - \frac{l\dot{\alpha}}{c} \left\{ 2n(1+\delta) + \frac{\left( \frac{2\beta}{\beta_0} \right) - \left( \frac{2 + \beta g}{1 + \beta_0 g/2\beta} \right) \left( 1 + \eta^{-1} \frac{d\eta}{d\beta} (\beta - \beta_0/2) \right)}{1 - 2 + 4(\beta/\beta_0)} \right\} \\
& + \frac{l\dot{\alpha}\dot{g}}{c} \left\{ \frac{(1 - 2\beta/\beta_0) \eta^{-1} \frac{d\eta}{d\beta} - (1 + (\beta - \beta_0/2) \eta^{-1} \frac{d\eta}{d\beta}) / (1 + \beta_0 g/2\beta)}{1 - 2 + 4(\beta/\beta_0)} \right\}
\end{aligned} \tag{50}$$

with

$$\eta^{-1} \frac{d\eta}{d\beta} = 2 \left\{ \frac{\beta}{1 - \beta^2} + \frac{[g + (1 + 2g^2)\beta + 3\beta^2 g + \beta^3]}{[1 + 4g\beta + 2(1 + 2g^2)\beta^2 + 4g\beta^3 + \beta^4]} \right\} \text{ and} \tag{51}$$

$$\eta^{-1} \frac{d\eta}{dg} = 2 \left\{ \frac{\beta(1 + 2\beta g + \beta^2)}{[1 + 4g\beta + 2(1 + 2g^2)\beta^2 + 4g\beta^3 + \beta^4]} \right\} \tag{52}$$

This relation is implemented in the code, using the  $\dot{a}$  calculated with the value  $d(Z_2 T_2)/dt$  returned from the corona heat transport relation, Eq. (38), and other model variables available with each time step. The value of  $\dot{I}$  is computed at each time step and used to advance  $I(t)$  as  $V_g(t)$  drives the entire system. The inclusion of  $\dot{\alpha}$  and  $\dot{g}$  terms in the circuit relation had been unnecessary with the constraint  $(Z_2^* T_2) \equiv 0$  imposed. The proper treatment of them here points out the complex character of corona corrections to the plasma inductance ( $I$  coefficient) and the corona impact upon the connection between energy exchange and core/corona current partition ( $\dot{a}$  coefficient).

Presently the 0-D implosion code SPLAT incorporates Eqs. (50) and (38) to determine the evolution of  $I(t)$  and  $T_2(t)$ . In addition, several other modifications to the original core corona equations are included as minor optimizations, corrections, and explorations of possible anomalously dissipative processes.

In the coronal pressure balance, the electron pressure is supplemented by the ion pressure  $n_I T_I$  — with  $T_I$  taken the same in core and corona, and  $n_I(r) = Z(T_2)^{-1} n_e(r)$  through quasi-neutrality. The entire development of the coronal quasi-static state is unchanged, save only the replacement  $\alpha = (T_2 + Z_2^{-1} T_I) 2c / ec_s^2$ , cf. Eq. (39).

As in Eq. (36) in Section II, the core motion is specified by a particular velocity field

$$V_r(r,t) = G_1(r/r_i) + G_2(r_i/r) \quad (53a)$$

which also arises naturally as that solution of  $\nabla \cdot \underline{V} = + \frac{d}{dt} \ln \pi(a^2 - b^2)$  with no viscous stress. Here  $r_i$  is used as a convenient scale radius and

$$G_1 = \left( \frac{r_i a}{a^2 - b^2} \right) [\dot{a} - (b/a) \dot{b}] \quad (53b)$$

$$G_2 = \left( \frac{b}{r_i} \right) \left( \frac{a^2}{a^2 - b^2} \right) \cdot [b \dot{b} - (b/a) \dot{a}] \quad (53c)$$

as in Eq. (3) in Section II.

This velocity field is assumed to retain its characteristic spatial structure with  $G_1, G_2$  given by time dependent boundary conditions,  $\dot{a}, \dot{b}$ . The constraint  $\dot{b} = \dot{a} - \dot{c}_1$  allows one to develop an equation of motion for  $a(t)$  in particular:

(i) for  $b \neq 0$ :

$$a = B_1^{-1} \left\{ \frac{F}{c} - 2n \left( \frac{a}{b} \right) B_2 - B_3 \right\} \quad (54a)$$

$$F = -P_2 - \frac{2(BI)^2}{\pi c^2 (a - r_i)^2} \left[ \frac{a^2 - r_i^2}{2} - r_i^2 \ln \left( \frac{a}{r_i} \right) \right] + \frac{F_{rad}}{2\pi a}, \quad (54b)$$

$$B_1 = \frac{ab}{a+b} \ln \frac{a}{b} + \frac{1}{2}(a-b), \quad (54c)$$

$$B_2 = \dot{a}^2 - \frac{2\dot{a}c_1}{1-(b/a)^2} + \frac{c_1^2}{1-(b/a)^2} \left( \frac{a^2 + b^2}{a^2 - b^2} \right) - \frac{bc_1}{1-(b/a)^2}, \quad (54d)$$

$$B_3 = \dot{a}c_1 - c_1^2 / (1-(b/a)^2) + bc_1 / 2, \quad (54e)$$

and

(ii) once  $b = 0$ :

$$\ddot{a} = (\pi \rho a^2)^{-1} \left\{ 2 a(p_1 + F) \right\}, \quad (55a)$$

$$p_1 = n_1 \left[ T_1 + Z^{-1}(T_1)T_1 \right] \quad (55b)$$

with  $\rho$  the core mass density,  $n_1, T_1$  the spatially homogeneous core electron density and temperature,  $T_2$  the coronal electron temperature,  $c_1$  the core sound speed,  $\dot{c}_1$  its time derivative due to changes in  $(Z_1 T_1)$ , and

$$P_2 \equiv \frac{\alpha^2 \eta^2}{8\pi a^2} / \left[ r^{\frac{1}{2}} + \delta^{-\frac{1}{2}} \right], \quad (56)$$

the inward coronal pressure in terms of the parameters describing the (implicitly evolved) force balance. The spatially integrated heat balance equation completes the set of coupled differential equations required to evolve the core fluid explicitly. For the electron fluid, one has

$$\frac{d}{dt} (Z_1 T_1) = \frac{2A_m}{3M} \left\{ -2\pi P_1 ((a-b) \dot{a} + b c_1) + \frac{(BI)^2 \eta_c}{\pi(a^2 - r_i^2)} \right. \\ \left. + \pi (a^2 - b^2) \frac{3m_e n_1}{A_m \tau_e} (T_I - T_1) + Q_{12} - P_{rad} + Q_{vis} \right\} \quad (57a)$$

with

$$Q_{12} = 2\pi a (\vec{q}_{12} \cdot \vec{r}) \quad (57b)$$

the net core/corona electron heat exchange, and

$$P_{rad} = -(a^2 - b^2) [P_{Br} + P_{rec} + P_{line}] \quad (57c)$$

the radiative loss term, based on approximations due to Colombant and Tonon (Ref. 15), Davis and Jacobs (Ref. 4), and a simple line radiation opacity model due to Apruzese (Ref. 7). The viscous heating term is given by

$$Q_{vis} = \frac{4\pi}{3} \eta_o^e \left\{ \frac{[\dot{a} - (b/a) \dot{b}]^2 + 3 [\dot{b} - (b/a) \dot{a}]^2}{(1 - b^2/a^2)} \right\} \quad (57d)$$

$$\text{with } \eta_o^e = 0.73 \eta_I T_I \tau_{ee} \quad (57e)$$

resulting from a straightforward evaluation of the classical expression, cf. Braginskii (Ref. 12). A similar expression obtains for the ion fluid,

$$\frac{d}{dt} T_I = \frac{2Am_p}{3M} \left\{ - 2\pi Z^{-1} n_I T_I ((a-b) \dot{a} + b c_1) + \pi (a^2 - b^2) \frac{3m_e n_I}{Am_p \tau_e} (T_I - T_e) + Q_{vis} \right\} \quad (58)$$

with  $Q_{vis}$  evaluated for appropriate ion coefficients. In these expressions  $\tau_{ee}$  is the usual Braginskii collisional relaxation time,  $M$  is the total mass per unit length in the core plasma;  $m_e$  and  $m_p$ , the electron and proton masses;  $A$  and  $Z_{1,2}$  the atomic number and (temperature dependent) charge state;  $\eta_c$ , the classical transverse resistivity.

The viscous heating term for the ion fluid may be enhanced during periods of compression at hypersonic speeds ( $\dot{a}/c, < -1.5$ ) to reflect the ion-electron energy relaxation time  $\tau_{I,e}$  rather than the classical like-species relaxation time. The physical picture here derives from the fact that ion-ion relaxation in these situations exhibits Coulomb logarithms of order one, indicating a rather fundamental inadequacy of classical transport theory. As such ions tend to behave more like a strongly coupled fluid than a classical plasma, momentum transferred from more tenuous, faster flowing regions into more dense, slowly flowing regions will tend to be distributed among several ions at a time in many-body collisions. These ions can then be considered as a quasi-neutral clump, transporting the momentum over a path length dictated by the time required for electrons to dissipate their ordered motion. Hence an ion-electron collisional relaxation time is more appropriate for the calculation of the viscosity.

While a detailed calculation of such effects is clearly preferable, a simple ad-hoc application of the basic idea here can be quite useful in directing future investigations. At present, when desired, the viscosity coefficient is smoothly allowed to rise to  $\eta^* = 10(\tau_{ie}/\tau_{ii})\eta_{cl}$  as  $\dot{a}/c$ ,

becomes less than - 1.5, indicating an "average" clump of about 10 ions. The effect is to heat the ion fluid heavily, with this thermal energy more slowly coupled to the electron fluid and future radiative losses. However, if the plasma thermal relaxation time  $\tau_e$  becomes so short that separate ion and electron temperatures equilibrate rapidly, this unbalanced heating of the ion component tends to cause rapid oscillatory heat exchange between the electrons and ions. When such effects attempt to dominate the numerical integration, the simplest and most appropriate course of action is to leave this heating source out pending a detailed calculation.

The calculation of  $\frac{d}{dt} (Z_1(T_1) T_1)$  and  $\frac{d}{dt} (Z_2(T_2) T_2)$  is transformed to a direct expression for  $T_1$  or  $T_2$  using any explicit functional model for  $Z(T_e)$  appropriate to the plasma species being investigated. As the power warms the plasma during compression, the resistive magnetic diffusion of  $r_i$  is smoothly replaced by a simple transport of  $r_i$  using the velocity field  $V(R)$  above. The simple scaling of the magnetic diffusion process (Ref. 1) used originally is now active only in the early stages of the implosion.

#### D. Self-consistency of the Model Assumptions

Of the three surviving assumptions among those considered at the outset, the one most deserving of some scrutiny is that of the quasi-static corona. From the explicit solution for  $n_2(r)$ , one can derive a simple criterion for the spatial extent of the coronal region,

$$r_c \sim a(10 + 9\delta)^{1/n}$$

being the radius for which the coronal density has decayed to about

$$\frac{(10 + 9\delta)^{1/n}}{100} n_a. \text{ Typically one finds } n \sim 5 \text{ to } 7, \delta \sim .4 \text{ to } .6 \text{ at peak}$$

compression (maximum coronal temperature and spatial extent) so that this

density is about  $0.06 n_a$  or less. If one computes how many times a sound wave can transverse the distance  $(r_c - a)$  in the time required for the implosion dynamics to change  $a$  by 10%, the result is usually of order 10 - 100 and of order unity only for the largest  $\dot{a}$  values on the implosion trajectory. There is good reason to believe that these largest  $\dot{a}$  values are somewhat unphysical anyway, so the quasi-static corona assumption appears quite consistent with the other elements of the model dynamics. The physical picture implied is that the corona can both expand to track the imploding core surface and also rearrange its internal state on a shorter time scale through the propagation of sonic turbulence, in order to continuously "hover" about the marginal stability condition and isothermal pressure balance.

The assumption that higher energy coronal electrons can be stopped in a short distance of core plasma also remains valid throughout the implosion process insofar as higher core densities occur simultaneously with the high coronal temperatures and produce a very short classical mean free path for the electrons. This constraint is even more easily satisfied in the later versions of the model because the coronal temperatures are somewhat lower than those previously calculated. This is due primarily to the improvements in the coronal kinetic energy transport calculation discussed above.

Finally, one must examine the consequences of invoking a precipitous density variation on the core/corona interface and here the results are not as good. The predominant effect of this discontinuity in  $n_e$  is to enhance the outward kinetic energy flux of core electrons very rapidly near the peak implosion and it can produce (through heating) a corona so great in spatial extent that it requires all the available current to maintain its pressure balance. In any physical system such a density gradient must remain finite and a smooth connection of core and corona density will result. This is one

of two primary motivations for expanding the model to take account of the spatial density variation in the core, the second being the extreme sensitivity of the model dynamics to the accuracy of the radiative loss calculation. A properly physical radiative transport and loss calculation cannot be obtained if the density variations are excluded. The required modifications to the model are discussed in Section IV below.

#### E. Explicitly Time-Dependent Code Results and Evaluation

The numerical parameters and behavior typical of this zero-D model as implemented are described in a short confidential supplement to this report. The case treated is meant to correspond, however roughly, to wire plasma imploded with diode and driver parameters corresponding to the Maxwell Laboratory devices. The driving voltage is that  $V_g(t)$  due to Katzenstein (Ref.13) offset by a short delay time to allow for the annular plasma formation and multiplied by arbitrary input factors (nominally unity) to allow varying the peak voltage and rise time. This calculation used  $V_g(t) = V_{Katz}(t + 31_{nsec})$ . The evolution of  $\{a(t), b(t), P_{rad}, T_1(t), V_g(t), I(t), n_1(t), I_1(t)\}$ , i.e., the inner and outer radii, core and corona electron temperature, total current and driving voltage, core electron density and core current, respectively, is shown in Figure (2a, b). Here  $a(t), b(t)$  are in cm, and  $T_1$  is in kev  $P_{rad}, n_1, I, V_g$  are in arbitrary units.

The example shown here is nearly one of a class of system trajectories one might call the "exploded corona". As the implosion proceeds the core current fraction  $\beta$  begins to drop rapidly upon assembly of the annulus. With the current then shifted into the corona and the reversal of  $Q_{12}$  to produce corona heating rather than core heating, the corona temperature rapidly increased. This in turn can further shift  $\beta$  toward zero and the 0-D model often becomes unstable.

Fig. 2a. Annulus Evolution and Radiated Power in the Explicit-T<sub>2</sub> Model

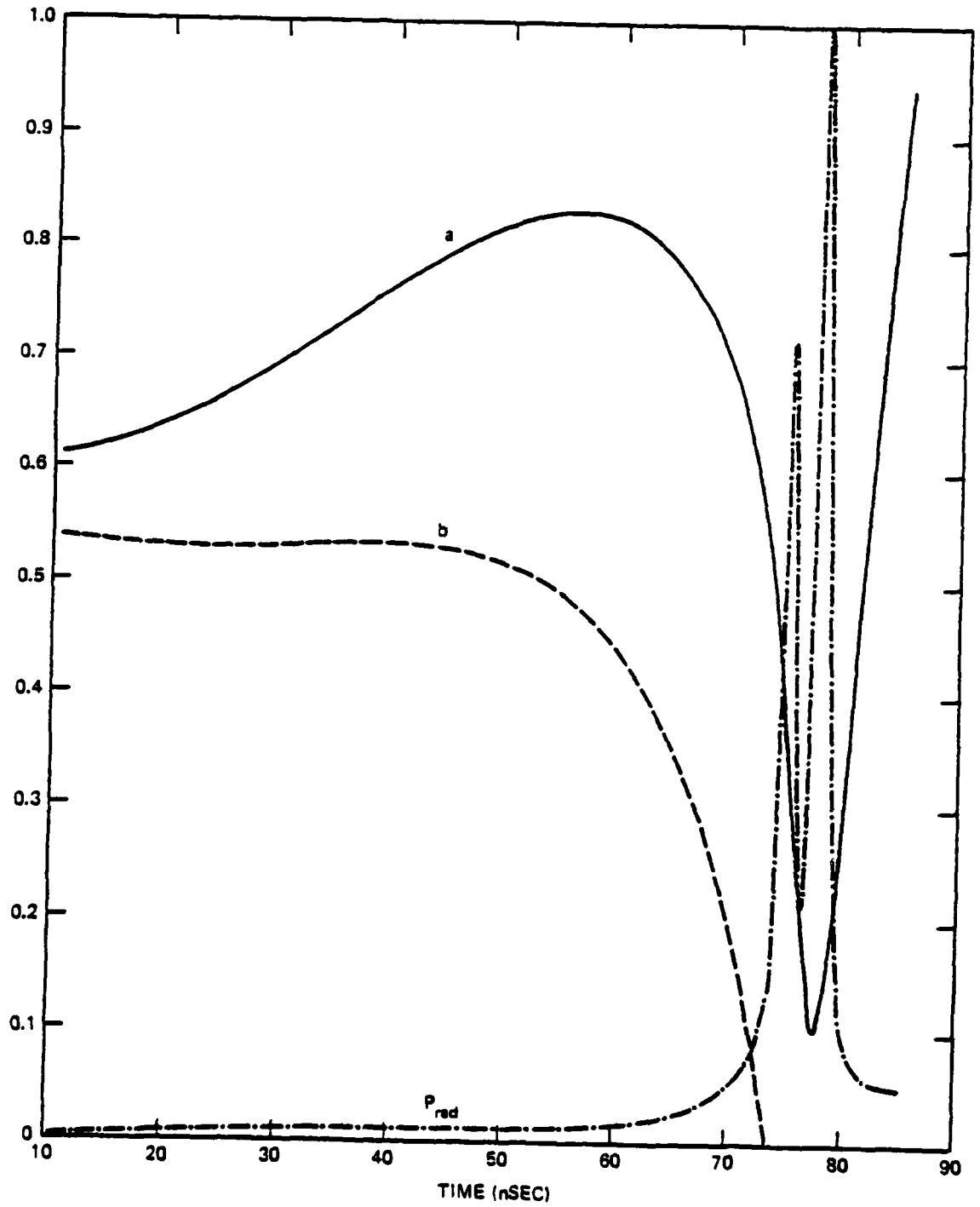
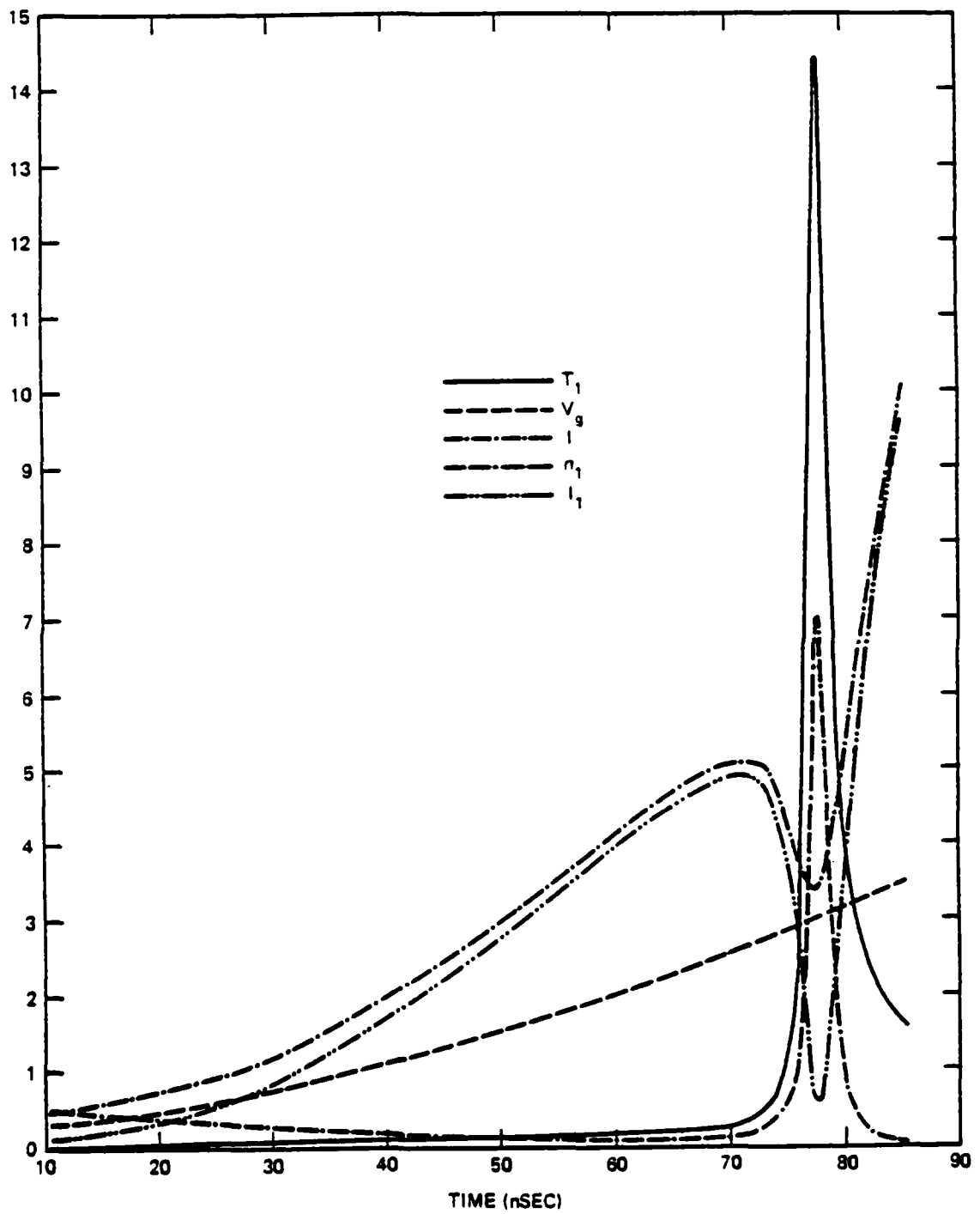


Fig. 2b. Thermodynamic Variables and Circuit Response



If there is sufficient energy to be removed from the core, this tendency to drop  $\beta$  will proceed until the corona is forced to be essentially infinite in extent. An extremely expanded corona is not particularly plausible because of the constraint that a sonic disturbance should traverse the corona as implied by the model trajectory in times short compared to the required hydrodynamic time step. In an ideal case, one would find the fraction  $\beta$  to be well above 0.05 over the entire implosion process.

The second general class of systems trajectories is quite the opposite case, which one might call the "refrigerator". In this second scenario, the fraction  $\beta$  is driven toward one as assembly occurs. This enhances the forces compressing the core plasma and simultaneously drives the coronal temperature downward. The plasma is driven to even smaller radii and higher densities where it radiates copiously and begins to cool. In this final phase,  $T_1$ ,  $T_I$  and  $T_2$  are driven toward zero, dropping by an order of magnitude or more in a few nanoseconds.

In both cases described above the current trace is quite similar, the decay of  $I(t)$  after assembly in Figure 2b is due to the time-dependent nature of the plasma inductance. If the implosion speed is very large one finds that the term,  $-\frac{2\dot{a}}{c^2 a}$ , in Eq. (50) can easily be dominant over  $R^*$  and  $Z_g$ . Any experimental current trace not exhibiting this downward trend would be interpreted, in terms of this model, as one corresponding to a slow implosion velocity. In any case, the behavior of the circuit variables is not particularly enlightening as to the reason for the "refrigerator" and "exploded corona" bifurcation among the system trajectories.

The strength of the core radiation loss and the coronal heating are the primary variables controlling the transition from "refrigerator" to "exploded corona". For any model conditions, a change of the order of 1% in radiation volume emission rate  $P_{\text{rad}}(n,T,Z)$  can force the system from one case to another. For larger emission rates the "refrigerator" model occurs, and, as the emission rate is smoothly lowered (for all time steps), there will exist a critical value for this quantity such that the "exploded corona" mode is established for all lower values of  $P_{\text{rad}}(n,T,Z)$ . Such manipulation of  $P_{\text{rad}}$  has no direct physical significance, of course. On the other hand, it is of primary consequence in the model evolution at the onset of the radiation pulse. The nature and time history of this pulse and its dependence on some of the system or code parameters is discussed briefly in the confidential supplement.

An additional factor which figures heavily in producing a near "exploded corona" trajectory is the initial radius of the annulus. In an obvious way, arrays of larger radii will require the thermalization of more kinetic energy at assembly and thus heat both core (and corona) to a greater degree. This in turn tends to drive  $\beta$  downward and there will exist, for a specified driving voltage waveform and radiative loss, a sufficiently large initial radius such that the corona will always "explode" near the time of initial assembly. These effects are indicative of several things.

First, the larger implosion speeds and flow kinetic energies are derived primarily from an intrinsic bias in any spatially uniform fluid description toward the most rapid possible response to the impressed  $\underline{j} \times \underline{B}$  forces in the surface layer. The fact that these larger speeds are limited as well as they are by the coronal current channel is a measure of its rather wide dynamic range in pinch-softening capabilities; but these capabilities are clearly

bounded by the upper limit to  $\beta_0$  forced by the logical structure of this sort of corona.

Second, the radiation pulse length is tightly linked to the overall time scale of compression and expansion in the core fluid. While better radiation loss calculations can significantly change this pulse length, the core density and temperature trajectory is the primary function to concentrate upon. It is the actual input to any radiative loss calculation and is, therefore, the ultimate determinant of the radiation pulse length. Any process that bears on the density and temperature trajectory calculation has a significant impact upon the loss calculation and attendant radiation pulse length, but not conversely. For example, the details of the total current evolution,  $I(t)$ , will not be particularly sensitive to the loss calculation (even though  $\beta(t)$  is quite sensitive). On the other hand, this total current is quite central to the density and temperature trajectory calculation. The code replicates this conclusion (cf. Figure 2b) with the weakened notch of  $I(t)$  (relative to that in  $I_1(t)$ ) through the complex radiation pulse generated by  $n_1(t)$ ,  $T_1(t)$  during the implosion.

This is not to say that almost any radiative loss calculation will suffice, for clearly it will not. One must take into account the effects dependent on density and temperature profiles and take care to evolve the plasma and the radiation self-consistently. The density and temperature trajectory calculation never decouples from the radiative loss calculation on any time domain of interest through the implosion.

Because of this tight linkage between the radiative pulse length and density/temperature trajectories, the modifications discussed in the next Section IV were undertaken as a prelude to more advanced calculations of

radiative losses. The improvements derived from this more physical and detailed picture help to bring the model in closer agreement with experiment by lowering the overall implosion speeds and by making possible more accurate radiative loss calculations, although even further changes will be seen to be required in order to confidently duplicate experimentally observed results.

A third primary facet of the model dynamics is the oscillatory behavior after the initial compression. This is aggravated by the fact that there is no dissipative mechanism, within the present model, which can sap the inward momentum of the collapsing plasma directly.

The plasma now behaves as a radiatively damped, and quite non-linear oscillator — using the pressures built up through thermalized flow kinetic energy, ohmic heating, and core/corona heat exchange to reverse its radial motion.

In fact, the core heating is the only retarding influence on the compression of the pinch, and this is why larger radiative losses can bring on a refrigerative collapse. In a simple mechanical analogy, the radiative loss rate eats away at the maximum available potential barrier (the pressure built up at the end of implosion) so that a given plasma with specified kinetic energy input can find either a positive or negative total energy upon reaching the axis, depending on the radiative loss rate. The oscillation is heavily damped and is not readily apparent experimentally, but neither is the refrigerative collapse. The simplest alternative is some motion within the corona (vorticity is a good candidate) that can act as a momentum reservoir, fed during compression and dissipated afterward. This possibility is being investigated, but it can be examined dynamically only once the improvements of Section IV are implemented successfully.

#### IV. SELF-SIMILAR 1D CORE-CORONA CALCULATION

##### A. Mathematical Model for Self-Similar Core Compression

###### 1. Basic Requirements

The velocity field currently used, Eq. 53(a), is a special case of the following simple theorem for compressible fluid mechanics.

Thm 1. Given a set of nested surfaces  $\psi(\underline{x},t) = \psi_i$  parametrized by spatially constant numbers  $\psi_i$ , let the quantity  $s_n \equiv -\frac{D}{Dt} \ln v_{ij}$  denote the logarithmic convective derivative of the volume enclosed by any two such surfaces, and the values  $\dot{\psi}_i \hat{n}_i, \dot{\psi}_j \hat{n}_j$  the normal velocities of such surfaces as they move with a fluid. If the flow field  $\underline{V}(\underline{x},t)$  appearing in  $\frac{D}{Dt}$  is now decomposed as

$$\underline{V}(\underline{x},t) = \underline{I}(\underline{x},t) + \underline{\Omega}(\underline{x},t)$$

with  $\underline{\nabla} \times \underline{I} \equiv 0$ ,  $\underline{\nabla} \cdot \underline{\Omega} \equiv 0$ ; and  $\underline{\Omega}$  is given as any solution of  $\underline{\nabla} \times \underline{\Omega} = \underline{\nabla} \omega$  (admitting only rigid rotor vorticity), then (i) the field  $\underline{V}(\underline{x},t)$  is determined uniquely by the solution of

$$\underline{\nabla} \cdot \underline{I} = -s_n, \text{ interior to } v_{ij},$$

and (ii) all such fields  $\underline{V}$  exhibit no viscous stress, viz.  $\underline{\nabla} \cdot \underline{W} \equiv 0$ , whenever  $s_n = s_n(t)$ . The proof follows from a simple application of Helmholtz's theorem and the recognition of an equivalent Poisson problem for  $\underline{I}$  with Neuman boundary conditions on a closed, simply connected surface. A second result is immediate from the continuity relation:

Thm 2. Given the flow field  $\underline{V}(\underline{x},t)$  above, the number density exhibits a self-similar evolution of the following form:

$$n(\underline{x}, t) = e^{S(t, t_0)} n(\underline{x}_0(\underline{x}, t), t_0), \quad (59)$$

whenever  $s_n$  is spatially homogeneous,  $s_n = s_n(t)$ . Here one has

$$S(t, t_0) = - \int_{t_0}^t dt_1 \frac{D}{Dt_1} \ln v_{ij}(t_1) = \ln (v_{ij}^0 v_{ij}^t), \quad (59a)$$

and

$$\underline{x}_0(\underline{x}, t) = \underline{x} + \int_t^{t_0} dt_1 \underline{V}(\underline{x}(t_1), t_1) \quad ; \text{ which are} \quad (59b)$$

equivalent to the differential equation

$$\frac{D}{Dt} n(\underline{x}, t) = s_n(t) n(\underline{x}, t).$$

Of course, it is the equation of momentum transfer which determines the time evolution of the flow field and maintaining the specialized form of  $\underline{V}(\underline{x}, t)$  demands a specialized form for  $\frac{D}{Dt} \underline{V}$ . Seeking the most general transformation preserving the property that  $\underline{\nabla} \cdot \underline{V} = -s_n(t)$ , one finds,

$$\frac{D}{Dt} \underline{V}(\underline{x}, t) = \alpha_1(t) \underline{V}(\underline{x}, t) + \underline{\alpha}_0(t) \quad (60a)$$

or (60b)

$$\underline{V} = S_1(t, t_0) \left( \underline{V}(\underline{x}_0(\underline{x}, t), t_0) + \underline{S}_{0,1}(t, t_0) \right)$$

with (60c)

$$S_1(t, t_0) = \exp \int_{t_0}^t dt_1 \alpha_1(t_1),$$

and (60d)

$$\underline{S}_{0,1}(t, t_0) = \int_{t_0}^t dt_1 \underline{\alpha}_0(t_1) e^{-\int_{t_0}^{t_1} dt_2 \alpha_1(t_2)}.$$

These relations are equivalent to the condition  $\frac{D}{Dt}(\nabla \cdot \underline{V}) = \alpha_1(t)$ , which says that the time development of the local compression  $\nabla \cdot \underline{V}$  is independent of position.

These results can be related for an isothermal plasma by requiring the preferred form of  $\frac{D}{Dt} \underline{V}$  to be produced from the local combination of pressure gradient and  $\underline{J} \times \underline{B}$  stresses actually existing in the plasma. Neglecting the viscous stress because  $\nabla(\nabla \cdot \underline{V}) = 0$ , consider the profile solving

$$\left. \frac{\nabla n}{n} \right|_{t_0} = \frac{\tilde{m}}{\tilde{T}} \left\{ \frac{\underline{J} \times \underline{B}}{\tilde{m} c n} - (\alpha_1^0 \underline{V} + \alpha_0^0) \right\} \quad (61)$$

with  $\tilde{m} = m_e + Z^{-1} m_I$ ,  $\tilde{T} = T_e + Z^{-1} T_I$ , and  $\underline{V}$  given as any solution of  $\nabla \cdot \underline{V} = -S_n(t_0)$  ( $\nabla \times \underline{V} \stackrel{d}{=} 0$ ) for the geometry of interest. This profile now generates the preferred form of  $\frac{D}{Dt} \underline{V}$  required in Eq. (60a), and, so long as this structure for  $\frac{D}{Dt} \underline{V}$  is maintained, the profile can be evolved using Eq. (59) -  $\nabla \cdot \underline{V}$  remains spatially homogeneous.

If external forces are involved, it is not clear that any such preservation of  $\frac{D}{Dt} \underline{V}$  is possible. Let  $\underline{A}_J \equiv \frac{\underline{J} \times \underline{B}}{\tilde{m} c n}$  and restrict attention to those forces satisfying a relation of the form  $\frac{D}{Dt} \underline{A}_J = S_A(t) \underline{A}_J$ . Then, as discussed below, it is possible to maintain a homogeneous  $\nabla \cdot \underline{V}$  at the expense of some restriction on the time dependence of  $\underline{A}_J$ . Expressing  $\underline{A}_J$  in terms of its initial value, with  $S_A(t, t_0) \equiv \int_{t_0}^t dt_1 S_A(t_1)$ ,

$$\underline{A}_J = S_A(t, t_0) \underline{A}_J^0(\underline{x}_0, t_0) ;$$

and the constraint on  $\frac{D}{Dt} \underline{V}$  becomes

$$\alpha_1 \underline{v} + \alpha_0 = \frac{D}{Dt} \underline{v} \equiv - \frac{\tilde{\tau}}{m} \left( \frac{\nabla n}{n} \right)_t + S_A(t, t_0) \underline{A}_j^0$$

as  $\frac{\nabla n}{n}$  and  $\underline{A}_j$  evolve in time. Can any such  $\underline{A}_j$  exist?

A special case for the profile  $\underline{j}(\underline{x}, t)$  of interest here is any form  $\underline{j}(\underline{x}, t)$  which is itself locked to the fluid flow, i.e.,  $\underline{j}(\underline{x}, t)$  such that

$$\frac{D}{Dt} \underline{j}(\underline{x}, t) = S_j(t) \underline{j}(\underline{x}, t) \quad (62)$$

from which it follows through the "generalized Ohm's Law" (Ref. 14) that

$$\eta_c [1 + \nu^{-1} S_j] \underline{j} = \underline{E} + (\underline{v} \times \underline{B}) c^{-1}. \quad (63)$$

Further, for an isothermal, highly collisional plasma ( $S_j(t) \nu^{-1} \ll 1$ ) with a nearly homogeneous resistivity  $\eta^* \equiv \eta_c (1 + \nu^{-1} S_j(t))$ , one has

$$\begin{aligned} \underline{\nabla} \times \eta^* \underline{j} &\sim \eta^* (\underline{\nabla} \times \underline{j}) \equiv \underline{\nabla} \times \underline{E} + c^{-1} \underline{\nabla} \times \underline{v} \times \underline{B} \\ \underline{\nabla} \times \underline{j} &\equiv - \frac{c}{4\pi} \square^2 \underline{B}, \text{ and } \underline{\nabla} \times \underline{E} = - c^{-1} \partial_t \underline{B}, \text{ thus} \\ - \frac{c \eta^*}{4\pi} \square^2 \underline{B} &= - c^{-1} (\partial_t \underline{B} + \underline{\nabla} \times \underline{v} \times \underline{B}); \end{aligned} \quad (64)$$

and using the continuity relation for  $n$  through  $\underline{\nabla} \cdot \underline{v} = - \frac{D}{Dt} \ln n(\underline{x}, t)$ , this yields

$$\frac{c^2 \eta^*}{4\pi} \square^2 \underline{B} = n \frac{D}{Dt} \left( \frac{\underline{B}}{n} \right) \quad (65)$$

as the implied constraint on  $\underline{B}/n$  for self-similar  $\underline{j}(\underline{x}, t)$  evolution. In the limit of large conductivity this relation forces  $\underline{B}$  and  $n$  to scale identically with the local compression of electron density, thus  $\frac{D}{Dt}$  results in

$$\frac{D}{Dt} (\underline{j} \times \underline{B}/n) \sim S_j (\underline{j} \times \underline{B}/n). \quad (66)$$

With the results of Eq. (66), and the fact that

$$\frac{D}{Dt} \left( \frac{\nabla n}{n} \right) = - \left( \frac{\nabla n}{n} \cdot \underline{\nabla} \right) \underline{v} - \underline{\nabla}(\underline{\nabla} \cdot \underline{v}) \quad , \quad (67)$$

one can derive (for a slab geometry) a simple constraint on the time development of  $\underline{A}_j$ . If a plasma slab is allowed to expand away from its density maximum on a plane  $x^*$ , and exhibits an initial density profile solving Eq. (61) consistent with a linear spatial dependence of the velocity field  $\underline{v} = G_1(t)(x - x^*)$ , then self-similarity can be maintained exactly whenever

$$S_A(t, t_0) = \frac{(\tilde{T}Z)}{(\tilde{T}_0 Z_0)} \frac{\tilde{m}_0 Z}{(\tilde{m}Z)} \exp - \int_{t_0}^t dt_1 G_1(t_1) \quad . \quad (68)$$

Here the point  $x^*$  is an invariant or fixed point of the mapping  $x^0 \rightarrow x(t)$  generated by  $\underline{v}(\underline{x}, t)$ . This relation implies a particular decay rate for the current density in the plasma. The scaling parameter  $S_A = S_j(t_1)$  must be such that it compensates for the temperature decay while the ratio  $\underline{B}/n$  remains constant on any expanding density contour  $(\underline{x} - \underline{x}^*)(t)$ . The partial time derivative of Eq. (68) provides the requirement

$$S_j \cong \frac{Z\tilde{T}}{\tilde{T}Z} - G_1 \quad ;$$

and this admits a simple physical interpretation. The isothermal nature of this expansion is preserved only because the  $pdV$  work done to move the plasma is spatially homogeneous, i.e.,  $\frac{1}{ZT_e} \frac{D}{Dt} ZT_e \cong -\nabla \cdot \underline{v}$ ,  $\frac{1}{T_I} \frac{D}{Dt} T_I \cong -\nabla \cdot \underline{v}$ . This implies the constraint  $S_j = -2(\underline{\nabla} \cdot \underline{v}) + G_1 = -(\underline{\nabla} \cdot \underline{v})$  and hence makes the imbedded  $\underline{A}_j$  compatible with the self-similar expansion. Now, if  $\underline{B}/n$  is constant on  $(\underline{x} - \underline{x}^*)(t)$  and  $S_j = -(\nabla \cdot \underline{v})$ , the time decay of  $\underline{A}_j$  is due solely to the density

decay in  $\underline{J} = n e \underline{V}_{D,Z}$  throughout the current carrying layer, for any current profile  $\underline{J}(\underline{x}, t)$ . The self-similarity is preserved because  $\underline{E}_Z = n^* e \underline{V}_{D,Z} n$  must change in step with  $n$  &  $T_e$  as the drift speed  $V_{D,Z}$  is held constant at its original local value, in order to preserve self-similarity. Clearly an arbitrary time dependence for  $\underline{E}_Z$  is not compatible with the self-similar expansion.

The self-similar motions generated by initial profiles solving Eq. (61) can be extended to curvilinear coordinate systems with more modifications. In cylindrical coordinates the only true self-similar expansions or contractions must be centered on the origin; however, a thin annulus can maintain such self-similarity approximately while its ratio of thickness to mean radius is small. In general the profiles generated by Eq. (61) are appropriate to physical systems which begin in a very viscous state before transition to plasma and any period of strong viscosity in the later evolution will always tend to drive the velocity field back to a profile such that  $\nabla \cdot \underline{V}$  is spatially homogeneous. This, in turn, tends to force the density profile back to its self-similar evolution.

When the core plasma is coupled to the marginally-stable pressure-balance corona, the regions of self-similar evolution are those for which  $J$  is approximately  $\underline{J}_0(\underline{x}_0, t_0) \cdot \underline{V}_{ab}^0 / \underline{V}_{ab}^t$  and the viscous heating is either spatially homogeneous or negligible. Moreover, the constraint  $S_j \sim -(\nabla \cdot \underline{V})$  cannot be maintained easily because the factor  $S_j$  must respond to the external equations that provide the boundary value of  $\underline{E}$  on the surface of the core.

But, since self-similar solutions provide quite economical computational models, it is quite useful to let Eq. (61) determine the initial profile  $n(\underline{x}, t)$  over the plasma, and approximate its evolution to remain self-similar

(in the sense of Eq. (59)), with continuity required of  $n$ ,  $V$ , and  $T$  at the core/corona interface defined by the constraint that

$$c_S = \frac{J(\underline{x}, t)}{en(\underline{x}, t)} \quad (69)$$

This provides the opportunity for a more physical calculation of the core/corona electron heat exchange that is so important in the energetics.

## 2. Application to Strictly Radial Geometry

Specializing Eq. (61) to radial variations only is relatively straightforward once a model profile for  $J_z(r, t)$  is chosen. The uniform current density being the preferred asymptotic final state of a magnetic diffusion process, we can set

$$\underline{E}' \equiv \underline{E}_z + c^{-1} \underline{v}_r \times \underline{B}_\theta = \begin{cases} E_a (1 - e^{-pY_R}) & Y_R > 0 \\ 0 & Y_R < 0 \end{cases} \quad (70)$$

with  $Y_R \equiv r/r_I - 1$ , and  $r_I$  defining the innermost penetration depth of the fields. Then, using the velocity field of the original model (a rotation-free special case of Thm 1) with  $\dot{a}$ ,  $\dot{b}$  denoting the normal velocities of the nested cylindrical surfaces, the solution of Eq. 61 can be expressed as

$$n_1(x_R) = n_0 F_{\frac{1}{2}}(\xi_a, -\mu_0, \sigma_0) \cdot \left\{ C_0 - H(x_R) {}_{\frac{1}{2}}F_1 \left[ U_{\frac{1}{2}+1}(\xi_a, \mu_0, \sigma_0) - U_{\frac{1}{2}-1}(\xi_a, \mu_0, \sigma_0) \right] \right\} \quad (71)$$

in the limit that  $p \rightarrow \infty$  in Eq. 70. Here for convenience we have let

$$F_{\frac{1}{2}}(x, \mu, \sigma) \equiv (1+x)^{-\frac{1}{2}} \exp \left[ \mu(\sigma x + x^2/2) \right] \quad (72)$$

and

$$U_{\zeta}(\xi, \mu, \sigma) \equiv \int_0^{\xi} F_{\zeta}(x, \mu, \sigma) dx \quad (73)$$

This solution arises from casting Eq. 61 in dimensionless form;  $n_0$  is a reference mean density, and applying the integrating factor

$$\exp - \frac{\tilde{m}}{\tilde{T}} r_I \int dR [x_{or} + \alpha_1 V_r(R)],$$

where

$$\tilde{m} = m_e + Z^{-1} m_I,$$

$$\tilde{T} = T_e + Z^{-1} T_I,$$

and

$$R = r/r_I, \text{ using } r_I \text{ as a convenient scale radius.}$$

In Eq. 71, the function  $H(x_R)$  is the unit step function, of argument

$$x_R \equiv \frac{r/r_I - 1}{a/r_I - 1}.$$

The various parameters of the model self-similar profile remaining in Eq. 71 are defined as

$$R_a \equiv \frac{a}{r_I}$$

$$\xi_a \equiv x_a(R_a - 1)$$

$$\mu_0 \equiv m r_I \alpha_1 G_1/T$$

(74)

$$\sigma_0 \equiv 1 + \alpha_0/\alpha_1 G_1$$

$$\zeta \equiv m r_I \alpha_1 G_2/T$$

$$\xi_1 \equiv (E'_a r_I/n^*c)^2/n_0 T$$

and  $G_1, G_2$  are given by Eq. 53(b,c,). The constant of integration  $C_0$  is determined by the radial equivalent of Eq. 69, i.e., one defines the core/corona interface by the electron drift speed in response to the local  $E'$  field. One finds the appropriate  $C_0$  to be

$$C_0 = \frac{n_a}{n_0} F_{\frac{1}{2}}(R_a - 1, \mu_0, \sigma_0) + \pi \xi_1 \left[ U_{\frac{1}{2}+1}(R_a - 1, \mu_0, \sigma_0) - U_{\frac{1}{2}-1}(R_a - 1, \mu_0, \sigma_0) \right] \quad (75)$$

with  $n_a \equiv E'_a / en^*(T_1) c_1(T_1)$ . A further requirement is that the density profile should normalize to envelop a specified total mass. In the case of Eq. 71 with  $C_0$  fixed by Eq. 75, the normalization condition arising from a total number,  $N_T$ , of atoms in the initial plasma becomes

$$Z(T_1) N_T = 2\pi r_I^2 (R_a - 1) \int_{x_b}^1 dx_R n_1(x_R) \left[ 1 + (R_a - 1)x_R \right], \quad (76)$$

with  $x_b = (b/r_I - 1)/(a/r_I - 1) < 0$ . This can be reduced to an equation for the parameter  $(R_a - 1)$  that is easily solved numerically, i.e.

$$R_a - 1 = \frac{Z_1 N_1}{2\pi r_I^2 \int_{x_b}^1 dx n_1(x) \left[ 1 - (R_a - 1)x \right]} \quad (77)$$

The denominator on the right is an increasing function of  $(R_a - 1)$  since as  $(a/r_I - 1)$  is increased, the absolute value of the profile  $n_1(x_R)$  is forced to intersect  $n_1 = n_a$  at a larger value of argument of the decaying exponential appearing in Eq. (71). One need only increase  $R_a - 1$  for fixed  $(b, r_I)$  (and other model parameters) until an intersection of  $f(a) = R_a - 1$  and  $g(a) = \text{RHS of Eq. (77)}$  is achieved.

The density profile can be evolved in an economical way only by following  $a, b, \dot{a}, \dot{b}, \ddot{a}, \ddot{b}$  in a Lagrangian sense in order to keep track of the time evolution of all the profile parameters  $\alpha_1, \alpha_0, G_1,$  and  $G_2$ . This is because the fundamental similarity variable is defined through an integral equation,

$$r_0(r,t) = r + \int_t^{t_0} dt' V_r(r(t'), t')$$

so that one must always follow the bounding zones of the self-similar solution region, and any interior zones of interest, e.g.  $r_1(t)$ , in a Lagrangian sense. The primary computational economy arises from the fact that all time derivatives required to follow the mesh are simple expressions, derived from the profile parameters that can be computed precisely rather than estimated from difference techniques.

The self-similar profile derived above will tend naturally to expand away from its density maximum and to fill the available space unless external forces change its motion. In the case of an annular profile responding to a specific model generator voltage trace, there are several factors which alter the self-similarity. These can be accommodated, however, by simple models for the run-in, assembly on axis, and later phases of the implosion. The primary modification is that due to changes in the magnitude and distribution of external force densities within the plasma. The original imbedded profile of  $\underline{J} \times \underline{B}$  force must respond to complex changes in the  $\underline{E}_z, \underline{B}_\theta$  surface fields and also reflect an ambipolar radial electric field and the associated  $\rho \underline{E}_r$  stress. The final stresses moving the plasma annulus inward will be a complicated superposition:  $-\nabla p + \rho \underline{E}_r + \underline{J}_z \times \underline{B}_\theta c^{-1}$ . As an overall drift inward is developed,

the compression will tend to be greater on the interior surface ( $\nabla \cdot \mathbf{v}$  receives a weak contribution  $\sim r^{-2}$ ) and as the plasma annulus closes down on the axis the density gradient will reverse (cf. Eq. (67)) and slow the inner surface more violently. This violent deceleration will then propagate outward and force a conversion of flow energy to thermal energy. This "collection" process onto the axis is the second source of alterations to self-similar motions in an expanding annulus.

In contrast to these mechanisms altering self-similarity, there is the action of viscosity, which tends to restore the homogeneity of  $\nabla \cdot \mathbf{v}$  when included in the momentum transport equation. In most applications of classical fluid plasma theory, viscosity is a relatively weak process and is often neglected. The basis for this approximation is a collision calculation that assumes very weakly correlated plasma particles, as measured by the so-called Coulomb logarithm,  $\Lambda$ . As a simple calculation will attest,  $\Lambda$  for ion/ion collisions in an Al plasma with  $T_I \sim 8 \text{ eV} - 200 \text{ eV}$ ,  $n_I \sim 10^{18} - 10^{20}$  is not large enough to insure the correctness of classical transport theory. Except for the higher temperature points along the typical implosion trajectory, this parameter is less than or on the order of 1. One should therefore treat a strongly coupled plasma, with transport coefficients that include the influence of many-body collisions. The proper transport coefficients are not available, and it is necessary to model the general effects of such strong coupling. The model adopted thus far is based on the heuristic assumption that the stronger collisional coupling does not change the character of the dissipative fluid processes (heat conduction, viscosity, friction) but simply makes them more dominant. The immediate implication is that time-asymptotic configurations for dissipative fluid evolution are achieved quasi-statically in the

strongly coupled core fluid. For internal energy changes, this implies maintenance of a nearly isothermal temperature profile; for velocity field changes, a nearly homogeneous  $\nabla \cdot \underline{v}$  profile as required for self-similarity; and, for the relative flow of ions and electrons, an equal radial drift velocity for each species.

One may treat the run-in phase by assuming that all stress developed at the outer surface  $a(t)$ ,  $c^{-1}(\underline{j}_z \times \underline{B}_\theta)_a$ , is transmitted inward to the location of the density maximum by a self-consistent combination  $(\rho E_r + (\underline{j}_z \times \underline{B}_\theta)c^{-1})$  of stresses. This drives the density maximum to accelerate slowly inward with some speed  $\dot{r}_m(t)$  and (interior and exterior to the plasma density maximum in the frame moving at  $\dot{r}_m$ ) the pressure gradients and viscous contributions act to spread the profile with a  $v_r(r,t)$  exhibiting a homogeneous divergence. This simple model for the evolving velocity field can be summarized as

$$\ddot{r}_m = J_a B_a / \tilde{m} c n_m \quad (78a)$$

$$\ddot{b} = - \frac{\tilde{\tau}}{\tilde{m}} \frac{\nabla n}{n} \quad (78b)$$

together with the constraint

$$\dot{a} = \dot{r}_m \left( \frac{r_m}{a} \right) \left( 1 + \frac{a^2 - r_m^2}{r_m^2 - b^2} \right) - \dot{b} \left( \frac{b}{a} \right) \left( \frac{a^2 - r_m^2}{r_m^2 - b^2} \right) \quad (78c)$$

arising from the  $\nabla \cdot \underline{v}$  homogeneity. Here  $n_m$ ,  $r_m$ ,  $\dot{r}_m$ ,  $\ddot{r}_m$  denote variables at the density maximum;  $n_b$ ,  $b$ ,  $\dot{b}$ ,  $\ddot{b}$ , those at the inner surface. Such a model has the advantages of computational simplicity and compatibility with the requirement

$\frac{D}{Dt} \underline{v} = \alpha_1 \underline{v} + \alpha_0$ . This enables one to advance a radial mesh of suitable

spatial resolution for the accurate computation of radiative losses.

The second phase is that of collecting the plasma onto the axis, and here one must be guided qualitatively by a very complex mix of phenomena. The instabilities available to the system because of strong density and flow gradients will tend to drive a significant level of microturbulence in the central regions, and the colliding ion fluid components will be strongly coupled collisionally as well. A detailed treatment of this sort of collapse is not within the scope of classical fluid plasma theory; but the net effect will be to mix the fluid, to dissolve the density and flow gradients, and to thermalize the energy previously tied up in the radial flow. At present a very simple model of this "collection" process has been implemented and it roughly describes the time development outlined above. As the inner surface ( $b(t)$ ) meets the axis, the number of particles flowing past a small collection radius,  $r_c$ ; is computed; and the flow energy of the local velocity field and density is thermalized. This continues at the first collection radius until enough material has flowed into the implied central cavity to erase the density gradient to  $r_c$ . At this point a new  $r'_c > r_c$  is chosen at the next grid location outside the previous radius; this models the propagation of the deceleration/turbulence front. The algorithm is continued until the densest region of fluid intercepts the collection radius and begins a compression of the (now uniformly filled) central region.

Once the particles are "collected", the third phase one must treat is the motion of the assembled plasma. This is modeled by again retaining a homogeneous  $\nabla \cdot \underline{V}$  and calculating the dynamics of the density maximum  $r_m$  in a manner similar to that used in the run-in phase. In particular, the  $\underline{J}_z \times B_\theta$  stress developed at the outer boundary is transmitted to the density maximum  $r_m$  and must compete with the local internal pressure in accelerating this

domain of fluid. The  $\nabla \cdot \mathbf{v}$  homogeneity then determines the accelerations and velocities of all other fluid elements, viz.

$$\ddot{\mathbf{r}}_m = \frac{2}{r_m} \frac{\tilde{T}}{\tilde{m}} - \frac{(\mathbf{j}_z \times \mathbf{B}_\theta)_a}{\tilde{m} c n_m} \quad (79a)$$

$$\ddot{\mathbf{a}} = \ddot{\mathbf{r}}_m \frac{a}{r_m} \quad (79b)$$

### 3. Modifications to the Core-Corona Energy Exchanges.

#### (i) Continuous Core/Corona Transition.

The smooth density falloff with radius in the outer regions of the self-similar core profile now allows us to define the Core-Corona Boundary as the point where instability to ion sound turbulence sets in. The transition from core temperature  $T_1$  to coronal temperature  $T_2$  must also occur on some scale length  $\lambda_T$  determined by the characteristics of those modes most heavily excited in the coronal turbulence. Since ion sound waves require a large temperature-gap  $T_2 > T_1$  in order to grow, the simplest self-consistent picture is one of linear temperature transition over a distance  $\lambda_T$  corresponding to a few growth lengths for the most unstable mode. In the case of the ion sound waves, this is a length on the order of several Debye lengths. A linear temperature connection and conservation of current density  $j_{z,a}$  provide a simple density transition  $n(a+\lambda_T) = \frac{c_1}{c_2} n_a$ . Outside the radius  $(\lambda_T + a)$ , the previous isothermal coronal quasi-equilibrium at  $T_2$  is appropriate. Once this density and temperature structure is adopted, it is possible to calculate the heat flux  $Q_{12}$  and particle interchange  $F_{12}$ , using the simple

Krook model discussed previously. The result is relatively simple,

$$Q_{12} = \pi a \left( \frac{\bar{n} \bar{T}^{3/2}}{2^{3/2} m_e} \right) \left\{ \frac{5V_t \tau_{ee} (-\partial_r \ln n_a)}{1 + (\Omega_a \tau_{ee})^2} - \frac{5V_t \tau_{ew} (\partial_r \ln n_a^+ + 4\partial_r \ln T_a^+)}{1 + (\Omega_a \tau_{ew})^2} \right\} \quad (80)$$

$$F_{12} = \pi a \left( \frac{\bar{n} \bar{T}^{1/2}}{2^{3/2} m_e} \right) \left\{ \frac{(-\partial_r \ln n_a) V_t \tau_{ee}}{1 + (\Omega_a \tau_{ee})^2} - \frac{V_t \tau_{ew} (\partial_r \ln n_a^+ + \partial_r \ln T_a^+)}{1 + (\Omega_a \tau_{ew})^2} \right\} \quad (81)$$

where the super-scripted "+" on  $T_a$  denotes gradients in the transition region,  $a < r < a + \lambda_T$ ,  $\bar{T}$  is  $\frac{1}{2}(T_1 + T_2)$ ,  $\bar{n}$  is  $\frac{1}{2}(n_1 + n_a^+)$ , and  $\tau_{ew}$  is a momentum exchange time for electrons with unstable waves. The calculation of  $F_{12}$  is an important addition to the coronal temperature derivative calculation, since

$$\frac{d}{dt} U_{c,e} = \frac{d}{dt} (N_c Z_2 T_2) \equiv I_2 E_z - P_{r,2} + Q_{12} \quad (82)$$

thus,

$$\frac{d}{dt} (Z_2 T_2) \equiv I_2 E_z - P_{r,2} + Q_{12} - \bar{Z}_2 \bar{T}_2 \cdot (F_{12}/Z_1), \quad (83)$$

with  $F_{12}$  the net electron exchange, weighting by  $1/Z_1$ , accompanying the diffusion of ions across the interface. These relations are currently implemented in SPLAT, and result in lower (more physical) coronal temperature.

(ii) Core Heating.

The spatially integrated forms of the electron and ion heat Equations 57 and 58 are still useful for an approximately self-similar core. Since ohmic heating is relatively insignificant, and since viscous heating and pdV works are spatially homogeneous or nearly so, and since (for a relatively opaque plasma) the radiative loss is primarily a surface term, one can simply adopt these previous heating expressions with only minor changes. This preserves the isothermal nature of the self-similar approximation to the fluid motion, yet it allows a more general calculation of radiation losses using the explicit density profile.

B. Improvements in Radiation Modeling.

At present, the radiative losses are calculated on the basis of several new analytic fits to recent sophisticated steady-state radiation computations. A frequency-integrated volume emission rate is computed for the average plasma ion density and electron temperature, to include bremsstrahlung, recombination, and line radiation from Al (K, L) shells. The line radiation emission per unit volume is fit with good precision to the results of Duston and Davis (Ref. 19) by using a series expression of the form:

$$\epsilon(n_I = 10^{19}, T_e) = \begin{cases} \exp \sum_k B_k^< [2n(T_e/0.300)]^k & \text{for } T_e \leq 300 \text{ ev} \\ \exp \sum_k B_k^> [2n(T_e/1.200)]^k & \text{for } T_e \geq 300 \text{ ev,} \end{cases} \quad (S4)$$

which is scaled by  $(\bar{n}_I/10^{19})^2$ , and subjected to an attenuation calculated on the basis of simple probability-of-escape ideas (Ref 7). In particular, the optical depth is estimated for a Doppler-broadened 0.5 keV line as

$$\tau \approx 2.1173E-17 (A/T_I)^{1/2} 2a(t)\bar{n}_I(t); \quad (85)$$

then probabilities of escape and quenching

$$P_E = \begin{cases} \frac{1}{1 + 1.86\tau + 0.817\tau^2} & \tau < 3 \\ \frac{0.286}{\tau (\lambda n(1.95\tau))^{1/2}} & \tau > 3 \end{cases} \quad P_Q = \frac{n_I(r)}{n_I(r) + 1.0E21} ,$$

are calculated. The power radiated in K and L lines is added to the bremsstrahlung (Br) and recombination loss (FB) rates, suitably attenuated by simple optical depth calculations, and a total effective emissivity

$$\epsilon_T(n_I(r), T_e, T_I, r) = \frac{\epsilon_{K,L}}{1 + P_Q(P_E^{-1} - 1)} + \epsilon_{Br} e^{-\tau Br} + \epsilon_{FB} P_{E,FB} \quad (36)$$

is developed for any radial location in the model profile. This  $\epsilon_T$  includes an additional line radiation attenuation due to collisional quenching where the ion density exceeds  $10^{22} \text{ cm}^{-3}$  (Apruzese, Ref. 8).

With the net loss from each radial location calculated,  $\epsilon_T(r)$  is numerically integrated over the model profile. The total radiative loss thus developed is then bounded above by the equivalent radiation from a cylindrical black body at the current electron temperature.

### C. Time-Dependent Self-Similar Code SPLAT.

#### 1. Operation and Structure of SPLAT.

The implosion code SPLAT can be decomposed into nine distinct sections covering two major calculations. It is equipped with 8 load time parameters (enabling semi-interactive execution and study of results) and 20 input variables modeling various aspects of machine geometry, electrical characteristics, and initial plasma conditions. In the present configuration, it employs a 1D radial fluid grid which is moved in a Lagrangian sense and enables one to track the local neutral plasma position, velocity, and acceleration fields. The ion

density is the fundamental fluid quantity which is evolved, between the radii  $a(t)$ ,  $b(t)$ , in a self-similar fashion. The ion fluid is heated through all appropriate physical processes and cooled through expansion and (indirectly) by radiation. At the present stage of development, the electron density is determined from the homogeneous electron temperature through a simple approximation  $Z (T_e Z_{\max} A)$  and quasi-neutrality,  $n_e = Z n_I$ . The electron heating is by compression, viscous and ohmic heating, as well as by core/coronal heat exchange and radiative losses.

The transition from classical to turbulent current transport occurs at the core/corona boundary  $a(t)$ , and outside  $a(t)$  the appropriate quasi-static coronal pressure balance determines the electron (and ion) density profiles. The coronal electrons are sustained at  $T_2 > T_1$  by enhanced J·E heating as the turbulent region absorbs a larger fraction of the total current, while the coronal ions are assumed nearly isothermal with those in the core due to reduced densities and longer electron-ion relaxation times. Each advance of the core plasma and circuit variables is initiated with a calculation of the internal energy changes in the coronal region, since this is a central and necessary ingredient in evolving  $n_I, r(t), T_1, T_I, I$ . In fact, all core plasma changes  $\dot{T}_1, \dot{T}_I, V(r), \frac{DV(r)}{Dt}$  and overall circuit response  $\dot{I}$  can be calculated from Eq. 50 only when the coronal state is calculated. The sequence of the time derivative calculations at each timestep is therefore immaterial except for the constraints that (i) the corona variables  $\alpha, \dot{\alpha}, g, \eta, \delta, \beta$  are computed prior to the core response  $\dot{T}_1, \dot{T}_I, DV/Dt, \dot{I}$ , and (ii) the radiative losses are computed prior to the core internal energy changes, allowing a properly self-consistent coupling of radiative losses and plasma dynamics.

The two major calculation phases of any SPLAT execution are (i) input and normalization (described in I below) and (ii) evolution forward from the specified initial condition (described in II-IX below). The first phase utilizes the subroutines NORMIT PARCYL PROFILE GRID and SETRPC to initialize a self-similar ion density profile, IONDEN, on the domain RGRID with the characteristic parameters of the profile  $\{\alpha_0, \alpha_1, G_1, G_2, \zeta, \zeta_0, u_0, \sigma_0, C_0, r_2, R_{a-1}\}$  stored in the array PROPAR. The logarithmic gradient  $\partial_r \ln n_I(r)$ , (conserved in strictly self-similar regions) is also evaluated and stored in GRLNNI.

After a report on the initialization, SPLAT begins the second phase and evolves this ion density profile on its mesh, RGRID, using the appropriate self-similarity law. Every five time steps a short report is generated and every thirty time steps a longer, more detailed report is produced. At the time of assembly on axis, a simple collection scheme is employed to fill the central cavity of the annular self-similar solution and smoothly transform it to a simple cylindrical self-similar solution. This process is controlled by the logical assignment SHIFT =.TRUE. After the assembly, the evolution can be followed for as long as desired, determined by initial assignments to the load time parameters LIMTS (limiting time-step  $\leq 1000$ ) and MAXTIM (max. time  $\leq 250$  ns)

i. Input and Normalization: Three namelist files must be supplied:

GEOM = (a b  $\lambda$   $r_w$ ) ,

ELEC = (V<sub>0</sub>  $\gamma$  V<sub>max</sub> I<sub>0</sub> V<sub>p,0</sub> L<sub>D</sub> Z<sub>g</sub>)

PLAS = (A Z<sub>max</sub>  $\rho$  T<sub>1</sub> R<sub>i</sub>  $\dot{a}$   $\ddot{a}$   $\ddot{b}$  n<sub>a,min</sub>);

at load time, the execution command specifies

LIMTS, MAXTIM, LTSP, KCTR, KOPF, KVGs, ITR, MESH

as integer control variables. The more important of these parameters are defined below:

a, b	outer/inner radii of initial core self-similar profile
z	load length
$r_w$	wall radius / "return current" radius
$V_o, \gamma$	estimated lower limits to initial generator voltage/rise time. $V_g(t)$ will determine these in normal operation.
$I_o, V_{po}$	initial current through the load and voltage across it.
$L_D, Z_g$	diode inductance and nominal generator impedance
A, $Z_{max}$	atomic species specification
$\rho$	initial mass density when <u>uniformly</u> distributed on the annulus [a,b]
$T_i$	initial temperature in keV for core electrons
$r_i$	inner radius of core current layer
$\ddot{a} \ddot{b} n_{a,min}$	parameters implying the structural details of any self-similar profile. $\ddot{a}$ determines $\ddot{b}$ <u>initially</u> through Eq. 79. ( $\ddot{a}$ , $\ddot{b}$ ) provide control of the slope of $n_e(r)$ at the inner and outer boundaries. $n_{a,min}$ sets a floor on the boundary density at a in order to avoid an impossible normalization.
LTSP	sets convergence criterion for the time step, e.g., 1000→10% changes, at a maximum, per timestep.
KCTR, KOPF	correction factors to coronal transition layer and opacity calculations
KVGS	control factor on generator voltage time scale
ITR	initial corona/core electron temperature ratio
MESH	number of points desired in the Lagrangian core mesh RGRID, up to a maximum of 51.

Upon input of these namelists and load time parameters, SPLAT assigns initial values for  $\{T_1, T_I, T_2, N_T, r_i, \bar{n}_e, n_{\perp}, \tilde{m}, \tilde{\tau}, Z_1, Z_2, I, \alpha, \varepsilon_0, g, \varepsilon, \dot{a}, \dot{b}, \ddot{a}, \ddot{b}\}$  and calls SETRPC (which then calls NORMIT), GRID, and PROFIL. When normalization is successful (the program stops otherwise), a report of the initial condition is generated. The general format of this report is:

```

a   r_i   b
     r_w
     a   b   a   b
V_g  V_po  I   V_max(t = 31. + MAXTIM)
L_D  Z_g
T_1  T_I  T_2
n_e  S_0  N_T
Z   A   m   tau   Z_1

```

(detailed titles are omitted here) with a listing of RGRID, IONDEN, GRLNNI, and PROPAR, followed by

```
MPTC, S_0, epsilon_0, g, epsilon
```

for the initial normalized state. (MPTC is the grid index of the density maximum;  $S_0$  is the value of  $\tau(a^2 - b^2)$ ).

ii. Scalar Time Derivatives Calculated.

The environment of plasma variables at each timestep is used to produce  $P_{rad}$  ( $Z_2 \dot{T}_2$ ) ( $Z_1 \dot{T}_1$ )  $\dot{T}_I$  and  $\dot{I}$ . The present version of SPLAT first calls ZT2DOT and then uses a simple area weighting  $n_I^2$  to provide a correction factor to the probability-of-escape formalism if  $n_I > 10^{22}$  where quenching is severe. In those time frames for which  $n_I < 10^{22}$  for all radial grid points this additional correc-

tion is not involved and the mean density  $\bar{n}_I = \bar{n}_e / Z$ , is used to evaluate a volume emission rate modified by simple probability of escape factors for a plasma of radius  $a(t)$  and an optical depth computed from  $T_I, \bar{n}_I$ . Once  $P_{rad}$  is calculated, ZTIDOT, TIDOT and IDOT are invoked and an updated set  $\dot{T}_1, \dot{T}_2, \dot{T}_I, \dot{I}$  is available.

iii. Velocity (V), Acceleration (DV/Dt), and (D<sup>2</sup>V/Dt<sup>2</sup>) Fields

The current values of PROPAR,  $\dot{T}, \dot{T}_I, \dot{I}, I$  are used to produce the fields required to push the Lagrangian mesh RGRID. For example, the use of  $G_1, G_2$  defines a field  $V \equiv DR/Dt$ :

$$V(R(t)) = G_1(t) \left( \frac{r(t)}{r_i(t)} \right) + G_2(t) \left( \frac{r_i(t)}{r(t)} \right) .$$

iv. Diagnostic Update

If the calculation is about to advance to a time step index (TSI) divisible by 30, then a vector of diagnostics is prepared for output. This diagnostic array consists of

$$(E_a, E_z, n_{s.p.c.}, r_{corona}/r_w, I_{core, max}),$$

the electric fields on the core surface and outer plasma, the number of sound wave transits across the corona in the time for  $a(t)$  to change by 10%, the corona radius relative to the wall radius, and the maximum current admissible in the core surface if this zone is to remain classical.

v. Time Step Determination ("Update of Pushdown Stack")

In this section the rates of change are surveyed and a time step is chosen on the basis of several criteria:

- (i) fractional changes in the most rapidly varying scalar quantity of the set  $(T_1, T_I, T_2, I)$

- (ii) possible interactions of  $T_1, T_I$  to quench temperature "sloshing"
- (iii) possible zeros in  $\dot{T}_2, Q_{12}$  to quench core/corona energy "sloshing"
- (iv) possible zeros in  $\dot{I}$  to quench corona/circuit energy "sloshing"
- (v) velocities and accelerations on the mesh.
- vi. Advance of Vector and Scalar Fields (includes temperatures and current)

The multi-level integrator advances  $\{T_1, T_I, T_2, I\}$ , while the mesh RGRID is advanced through a third order Taylor series. If the collection process is active in the interior region no mesh advance takes place on those domains.

- vii. Update Plasma Density Variables, etc.

Here the new plasma variables are transformed to those intermediate quantities required to calculate the new rates of change. The ion density array IONDEN is evolved according to the self-similar evolution rule, and the modification of  $\partial_r \ln n_I$  in the current carrying layer is calculated.

- viii. Collection in Central Cavity when required

The collection of matter flowing past an implicitly time dependent radius, ERC, is computed and interior density profiles and gradients are smoothed. The collection persists as long as matter can be drawn onto the central plasma body by a negative  $\nabla P$  force, but it is interrupted (HOLD = .TRUE.) if the local flow field is not directed toward the central plasma.

- ix. Housecleaning and Reporting

Here preparations for the next time step are completed by a call to

SETRPC, and a report is constructed if required. The shorter report output every 5 time steps has the format

a	$r_i$	b	$\dot{a}$	$\dot{b}$	$c_2$
I	$V_g$	$R^*$			
$\bar{n}_e$	$T_1$	$T_2$	$T_I$	$P_{rad}$	$Q_{12}$
t	dt	TSI			
$\ddot{a}$	$\ddot{b}$	$c_1$	B	$Q_{12} - \dot{N}_c Z_2 T_2$	

RGRID

IONDEN

The longer report presents several more details of the evolution, information permitting a cross check of the precision of the integration, the array DIAG, and details of the coronal state, CPV.

## 2. Description of Subroutines and Functions

### (1.) SETRPC - Set radial profile coefficients

- argument sequence: LOGPRO,  $n_a$ ,  $N_T$ ,  $Z_1$ ,  $m$ ,  $T$ ,  $\bar{n}_1$ ,  $n_{\perp}$ ,  $E'_a$ ,  $a$ ,  $r_i$ ,  $b$ ,  $\dot{a}$ ,  $\dot{b}$ ,  $c_1$ ,  $\ddot{a}$ ,  $\ddot{b}$
- output to COMMON BLOCK: DENSI/PROPAR/ and (if LOGPRO = .FALSE.) the argument "a" is overwritten by the subroutine NORMIT
- operational summary: If the initial profile has not been calculated and normalized, SETRPC prepares the common block ZNARG/AS/ for use by NORMIT and then calls NORMIT to adjust "a" until the profile contains a specified linear density  $N_T$ . If the profile has been calculated and normalized previously (LOGPRO = .TRUE.), then only the elements  $\alpha_0$ ,  $\alpha_1$ ,  $G_1$ ,  $G_2$ , (i.e. (PROPAR (1, 2, 3,4))) are updated using the current values of  $a$ ,  $b$ ,  $\dot{a}$ ,  $\dot{b}$ ,  $\ddot{a}$ ,  $\ddot{b}$ .

(2.) NORMIT - Normalize It.

- argument sequence:  $a$   $r_i$   $b$   $\tilde{a}$   $\tilde{b}$   $c_1$   $\tilde{a}$   $\tilde{b}$   
input common blocks ZNARG/AS/, CORO/CPV/
- output: overwriting of argument "a" ; and to COMMON BLOCK: CORO/CPV/  
to update  $\beta$ ,  $g$ , i.e., CPV(5), CPV(6), after a normalization calculation.
- operational summary: NORMIT solves the equation (77) for that value "a" which implies a specific total number of electrons per unit length in the core plasma. AS(1) contains this total number upon any call to NORMIT. The iteration is continued until convergence to four significant figures in the value "a" is achieved or until twenty iterations have occurred. Usually three to seven iterations are quite sufficient to isolate the root; each iteration is reported as a triangle of points enclosing the root and a slope for the hypotenuse of this triangle. The value of the denominator on the right of Eq. 77, with the numerically integrated contribution to it, is reported along with the values generated in PROPAR as the iteration proceeds. If convergence does not occur the final state of the calculation is reported for diagnosis. Since  $n_e(r)$  involves the special function  $U_{\frac{1}{2}}(xR, \mu, \sigma)$  NORMIT calls PARCYL whenever such functions are required.

(3.) PROFIL - Profile

- argument sequence:  $[r]$ ,  $[n_I(r)]$ ,  $[\tilde{a}_r \& n n_I]$ ,  $Z_1$ ,  $\tilde{n}_1$ ,  $\tilde{m}$ ,  $\tilde{T}$ , array dimensions  
input common block: DENSI/PROPAR/

- output: overwriting of the array arguments  $[n_I(r)]$   $[\partial_r \ln n_I(r)]$
- operational summary: PROFIL calculates the explicit self-similar profile for an array of values  $r$  using the parameters stored in PROPAR. It calls PARCYL whenever the special function  $U_{\zeta}(xR, \mu, \sigma)$  is required. It stores these values in  $n_I(r)$ , the array IONDEN from SPLAT. It also computes  $\partial_r \ln n_I$  and stores these values in the array GRLNNI from SPLAT.

(4.) PARCYL - "Incomplete Parabolic Cylinder Function"

- argument sequence:  $[U]$   $[X]$   $R, \zeta, \mu, \sigma$ , array dimensions,
- output: overwriting of the array argument  $[U]$
- operational summary: PARCYL evaluates the special function  $U_{\zeta}(xR, \mu, \sigma)$  by numerical integration. The accuracy of the integration is determined by the variable DG (dimension of the grid), computed externally on the basis of  $\mu$  and  $R$  and bounded above by  $DG_{\max} = 301$ . Seven figure accuracy is easily achieved on a  $2 \left[ 10 + 8 (\mu R) \right] + 1$  mesh for  $x \leq 1$ .

(5.) GRID - Mesh Generator

- argument sequence:  $[r]$   $r_{\max}, r_i, r_{\min}, I_{r_i}$ , points
- output: overwriting of array argument  $[r]$
- operational summary: GRID produces a sequence of equally spaced  $r$  values between  $r_{\min}$  and  $r_i$ , and inserts four points between  $r_i$  and  $r_{\max}$ . The grid then consists of  $(\text{points} - 5)$  values on  $[r_{\min}, r_i]$  and five values on  $(r_i, r_{\max}]$ , for a total of  $(\text{points} - 1)$  zones.

(6.) ZT2DOT - Corona Internal Energy Time Derivative

- argument sequence:  $\bar{n}_1, T_1, T_2, I, E_z, Z_2, Z_{max}, A$   
 $a, r_i, O_p, Z_1, \lambda_T, T_I, E'_a, n_{I,a}, \beta_r, \lambda_n, n_{I,a}$   
input from common block CORO/CPV/:  $S_0, g, \lambda_T, N_{T,C}$   
CPV (3, 6, 13, 10)
- output: to common block CORO/CPV/  $\dot{T}_2, \alpha, \beta, n, n_a, P_{r,2}, Q_{12}, F_{12}$   
CPV (1, 2, 7, 8, 9, 11, 12, 14)
- operational summary: ZT2DOT calculates the coronal equilibrium parameters  $\beta, n, \delta$  (and  $N_{T,C}$  on the first time step). The core (corona density and temperature transition is smoothly connected by conserving  $j_z$  over a narrow region  $\lambda_T$  on the order of a few wave growth lengths. Using the explicit density gradient supplied from the core and differencing over  $\lambda_T$  to estimate the density and temperature gradients at the inner surface of the corona, ZT2DOT distributes the net energy gain or loss over all  $N_{T,C}$  atoms in the coronal equilibrium and generates values for  $(\dot{T}_2, \alpha, Q_{12}, F_{12})$ . The Krook model is applied consistently in all exchange calculations leading to  $Q_{12}$  (kinetic energy transfer) and  $F_{12}$  (particle transfer). The far coronal field  $E_z$  is used to calculate the  $J_z \cdot E_z$  heating and the functions RAD and CORFAC are used to compute the radiative loss from the thin corona.

(7.) CORFAC - Corona Radiation Factor

- argument sequence (r, n,  $\delta$ , term limit)
- output: to function nam, CORFAC

- operational summary: CORFAC evaluates the geometric weighting factor in the net radiative energy loss from a thin isothermal radiator with a density profile  $n_e(r)$  corresponding to the coronal equilibrium configuration given at any time step by  $r, n, \delta$ . This evaluation is accomplished either by hypergeometric series or analytic approximation where appropriate.

(8.) RAD - Radiation

- argument sequence:  $(n_e, Z, A, T_e, \lambda, T_I, O_p)$
- output: to function name, RAD
- operational summary: RAD calculates a frequency integrated volume emission rate for a plasma specified by  $(n_e, Z, T_e, T_I, A)$ . The Bremsstrahlung and recombination losses are presumed thin, while the K, L shell line radiation losses are calculated from an analytic fit to the emission rate results of Duston and Davis (the function DAV\$R) and then attenuated using the probability-of-escape opacity model due to Apruzese. The arguments  $n_e, Z, \lambda, T_I, O_p$  control this opacity calculation;  $\lambda$  plays the role of the physical depth or dimension of the radiating plasma,  $\lambda=0$  results in a thin calculation. Arguments  $n_e/Z, T_I$  are used to calculate an appropriate optical depth and  $O_p$  allows any external calculation of opacity corrections to be included in the attenuation.

(9.) DAV\$R - Line Emission Due to Duston and Davis

- argument sequence:  $n_I, T_e$
- output: to function name, DAV\$R

(9.) (cont'd)

- operational summary: This function fits the K, L shell Al line emission rates calculated by Duston and Davis over the temperatures range  $T_e = (0.010, 9.000)$  keV and scales this emission by  $(n_T/1.0 \times 10^{19})$ . The fit is good to within 8% over the entire range of temperatures.

(10.) ZTIDOT - Core Internal Energy Time Derivative

- argument sequence:  $\bar{n}_e$   $T_I$   $T_C$   $I_1$   $Q_{12}$   $P_r$   $n$   $r_i$   
a b c<sub>1</sub> ä N<sub>T</sub> Z<sub>1</sub> A ä b
- output: to function name, ZTIDOT
- operational summary: ZTIDOT calculates the core heating due to compression.  $[p(\underline{\sigma} \cdot \underline{V})]$ , ohmic dissipation  $[j_1^2 \eta_{\perp}]$ , viscosity  $[\eta_{0\underline{W}} : \underline{\sigma} \underline{V}]$  core/corona energy exchange  $Q_{12}$ , total radiative energy loss  $P_r$ , and ion-electron energy exchange. The net energy gain or loss is distributed over the conserved number,  $N_T$ , of atoms in the core plasma. All radiative loss rates are computed externally using RAD and DAVSR and allowed to enter self-consistently into the internal energy evolution of the core plasma. Under conditions of particularly violent compression, a heating report is printed which shows the relative importance of the various heat sources during the time of interest.

(11.) TIDOT - Core Ion Heating

- argument sequence:  $\bar{n}_e$   $T_I$   $T_C$   $Z_1$   $C_1$   $N_T$   $A$   
a b ä ä b
- output: to function name, TIDOT

(11.) (cont'd)

- operational summary: TIDOT calculates the core ion heating due to compression  $[p(\underline{v} \cdot \underline{v})]$ , electron-ion heat exchange, and, if desired, an enhanced viscosity  $[\eta_0^* \underline{W}: \underline{\nabla} \underline{v}]$  under conditions of rapid compression  $|a| > 1.5c_1$ . The viscosity enhancement is smoothly connected to the classical value as  $|a|$  falls below the current sound speed  $c_1$ . Under conditions of particularly violent compression, the heating report started by ZTIDOT is completed by TIDOT.

(12.) IDOT -  $\dot{I}$ , Calculation from the Circuit Relation

- argument sequence:  $a \quad \dot{a} \quad \alpha \quad \dot{\alpha} \quad r_w \quad \dot{r}_w \quad I \quad R^* \quad Z_g \quad L_D \quad \beta \quad \eta \quad \delta \quad V_g$
- output: to function name, IDOT
- operational summary: This function constrains the time derivative  $\dot{I}$  to be given by the complete circuit equation (50) with all coronal contributions explicitly included. The driving voltage is supplied by  $V_g$  and all other input is derived from the results of ZT2DOT, and preparatory calculations in SPLAT from current values at a given time step. When a decrease in current is imminent, a report of IDOT DATA is generated to allow diagnosis of the factors controlling the "current notch".

(13.) SETST - Set Time-step

- argument sequence:  $a, \dot{a}, \ddot{a}, \ddot{\ddot{a}}, b, c_1$ , convergence and history information
- output: to function name, SETST

- operational summary: SETST surveys the most rapidly varying elements of the evolution and chooses the time step required for a predetermined level of accuracy (the LTSP in SPLAT) in the most rapidly varying of  $(a, T_1, T_I, T_2, I)$ . High frequency exchanges of energy are anticipated and quenched to allow the time step to remain above  $5.0 \text{ E-11 sec.}$

(14.) W\$PUSH - Weights for the Variable Time Step/Multi-time Level Integrator

- argument sequence: [W][h]
- output: overwriting of argument array [W]
- operational summary: W\$PUSH computes the weight factors for advancing  $T_1, T_I, T_2, I$  through the leap-frog integrator  $Y_{i+1} = (\sum_{k=0}^4 W_k \dot{Y}_{i-k}) + Y_{i-2}$ . The variable mesh of previous time steps [h] is required in calculating  $W_k$ .

(15.) ETA - Classical Resistivity,  $\eta_{\perp}$

- argument sequence:  $(n_e T_e Z)$
- output: to function name, ETA
- operational summary: ETA evaluates the resistivity  $\eta_{\perp}$  given by  $\eta_{\perp} = a_{\perp} Z \lambda \ n_e T_e^{-3/2}$

(16.) V - Generator Voltage Model

- argument T in nsec
- output: to function name, V
- operational summary: a piecewise quadratic fit to  $V_g(t)$  due to J. Katzenstein.

### 3. SPLAT Program Flow

READ 3 namelists GEOM, ELEC, PLAS, which  
set generator parameters, initial plasma state.

Initialize  $a, \dot{a}, \ddot{a}, b, \dot{b}, \ddot{b}; n_1, T_1, T_I, r_j, \beta, N$ .

Normalize an initial profile to envelop a specified mass:  $Nm_{A1}$

Call subroutine SETR(adial)P(rofile)C(oefficients),

which call subroutines NORMIT and PARCYL to adjust profile  
width, and evaluate  $G_1, G_2, \alpha_0, \alpha_1$ , (e.g. 31), the elements  
(e.g. 50) output through the common block PROPAR (Profile  
PARAMeters).

Initialize the arrays IONDEN, RGRID, and GRLNNI (gradient of loga-  
rithm of ion density) using the subroutines GRID, PRCFIL, PARCYL

Report the initial state

(A)

Calculate corona parameters using subroutine ZT2DOT, and output through  
the common block C(orona) P(arameter) V(ector) the variables ( $\dot{T}_2, n, \beta, \dot{\alpha},$   
 $Q_{12}, P_{r,2}, F_{12}$ ). ZT2DOT calls RAD (which calls DAVSR) and function  
CORFAC to effect a thin calculation of corona losses.

Calculate the relative opaque volume of core plasma, cf. Eq. (36), for use with probability-of-escape loss calculations,

Calculate core radiative loss  $P_{\text{rad}}$  using RAD and DAVSR.

ZTIDOT calculates  $\dot{T}_1$ , using the present heat flow  $Q_{12}$ , radiated power  $P_{\text{rad}}$  and fluid plasma parameters.

TIDOT calculates  $\dot{T}_I$  for the present fluid plasma parameters.

Calculate  $\dot{r}_i$  from the present flow field in common block PROPAR, and the appropriate  $\dot{g}$ .

Calculate the total  $\dot{I}$  using the complete core/corona circuit equation and the present values of  $g, \dot{g}, \alpha, \dot{\alpha}, \beta, \delta, n, R^*$ , using the function IDOT.

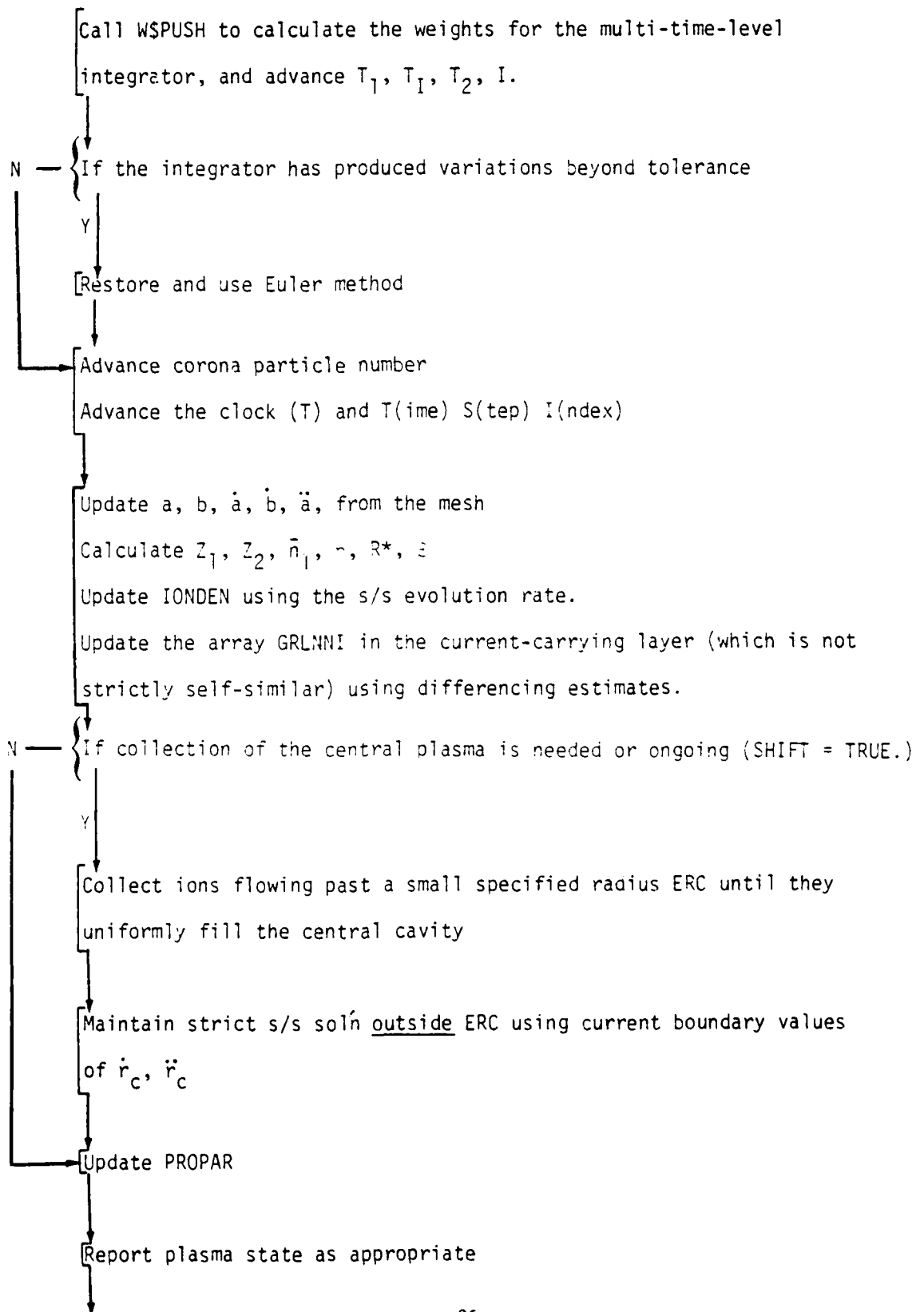
Prepare to advance the Lagrangian mesh RGRID using the self-similar velocity fields AVSSC (-, 3), and acceleration fields AVSSC (-, 4).  
 AVSSC (-, 5) calculated from PROPAR.

Prepare the array DIAG if required (every 30 time steps) for printout

Push down the multi-time-level stack of  $\dot{T}_1, \dot{T}_I, \dot{T}_2, \dot{I}, T_1, T_I, T_2, I$ , the sequence of heat flows Q12\$, and the sequence of time steps H\$

Inventory the rates  $\dot{T}_1/T_1, \dot{T}_I/T_I, \dot{T}_2/T_2, \dot{I}/I$  and calculate the time step using SETST(ep) for DT.

Advance the portion of RGRID not involved in collection and predict new velocities AVSSC(-,2) and accelerations AVSSC(-,1) for the zone boundaries a and b.



AD-A131 175

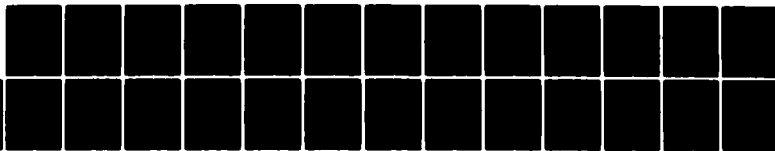
DEVELOPMENT AND EXPLORATION OF THE CORE-CORONA MODEL OF  
IMPLoding PLASMA LOADS(U) JAYCOR ALEXANDRIA VA  
J GUILLORY ET AL. 01 JUL 80 JAYCOR-TPD-200-80-001-DFR  
DNA-5234F DNA001-79-C-0189

2/2

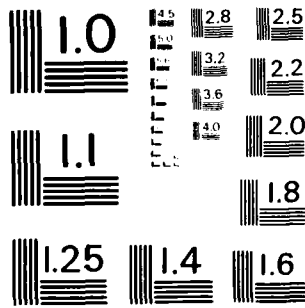
UNCLASSIFIED

F/G 18/3

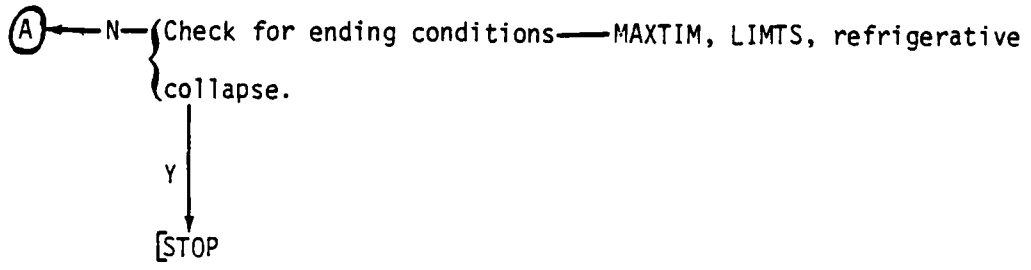
NL



END  
DATE  
FILMED  
DTIC



MICROCOPY RESOLUTION TEST CHART  
NATIONAL BUREAU OF STANDARDS - 1963 - A



#### 4. Advantages and Disadvantages

##### Advantages:

- (i) Economy of computation (1c/time step)
- (ii) Relative simplicity in treating new physics (zone/module structure)
- (iii) No arbitrary multipliers on transport coefficients
- (iv) A class of initial conditions of specific form that are subject to experimental constraint, reducing the dimension of the free parameter space
- (v) Potential generalization to 2 and 3 dimensions with even greater relative computational economy.

##### Disadvantages:

- (i) Breakdown of self-similar motions upon collapse should be treated with more general fluid/kinetic theory, but the self-similar regions allow simple dynamic calculations and free the more delicate methods to concentrate on the special cases. This implies less computation for any fixed precision or more precision for a fixed level of computational effort.
- (ii) The very stiff set of non-linear differential equations requires delicate integration methods. Particularly if extended into domains of sharp gradients and many orders of magnitude in density, the tracking of widely separate rates for various energy/momentum exchanges is the most difficult aspect of the calculation.

## V. SCALING AND GUIDELINES BASED ON CORE-CORONA MODEL AND CODES

### A. Interpretation of Code Results.

#### 1. Initial Conditions.

The self-similar initial-condition relations discussed above allow a wide class of initial core states, and there is little experimental information to provide more than a rudimentary guide to their selection. The parameters of the self-similar profile  $\alpha_0$ ,  $\alpha_1$ ,  $G_1$ ,  $G_2$ ,  $\bar{m}$ ,  $\bar{T}$ , and  $E'_a$  are chosen for the code runs on the basis of reasonable criteria, but are not as yet intended to duplicate any particular laboratory implosion.

In particular, one wishes an initial profile exhibiting: (i) confinement to a narrow annulus, (ii) expansion velocities on the order of the sound speed, (iii) expansion velocities compatible with initial temperatures (of order 10eV), (iv) initial currents compatible with the generator voltage and network parameters, and (v) a specific total mass. The term "compatible" means that in a practical sense one must search the parameter space a bit with each fresh profile constructed, usually adjusting  $\bar{a}$ ,  $\bar{b}$ ,  $I$  in order to achieve satisfactory confinement. The choice of  $r_i$ , the extent of radial penetration of the driving electric field prior to freezing these fields to the fluid flow, is also relatively unguided by direct experimental input. At the temperatures considered, the resistivity is so low as to force any statement of  $r_i(t_0)$  to be a statement about the early time development of melting, vaporization, expansion and ionization. None of these transitions are intended to be a part of this model and thus their end results are treated as simple input data. For example at 32 ev, a skin depth of  $8.4 \times 10^{-3}$  cm is well within reason for times as late as 45 ns into the implosion phase where the self-similar model could reasonably be expected to accommodate

the physics. The selection of the present initial profiles as physically appropriate rests on the suppositions that: (i) the early fluid development passes through a state of large viscosity (relative to the classical plasma value) and (ii) such viscous stresses act to bring the density and flow-field profiles into the forms used here. Whatever the detailed time development in the early phases, the restriction to such a class of profiles is a relatively weak one. It implies generation processes which provide a continuum of initial values, e.g.,  $r_I$ ,  $\ddot{a}$ ,  $\ddot{b}$ , and which admit further experimental investigation.

The fixed initial mass is taken to be that of a 24-wire array of 1.5 mil Al wires 3 cm long. This is used by the normalizing algorithm discussed above and is a conserved quantity in the calculation. The structure of two such self-similar profiles is shown in Fig. (3a,b) for initial temperatures of 15 eV. The smaller-radius profile initially confines most of the mass between 0.60 cm and 0.76 cm, the larger-radius one, between 0.92 cm and 1.09 cm. Both profiles contain  $1.5023 \times 10^{19}$  ions per cm of discharge length. The initial penetration of the current layer is indicated at 0.60 cm and 0.95 cm, respectively.

## 2. Classes of Trajectories.

In the studies detailed below, one can identify three general classes of implosion trajectories, as defined by the position of the density maximum  $r_m(t)$  in the self-similar profile. The first is a simple refrigerative collapse (SC), in which the implosion picks up energy from the generator, builds inadequate retarding pressure, and quickly radiates this energy away as it is thermalized. Under these conditions, the plasma is smoothly driven into the origin by  $\underline{J} \times \underline{B}$  forces without evidencing any retarding

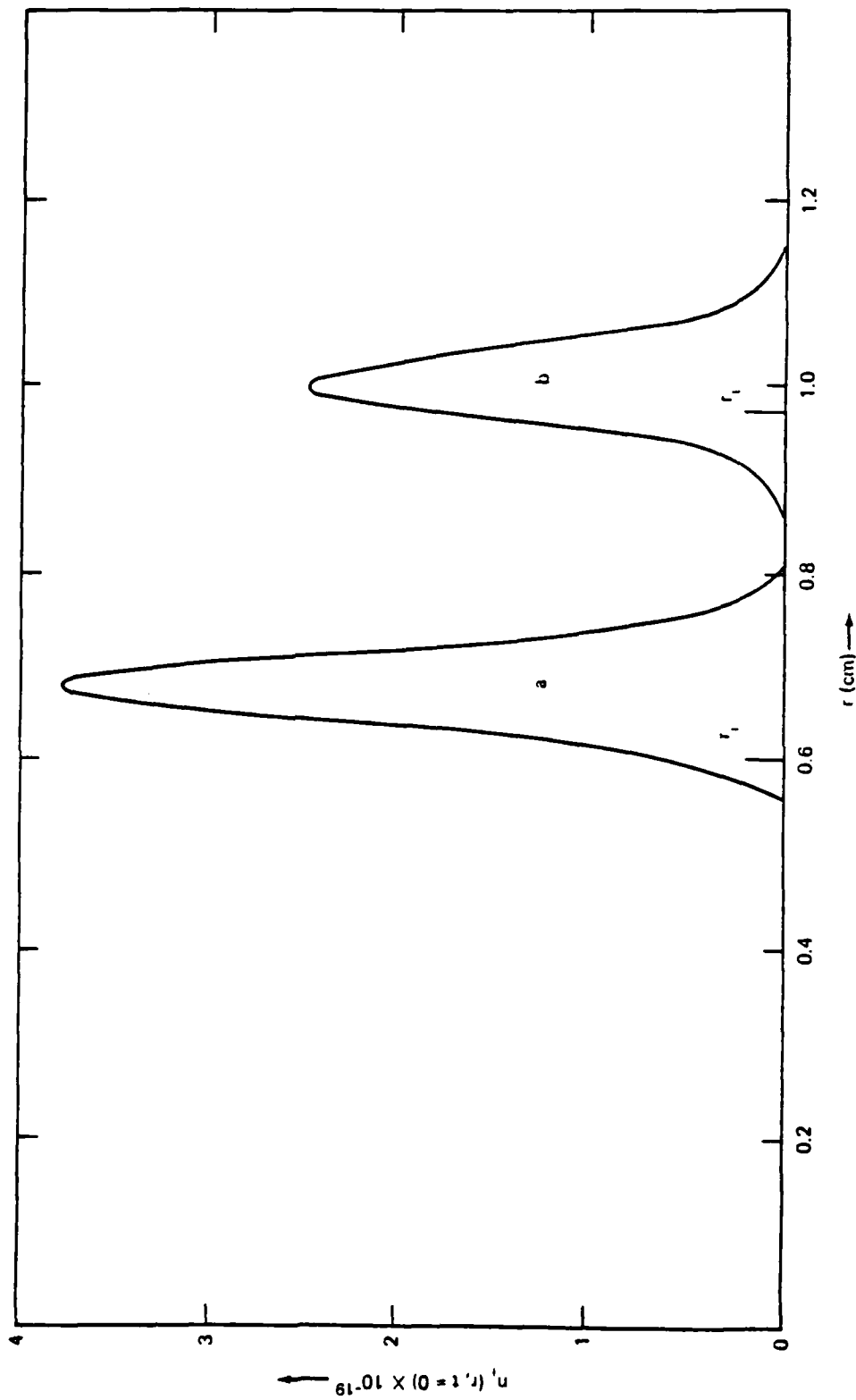


Figure 3 a,b. Two "initial" ion density profiles for different SPLAT-ID code runs. Initial temperatures were taken to be 15 eV. The assumed initial current-penetration radius,  $r_i$ , is shown for both.

pressures large enough to cause deceleration. The second type of trajectory pauses and collapses (PC), where the rapidity of heating allows retarding pressures to build up and slow the implosion velocity by a factor of 2 or more. In this class the radiation output becomes slightly broader in time and larger temperatures are seen (nearly coincident) with the radiation peak. A third type of trajectory involves more significant bounce before collapse (BC), and runs with higher peak temperatures and faster generator risetime fall into this latter class. The bouncing occurs in the zero-D model also, and is more asymmetric in time if the outward pressure gradients after implosion are more pronounced; the bounce is held to smaller radii only if the energy feeding expansion is removed rapidly enough by the radiative losses. Bounce trajectories without collapse, although not seen in the present study, can be generated for weak or rapid generator pulses.

The density and temperature trajectories, which determine the radiation pulse width and amplitude, are similar for the SC and PC paths, and distinct from those of the BC paths. In the case of the former, all densities on the profile increase monotonically with time after the initial expansion phase of the annulus. The temperatures peak just prior to peak assembly on axis, shortly before the maximum radiative losses. In the BC case, the densities rise until the bounce occurs, after which there is a smooth decay and subsequent recompression. The temperatures are observed to rise and fall smoothly through the initial bounce, only to rise again from small values ( $\sim 30$  eV) with the final compression and collapse.

In all cases, some time asymmetry of the radiation pulse occurs because the rise time is determined by the plasma compression time scales, but the decay is determined mainly by the large radiative loss rate which is very sensitive to even the slowed compression or expansion of the pinch. The mix of line (K, L shell) and continuum radiation tends to favor the

continuum at the peak of emission because the high densities  $n_T \sim 3 \times 10^{19}$  imply very high line opacity. In the absence of motional broadening, a mix favoring line emission will be obtained for milder compression, i.e., bounce or pause at earlier times and larger radii, or for warmer plasma. Larger initial temperatures in the annulus, perhaps 50 eV - 70 eV, tend to alleviate this behavior, but many alternative factors can play a significant role.

The time-integrated yield (integrated over all photon energies) is sensitive to the maximum implosion speed achieved, whether by faster rise times in the generator (larger forces), or by a longer distance over which to act (greater initial radii). In the case of PC trajectories there will tend to be a short, cold after-pulse following the main radiation pulse, caused by the "last gasp" of the system as collapse occurs. The contribution to the yield from a single such pulse is small, but if the initial bounce point is approached slowly there may exist implosion trajectories which hold at moderate radii for some time, radiating more slowly and bouncing gently, perhaps many times. Under these conditions the collapse could be stretched out and the contribution to the yield due to this late time behavior would increase. However, this contribution is at photon energies considerably less than 1 keV.

### 3. Illustrations of the Dynamics.

The typical SC trajectory is shown in Fig. 4a, starting from the initial state of Fig. 3a. The largest implosion speed of the density maximum is about  $1 \times 10^7$  cm/sec and the peak temperature on axis is 338 eV. The current notch due to motional impedance is not pronounced.

The typical PC trajectory is shown in Fig. 4b, starting from the initial state of Fig. 3b. The largest implosion speed of the density maximum is about

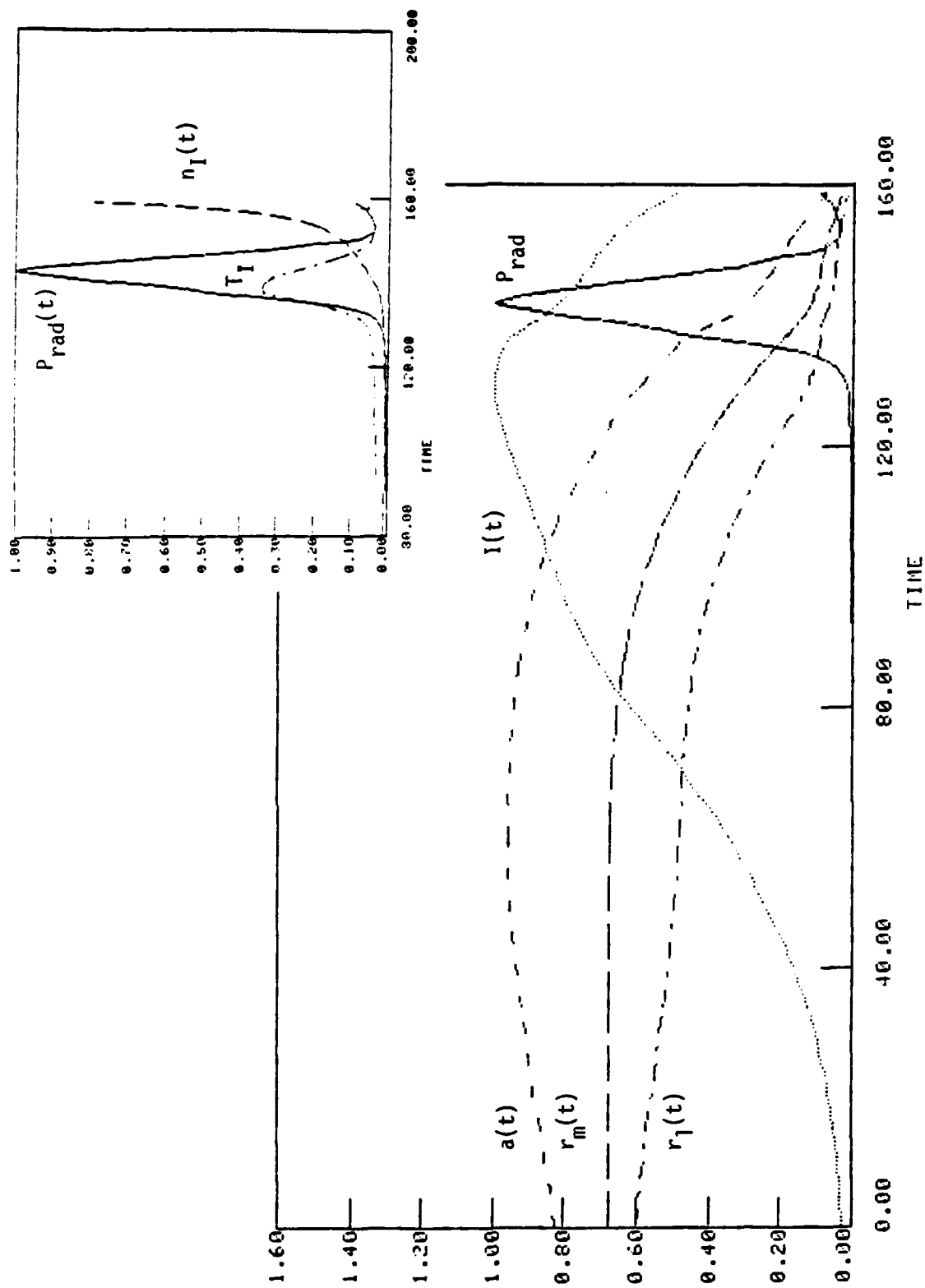


Fig. 4a. Simple collapse (SC) evolution of  $r_i$ ,  $r_m$ ,  $b$ ,  $I$ , and  $P_{rad}$ .  
 Insert shows the relation of  $P_{rad}$  to ion temperature and spatially averaged ion density.

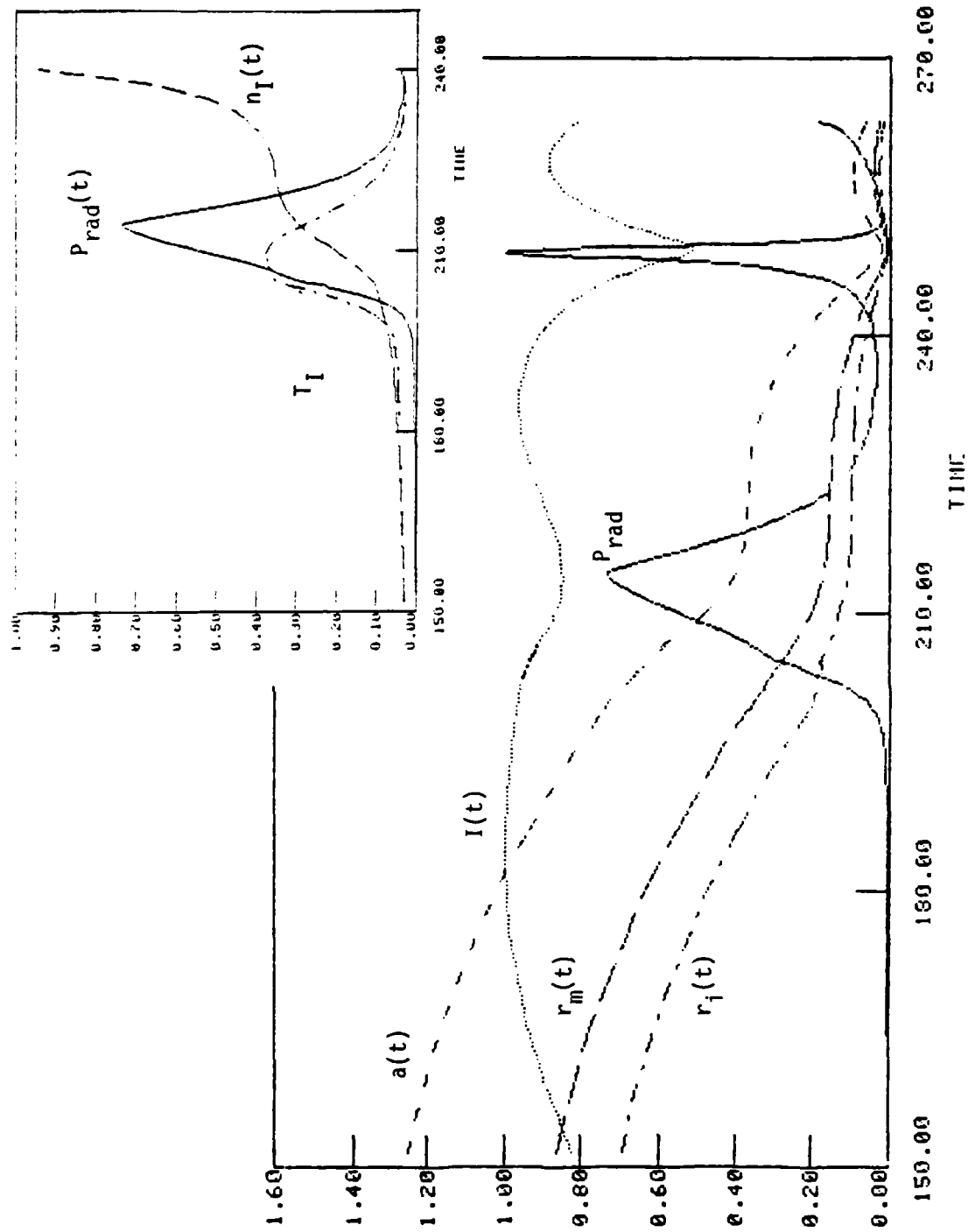


Figure 4b. Pause-and-collapse (PC) evolution of  $r_i$ ,  $r_m$ ,  $b$ ,  $l$ , and  $P_{rad}$ .  
 Insert shows the relation of  $P_{rad}$  to ion temperature and spatially averaged ion density.

$2 \times 10^7$  cm/sec and the peak temperature on axis is 378 eV. The current notch is relatively weak, subtracting about 10% of the previous maximum driving the implosion; but the current trace recovers to 100% of this previous current maximum. Even though the generator voltage continues to rise, the "impedance" of the array increases significantly as the radius decreases. In the first of the cases illustrated, the core current fraction,  $\beta$ , is approximately 0.7, but the coronal temperature never exceeds 10 keV. In the second,  $\beta$  is bounded above by 0.9, and  $T_2$ , again by 10 keV. Both cases were run with good initial current penetration into the core plasma.

Figures 5 and 6 illustrate the effect of variations in generator rise time. The yield dependence on the generator timescale is shown for several cases with the initial conditions (Figures 3,a,b, etc.) and clearly indicates that too rapid a coupling degrades the yield at some point. The generator rise times were varied using a simple multiplication on the time scale of the driving function  $V(t)$ , i.e.,  $V(t) \rightarrow V(\alpha t + 31.0 \text{ nsec})$ ,  $\alpha = 0.5$  to 1.6 in intervals of 0.1. (Figure 5.) The yield degrades for the faster time scales, because the generator then can heat the plasma earlier in assembly phase and cause it to expand before reaching as high a density (Fig. 6). This provides higher temperatures, but generally lower densities and keeps the overall radiated energies smaller.

Note that the radiated energy plotted in Fig. 6 (and the radiated power in Figs. 4a and 4b) are frequency-integrated values, without any cutoff, and do not represent experimentally measured radiation passed first through filters. The radiation package of the code is presently being reconfigured to give output separately in two frequency "bins".

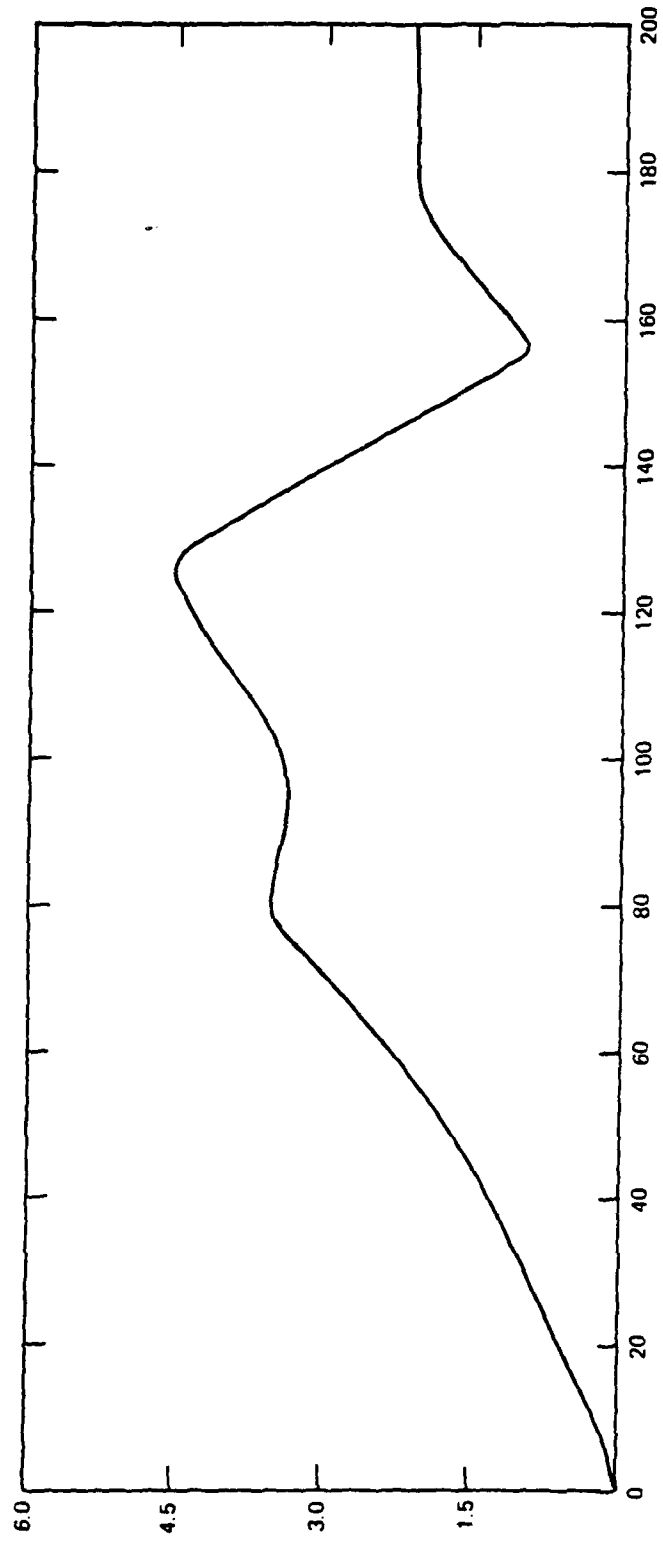
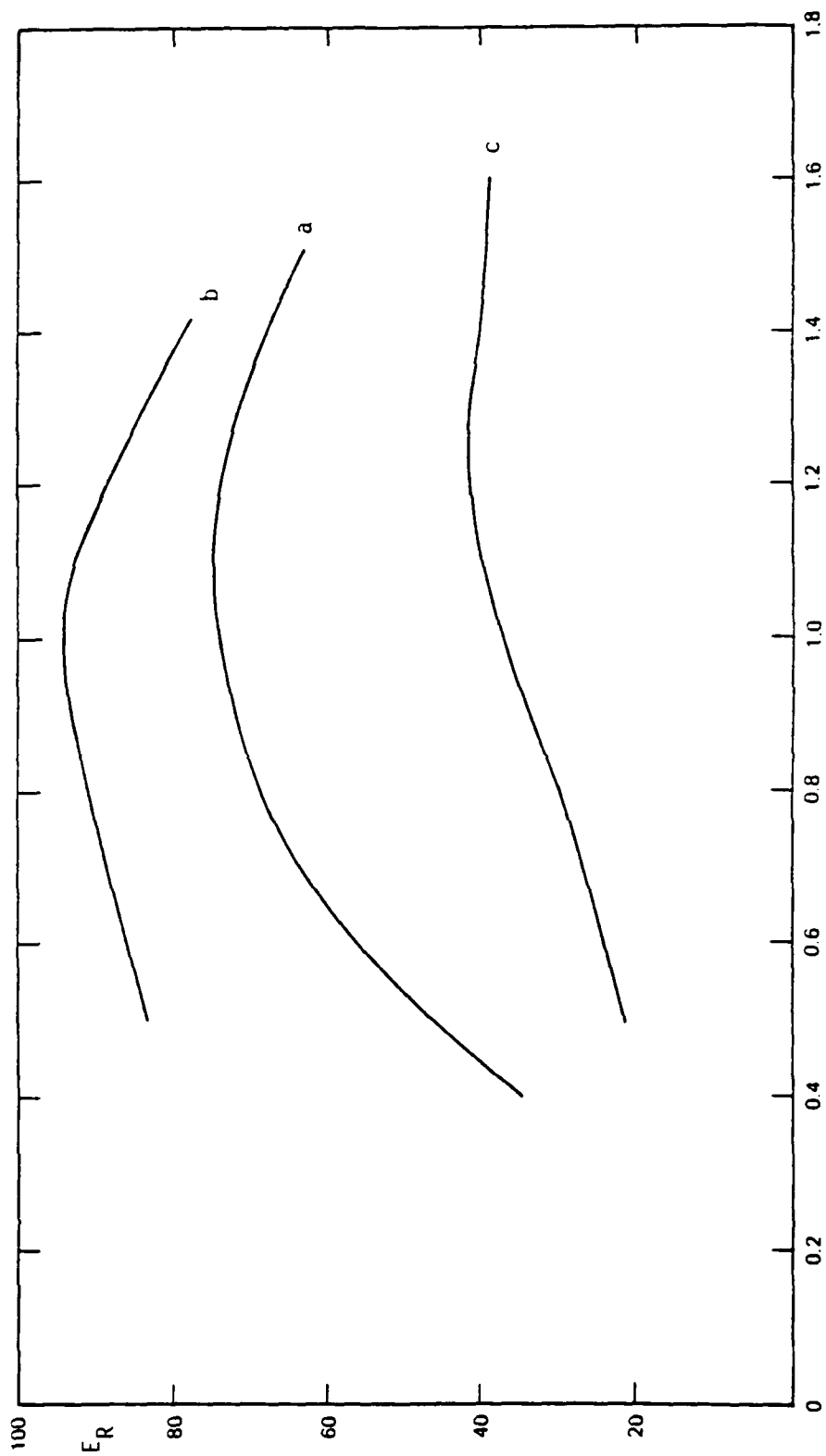


Figure 5. Generator voltage vs time for  $\alpha = 1.2$  (1.2 x faster than normal pulse).



$\alpha \rightarrow$  Figure 6. Frequency-integrated radiative yield vs generator rise-rate multiplier  $\alpha$ , for three initial configurations:

(a) that of fig. 3a, (b) that of fig. 3b, and (c) a smaller radius array with peak at 0.3 cm and width 0.1 cm, but the same mass as 3a and 3b.

#### 4. General Comparison of Zero-D and 1-D Formulations.

The use of a continuous profile for the core density provides an important correction to the dynamics of the implosion. It is clear a priori that the mechanism for coupling generator fields to radial fluid momentum is a major determinant of the dynamics, but it is obvious after some experience that this is the single most important facet of the problem. The use of explicit pressure gradients and the propagation of external  $J \times B$  stresses to the local density maximum allows the model plasma to respond to the "magnetic piston" by a smooth inward drift reflecting the appropriate inertia and by relative compressions/expansions reflecting the density profile. The simple spatially integrated model only allows the average inertia to enter and accelerates the inner surface independently of the pressure gradient. This results in larger implosion speeds, higher temperatures, and shorter radiation pulses as can be seen from the dynamics presented in previous sections. On the other hand, the smooth 1D version prevents such large transfers of radial momentum.

The second most important correction is the opportunity to do a detailed calculation of the radiative losses. From the simple picture, we concluded that proper opacity calculations are very important in the model dynamics because energy not radiated remains to provide more retarding pressure (directly or indirectly) and slows the time scale of the radiation pulse.

The third correction is embodied in the core/corona heat exchange calculation discussed above. This energy exchange plays a major role in determining  $\beta$  and, thus, in modifying the  $\underline{j} \times \underline{B}$  force driving the core implosion. In contrast to previous calculations, the present 1D version allows for particle interchange at the core/corona boundary and provides a cooler corona, less susceptible to "exploding". The cooler corona now tracks the core temperature more closely and is less extended spatially than in the previous version of this model. In fact the corona now resembles a thin zone of turbulent current transport capable of accepting essentially all of the current required by the generator field in order to satisfy the circuit relation. This coronal region is not spatially extended because the pressure balance assumed in its construction does not require a broad spatial region at the temperatures, currents, and core skin depths encountered. The problem of experimental examination of this region thus becomes more delicate.

For the model as presently implemented, it is possible to search for surfaces in the initial-condition space that imply the bifurcation of trajectories among the SC/PC/BC classes. For the previous version of the code, this was not useful and not easily done because of the extreme sensitivity to the radiative losses discussed above in regard to the "exploded corona" problem. Such partitioning of the initial-condition space will provide a useful guide in constructing scaling laws and in estimating the performance of alternate generator and load configurations, because the most physically appropriate trajectories (for any radiative loss approximation) will be those near the PC/BC bifurcation. Moreover, it appears that some function of  $(\tilde{T}, \beta, r_m)_{t_0}$  will provide this surface (for fixed generator

parameters) so that inference back to initial conditions may be drawn from later performance, or the domain of initial conditions limited based upon knowledge of particular performance criteria.

In addition to improved radiative loss calculations, there remain many areas for improvement in the self-similar model, most notably the inclusion of magnetic diffusion, improved dynamics in the current-carrying layer, an equation of state that is coupled to the photoionization process, and a continuous radial velocity profile for the core/corona interface. In addition, the performance of the 1D code suggests that some direct dissipative mechanism for radial momentum may be required in order to bring the model into detailed agreement with experiment. If such a mechanism is found then the PC/BC bifurcation surface will tend to widen into a zone of finite measure and soften the present sensitivity to the initial conditions. These problems will be addressed in the coming months, as well as extensions of the core self-similarity model to allow axial or axial/azimuthal variations.

#### B. Analytic Modeling for Scaling Laws.

Our code and analysis during this contract period have not addressed the early-time history of the wire array, (e.g., melt and initial expansion of the plasma about each wire). Analysis and computation begin from an assumed (but self-consistent) cylindrical-shell-like distribution of cool plasma, with specified density profiles in pre-formed core and corona regions, and specified temperatures. We do not yet know of complete models for the early-time history, although certain features appear to be described by the work of Bloomberg et. al. (Ref. 11).

Side by side with the more complete analysis embodied in the SPLAT code and its equations, we have attempted to formulate a much simpler set of model equations, simple enough to give various analytic scaling laws for the collapse time, radiation pulse duration, radiated energy, and temperature. These models, necessarily oversimplified in order to give analytic results, may be useful for making some further approximations in the code, and for predicting order-of-magnitude results and large-scale dependence on input parameters (mass  $m$ , initial radius  $r_0$ , atomic weight  $A$ ) and generator parameters (peak voltage  $V_0$ , voltage rise time  $\tau_g$ , generator impedance  $Z_g$ ).

The physics of the system depends more simply on the current  $I(t)$ , peak core density  $n_1(t)$ , and peak implosion velocity  $V_1$ , corona 'boundary' density  $n_a(t)$  and corona scale height  $\delta(t)$  — all of which are related to the input and generator parameters by differential equations without simple analytic solutions. It is our hope eventually to have heuristic fitting functions relating these physical parameters to the input and generator parameters, as a result of large numbers of code runs. Difficulties in the code development have prevented our having enough runs yet to report real achievement of this objective, although we do not see fundamental obstacles. Preliminary scaling, demonstrated from a relatively few runs is shown in Fig. 6.

#### 1. Collapse-Phase Models.

A simple model represents an extreme in bounding the collapse-phase behavior. Plasma pressure and corona current are ignored, and the core-plasma shell is accelerated inward by only the  $\underline{j} \times \underline{B}$  force due to current in the skin layer, whose thickness is assumed to be "frozen-in" by the plasma

temperature so that the thickness  $a(t) - r_i(t) = f a(t)$  with  $f$  a constant. The equation for the outer radius  $a$  is then

$$- a^3 \ddot{a} = (\pi m c f)^{-1} I^2(t) , \quad (87)$$

if plasma compression during run-in is neglected (until assembly on the axis). In the preliminary code runs,  $I(t)$  appears to be nearly linear during the collapse phase, i.e., the effective total impedance appears to be nearly constant. Using the simple form  $I = \dot{I} t$  in Eq. (87) gives an equation of the form  $x^3 \ddot{x} = - t^2$ . The dimensionless time to collapse to the origin is then a number of order unity, obtainable by numerical solution, and the real collapse time scales as  $a_0 \dot{I}^{-1/2} (m f)^{1/4}$ . The more complex form with  $I$  given by

$$Z_g \dot{I} + L_g \ddot{I} + (R + \dot{L}) I = V_g(t)$$

and with load inductance modeled by  $L = L_0 - k \ln(r/r_0)$ , does not give readily scalable results.

## 2. Simplified Assembly Model.

In the simplest approximation, we may imagine a more-or-less uniform core plasma with radius  $r(t)$  and temperature ( $T_e = T_i$ )  $T(t)$ , with the origin of  $t$  taken to be the beginning of the assembly (i.e., we assume a sharp assembly beginning at  $t = 0$ ). We will use two simultaneous ordinary differential equations to describe, in a simplified way, the evolution of  $r(t)$  and  $T(t)$ . The core current fraction  $\beta$  will enter in general as a parameter in both equations; but, to the extent that the corona has robbed the core of both its  $\underline{J} \times \underline{B}$  compression force and its ohmic heating, the magnitude and effect of  $\beta$  will be reduced.

The force equation has two force terms: the outward  $2\pi r p = 2\pi r n T$  with  $n = n_i + Z(T)n_e$ , and the  $2\pi r B^2/8\pi$  magnetic compression force with  $B = 2BI(t)/cr(t)$ . The density  $n_i$  is given by  $N/\pi r^2(t)$  with fixed  $N$ .

The energy equation has an assembly heating term representing the conversion of kinetic energy  $\frac{1}{2} \dot{m} r^2$  into thermal energy  $\frac{3}{2}(n_i + Zn_i T)$  and ionization potential energy  $\epsilon_i(Z)n_i T$ , and has radiative cooling terms corresponding to line radiation with a line-average opacity factor, recombination radiation, and bremsstrahlung, which will be allowed to escape unattenuated. The radiative power expressions are modeled by:

$$P_L(W) = \pi r^2 \lambda \cdot 4.73 \times 10^{-25} n_i^2 Z F_L(T) P_E \quad (88)$$

$$\text{with } p_E = .286 \tau^{-1} (\ln 2\tau)^{-1/2}, \text{ the line photon escape factor,} \quad (89)$$

$$\tau = 79.2 r_{\text{cm}}^{-1} T_{\text{keV}}^{-1/2} [10^4 \text{ m(g)}/\lambda(\text{cm})] , \quad (90)$$

$$F_L(T) \text{ approximating the results of Duston \& Davis (Ref. 19) and} \\ \sim T_{\text{keV}}^{-1/2} \text{ for } T \geq 1 \text{ keV,} \quad (91)$$

$$\text{and } Z(t) \approx \zeta T_{\text{keV}}^{1/3} \text{ for } .03 < T_{\text{keV}} < .25 , \quad (92)$$

$$P_R(W) = P_B \times \text{Min} (3, 2T_{\text{keV}}^{-1/3}) \quad (93)$$

$$P_B(W) = \pi r^2 \lambda \times 4.74 \times 10^{-31} n_i^2 Z^3 T_{\text{keV}}^{-1/2} . \quad (94)$$

Upon specializing to Aluminum ( $\zeta \approx 21$ ) and expressing all times in 'shakes', i.e., units of  $10^{-8}$  sec (the natural units for the problem), we have the following pair of simultaneous ordinary differential equations:

$$\ddot{r} = K_p r^{-1} T^{4/3} - K_M r^{-1} T^3 \quad (95)$$

$$T^{1/3} \dot{T} = -K_A \dot{r} \ddot{r} - K_L r^{-1} [K_T - \ln(r T^{1/2})]^{-1/2} F_L(T) T^{1/2} \\ - K_R r^{-2} T^R - K_B r^{-2} T^{3/2} + K_\Omega IV = \frac{1}{2} K_A \dot{r} r^{-1} \quad (96)$$

with T in keV, r in mm, I in MA, V in MV, and with:

$$K_p = 15.5 \quad (\text{Pressure expansion factor}) \quad (97)$$

$$K_M T^3 = 1.0 \beta^2 I_{MA}^2 \mu^{-1} \quad (\text{Magnetic compression coef.}) \quad (98)$$

$$K_A = 2.0 \zeta^{-1} = .095 \quad (\text{Assembly heating coef.}) \quad (99)$$

$$K_L = 1.97 \times 10^{-4} \quad (\text{Line rad. coef.}) \quad (100)$$

$$K_B = 10.9 \zeta^2 \text{ m}/\ell = 0.48\mu \quad (\text{Bremsstrahlung coef.}) \quad (101)$$

$$K_R \approx 3 K_B \text{ for } T < .3, 2 K_B \text{ for } T \geq .3 \quad (\text{Recomb. rad. coef.}) \quad (102)$$

$$K_\Omega = 0.65 \beta / 10^4 \text{ m}(g) \quad (\text{Ohmic heating coef.}) \quad (103)$$

$$K_T = 8.06 + \ln \mu \quad (\text{Optical depth factor}) \quad (104)$$

$$\mu = 10^4 \text{ m}(g) / \ell(\text{cm}) \quad (\text{Mass coef.}) \quad (105)$$

$$R = 3/2 \text{ for } T < .3, 7/6 \text{ for } T > .3 \quad (\text{Exponent for recomb.}) \quad (106)$$

Once the temperatures reach 0.24 keV, the  $T^{4/3}$  and  $T^{1/3} \dot{T}$  are replaced by  $.62T$  and  $.62\dot{T}$  respectively. (This assumes that all the atoms are in the average ionization state  $\bar{Z}$  and that above 240 eV the Al is stripped). Here the coronal effects enter via the unspecified parameter  $\beta = I_{\text{core}}/I_{\text{total}}$ .

From the coefficients in this form, one sees that for  $m \sim 10^{-4} \text{g}$ ,  $l \sim 3 \text{cm}$ ,  $r_1 \sim 1 \text{mm}$ ,  $T_0 \sim 0.1 \text{keV}$ ,  $I \sim 1 \text{MA}$  and  $V \sim 1 \text{MV}$  one will have "initially" at the beginning of assembly

$\ddot{r} \sim [0.7 - (3)\beta^2] \text{mm/sh}^2$	acceleration
$-K_A \dot{r} \ddot{r} \sim .07  \dot{r}_1  (\text{mm/sh}) \cdot (1 - 4\beta^2)$	PdV heating, if $\frac{d}{dt}(\dot{r}^2) < 0$
$K_\Omega IV \sim 0.7\beta$	Ohmic heating
$K_B r^{-2} T^{3/2} \sim .005$	Bremsstrahlung cooling
$K_R r^{-2} T^R \sim .015$	Recomb. rad. cooling
$K_L r^{-1} F_L(T) T^{1/2} K_T^{-1/2} \sim .023$	Line rad. cooling

If  $\ddot{r}$  remained constant, a minimum radius

$$r_{\text{min}} \sim r_1 - \frac{1}{2} \dot{r}_1^2 [0.7 - (3)\beta^2]^{-1} \quad (107)$$

would be reached in a time

$$t_a \sim |\dot{r}_1| [0.7 - (3)\beta^2]^{-1} \quad (108)$$

If radiation cools  $T$  faster than  $r^{-1}$  can increase, then the  $r_{\min}$  is smaller (cooling then even faster) and  $t_a$  is shorter; so the condition for refrigerative collapse with small  $\beta$  is approximately that

$$K_p r^{-1} T^{4/3} \text{ decreases on the timescale } |\dot{r}_1|/K_p r^{-1} T^{4/3}.$$

$$\text{i.e., } \left| \frac{4}{3} \frac{\dot{T}}{T} + \frac{(-\dot{r})}{r} \right| > \frac{4}{3} K_p r^{-1} T^{4/3} |\dot{r}_1^{-1}| \quad (109)$$

assuming  $|4\dot{T}/3T| > (-\dot{r})/r$ . This is clearly easier when  $|\dot{r}_1|$  is large. When such a collapse occurs, all the kinetic energy of implosion is converted into radiation, as well as the initial thermal and ionization energy. The fate of the magnetic energy depends on the behavior of  $\beta I$  during such a collapse.

But the amount of radiated energy coming out at energies above, say 1 keV, depends mostly on the history of radiation before the plasma cools to  $T \sim 300$  eV, and the exponentially small number of  $\sim 1$  keV transitions excited in a plasma of  $T < 300$  eV. Thus, the experiments optimizing radiation above 1 keV will be those that get the plasma hotter than about 300 eV before or during collapse, and have low enough densities at assembly to prevent radiation cooling below 300 eV on a fast timescale. Regarding this threshold temperature  $T_\theta$  as a parameter, one wishes to maximize

$$\int_{[T > T_\theta]} dt \left[ K_L K_T^{-1/2} r^{-1} F_L(T) T^{1/2} + K_R r^{-2} T^R + K_B r^{-2} T^{3/2} \right],$$

in other words, if  $\beta$  is small, maximize

$$\int_{[T > T_\theta]} \left[ K_A K_P (-\dot{r}/r) + (-\dot{T}/T) \right] T^{4/3} dt. \quad (110)$$

Here  $-\dot{r}/r$  is approximately the inverse of the compression timescale, and  $-\dot{T}/T$  the inverse of the net cooling timescale (dominated by radiative cooling).

Note that, because of the large opacity factor in the line radiation and the  $Z^3$  dependence of bremsstrahlung (as opposed to  $Z^1$  dependence in the line radiation), the line and continuum cooling rates may be comparable. Note also that the simultaneous equations for  $\ddot{r}$  and  $\dot{T}$  in even this oversimplified model are complex enough, and  $F_L(T)$  is complex enough, that no simple scalings beyond the ones just discussed can be obtained. As a simple rule, we have a radiation pulse length

$$t_a \sim |\dot{r}_1|/\ddot{r} \sim |\dot{r}_1| r_1 K_p^{-1} T_1^{-4/3} \quad (111)$$

and a total radiated energy of order  $\frac{1}{2} m \dot{r}_1^2$ , but the radiative yield above a threshold  $T_\theta$  cannot be derived as a simple function of  $m$ ,  $\lambda$ ,  $V$ ,  $I$ , and the generator risetime.

The differential equations of this model were solved for certain cases with only bremsstrahlung cooling and with  $\beta = 0$ . "Initial" velocities just prior to collapse were set at values of order  $10^7$  cm/sec and initial temperatures at values of order 0.1 keV. Transparent bremsstrahlung alone was then enough to induce simple collapse trajectories, in which radiation cooling dominated the thermal energy input from the collapse. The deceleration due to plasma pressure even without any opposing  $\underline{j} \times \underline{B}$  force was insufficient (by an order of magnitude) to prevent the density buildup responsible for the cooling. In order to do so, the peak density-squared, proportional to  $[r_1 - (\sim 1)\dot{r}_1^2]^{-2}$ , had to be lowered by two orders of magnitude (as achievable when  $\dot{r}_1 \sim 0.3$  mm/shake).

### 3. Radiation Scaling Model.

Mosher (Ref. 5) has derived radiation scaling with wire mass  $m$  and assembled radius  $r_1$ , based on the following assumptions:

(1) Energy input is the implosion kinetic energy  $K = \frac{1}{2} m v_1^2$ , delivered to the plasma on the hydrodynamic assembly timescale  $t_a = r_1/v_1$ .

(2) Energy loss is by radiation, to which the plasma is transparent above temperature  $T_c$ . The radiated power is modeled by

$$P_{\text{rad}} = P_{\text{BB}} = K_{\text{BB}} r_1 T^4 \text{ for } T < T_c \quad (112)$$

$$P_{\text{rad}} = K_L m^2 r_1^{-2} T^{-0.7} \text{ for } T > T_c.$$

$T_c$  is the value at which the two expressions are equal.

(3) The heating power,  $P_H = \frac{1}{2} m v_1^2 / t_a$ , exceeds the maximum  $P_{\text{rad}}$ , so that  $T$  rises to exceed  $T_c$ .

(4) Energy not radiated is stored in internal energy and in temperature:  $\epsilon = K_e m T$ , with  $\dot{\epsilon} = P_H - P_{\text{rad}}$ . The model, however, appears to give a yield scaling with  $m$ ,  $r_1$ , and  $v_1$  which disagrees with experiments. The model may be misleading in that

(a) it neglects ohmic heating, which continues after assembly and could account for most of the energy input after assembly,

- (b) there is evidence that the energy loss precedes transparency of the plasma; in fact, the plasma is probably never transparent, but nor is it a black body for the dominant lines.
- (c) Continuum radiation is neglected in the  $T > T_c$  domain,
- (d) no account is taken of coronal effects, and
- (e) the single differential equation for  $T$  which results,

$$K_{\epsilon} m \dot{T} = \frac{m}{2} v_1^3 t^{-1} (t < t_a) - P_{\text{rad}}(r, T) \quad (113)$$

assumes a constant-density radiator, i.e., the radiation cooling rate cannot induce contraction.

We have modified this model to include ohmic heating, continuum radiation, and a 'typical' opacity for the line radiation. Coronal effects can be studied in part, through the parameter  $\beta$  in Eqs. 98 and 103. Eqs. 95 - 106 remove the disadvantages just mentioned, but do not give particularly tractable results useful for scaling laws. By taking the assembly heating to be  $\frac{1}{2} m v_1^2 / t_a$  with  $t_a = |r_1| / 2r$ , and eliminating  $r$ , a generalization of Eq. (113) can be derived from (95) - (106):

$$T^{1/3} \dot{T} = K_p K_A r^{-1} T^{4/3} - K_L K_T r^{-1} F_L(T) T^{1/2} - 3 K_B r^{-2} T^{3/2} + K_{\Omega} VI(t) \quad (114)$$

with  $F_L(T)$  approximating the results of Duston and Davis (Ref. 19). Now the assembled radius  $r$  is simply a parameter, as in the Mosher analysis, and not a time-dependent variable with an equation governing its evolution. At the temperatures expected,  $F_L(T)$  is non-monotonic but  $F_L(T) T^{1/2} + 3 K_B r^{-2} T^{3/2}$  may well be. Approximating the assembly and radiation  $T$ -dependence by a single power law, one gets

$$\dot{T} \approx K_1 T + K_2 VI(T) T^{-1/3} \quad (115)$$

with  $K_p K_A r^{-1} T - K_L K_T r^{-1} F_L(T) T^{1/6} - 3 K_B r^{-2} T^{7/6}$  modeled by  $K_1 T$ . The time-dependence of  $I$  is ignored, and  $I$  is taken as a parameter of the problem (hiding its  $T$  dependence). The solution of Eq. (115) for  $k_1 > 0$  is

$$T^{4/3} = \left[ K_2/K_1 + T_1^{4/3} \exp\left(\frac{4}{3} K_1 t\right) \right] - K_2/K_1; \quad (116)$$

with  $K_2 = K_2 VI$ . For  $K_1 < 0$ ,

$$T^{4/3} = K_2/|K_1| - \left[ K_2/|K_1| - T_1^{4/3} \right] \exp\left(-\frac{4}{3} |K_1| t\right) \quad (117)$$

The reference temperature  $T_1$  may be taken small and neglected. Doing so gives

$$T = (K_2/|K_1|)^{3/4} \left[ 1 - \exp\left(-\frac{4}{3} |K_1| t\right) \right]^{3/4} \quad (118)$$

Ordinarily  $K_1$  is negative, and Eq. (118) describes the Ohmic heating to final temperature  $(K_2/|K_1|)^{3/4}$  in the presence of radiative losses, until the assembly heating ceases. Then with  $T$  as a new "initial" temperature  $T_1$ , Eq. (117) with the new  $K_1$  describes the subsequent temperature decay. The central parameter,  $K_2/|K_1|$ , scales as  $8IVm^{-1}|K_1|^{-1}$  with

$$|K_1| = K_L K(T_1) r^{-1} F_L(T_1) T_1^{5/6} + 3K_B r^{-2} T_1^{1/6} - K_p K_A r^{-1} \quad (119)$$

and the remaining coefficients given by Eqs. (97) - (106). From this prescription, the duration for which  $T > T_\theta$  (some threshold temperature) can be calculated, and the radiation yield during that time interval can be calculated from  $T(t)$ . The assembled plasma radius remains as a free parameter, which is the price paid for ignoring its simultaneous evolution.

## REFERENCES

1. D. A. Tidman and D. G. Colombant, "Diode-Imploded Annular Plasmas and Coronal Superheating", JAYCOR Report J78-1069-TC, June 1978.
2. R. Terry and J. Guillory, JAYCOR Semi-Annual Progress Report, Contract DNA001-79-C-0189, 1 August 1979.
3. J. Davis, et. al., NRL Quarterly Progress Report, Jan-Feb-Mar, 1979, on DNA Advanced Concepts Theory and Pulsed Power Advanced Simulation Contracts.
4. J. Davis and V. L. Jacobs (unpublished work, 1978).
5. D. Mosher, NRL Memo Report #3687.
6. D. Duston, J. Davis and K. Whitney, "Effects of Atomic Structure on the Radiation Dynamics of an Optically Thick Plasma", NRL Memo Report #3846, Sept. 1978.
7. J. Apruzese and J. Davis, "Direct Solution of the Equation of Transfer Using Frequency - and Angle-Averaged Photon Escape Probabilities" NRL Memorandum Report #4017, June 21, 1979.
8. J. Apruzese, private communication.
9. J. Katzenstein, "Optimum Coupling of Imploding Loads to Pulse Generators".
10. A. Wilson, et. al., Theory Support of Pulsed Power Experiments, Systems, Science and Software Report SSS-R-79-3948, Feb. 1979.
11. H. W. Bloomberg, et. al., Energy Coupling Mechanisms in Multiple Wire Array Configurations, Science Applications, Inc. Report # SAI-102-72-004, (1979).
12. S. I. Braginskii in Reviews of Plasma Physics, ed. M. A. Leontovich (Consultants Bureau, New York, 1965) (p. 213 ff.)
13. P. C. Kepple, private communication.
14. N. A. Krall and A. W. Trivelpiece, Principles of Plasma Physics, McGraw-Hill, New York, 1973, p. 91.
15. D. G. Colombant and G. F. Tonon, J. Appl. Phys. 44, 3524 (1973).
16. P. Ottinger, J. Guillory, and H. Lashinsky, Phys. Fluids 21, 798 (1978).
17. D. C. Book, E. Ott, and M. Lampe, Phys. Fluids 19, 1982 (1976).
18. J. W. Shearer, Contraction of Z-Pinches Actuated by Radiation Losses Lawrence Livermore Laboratory Report UCRL 77676, Jan. 1976.

19. D. Duston, J. Davis, private communication.
20. B. Lippman et. al., "PI Theoretical Effort", Briefing at NRL, October 1979.

### FIGURE CAPTIONS

Figure 1 - Evolution of the Implicit- $T_2$  Model. The inner, outer core annulus boundaries [b,a] are in (cm), all other quantities are in arbitrary units. The time is in units of the assembly time,  $t_a : b = 0$ .

Figure 2a- Annulus Evolution and Radiated Power in the Explicit- $T_2$  Model. The boundaries [b,a] are in (cm),  $P_{rad}$  is normalized to its maximum.

Figure 2b- Thermodynamic Variables and Circuit Response. All quantities are in arbitrary units.

Figure 3a- Two "initial" ion density profiles for different SPLAT-iD  
3b code runs. Initial temperatures were taken to be 15 eV. The assumed initial current-penetration radius,  $r_i$ , is shown for both.

Figure 4a- Simple collapse (SC) evolution of  $r_i$ ,  $t_m$ , b, I, and  $P_{rad}$ . Insert shows the relation of  $P_{rad}$  to ion temperature and spatially averaged ion density.

Figure 4b- Pause-and-collapse (PC) evolution of  $r_i$ ,  $r_m$ , b, I, and  $P_{rad}$ . Insert shows the relation of  $P_{rad}$  to ion temperature and spatially averaged ion density.

Figure 5 - Generator voltage vs time for  $\alpha = 1.2$  (1.2 x faster than normal pulse).

Figure 6 - Frequency-integrated radiative yield vs generator rise-rate multiplier  $\alpha$ , for three initial configurations: (a) that of Fig. 3a, (b) that of Fig. 3b, and (c) a smaller radius array with peak at 0.3 cm and width 0.1 cm, but the same mass as 3a and 3b.

DISTRIBUTION LIST

DEPARTMENT OF DEFENSE

Assistant to the Secretary of Defense  
Atomic Energy  
ATTN: Executive Assistant  
ATTN: Military Applications

Defense Intelligence Agency  
ATTN: JT-1B, R. Rubenstein

Defense Nuclear Agency  
ATTN: RAAE  
ATTN: RAEV  
ATTN: STNA  
ATTN: RAEF  
4 cy ATTN: TITL

Defense Tech Info Ctr  
12 cy ATTN: DD

Field Command Defense Nuclear Agency  
Det 1  
Lawrence Livermore Lab  
ATTN: FC-1

Field Command  
Defense Nuclear Agency  
ATTN: FCPR  
ATTN: FCTT, W. Summa  
ATTN: FCTT  
ATTN: FCTXE  
ATTN: FCTT, G. Ganong

Under Secretary of Defense for Rsch & Engrg  
ATTN: Strategic & Space Sys (OS)

DEPARTMENT OF THE ARMY

Harry Diamond Labs  
ATTN: DELHD-NW-P, 20240  
ATTN: DELHD-NW-RA, 22100  
ATTN: DELHD-NW-RI, Kervis, 22900  
ATTN: DELHD-TA-L, 31100

JS Army Nuclear & Chemical Agency  
ATTN: Library

JS Army Test and Evaluation Comd  
ATTN: DRSTE-EL

JSA Missile Command  
ATTN: Doc Section

DEPARTMENT OF THE NAVY

Naval Rsch Lab  
ATTN: Code 2000, J. Brown  
ATTN: Code 4770, I. Vitokovitsky  
ATTN: Code 4720, J. Davis  
ATTN: Code 4780, S. Ossakow  
ATTN: Code 4773, G. Cooperstein

Naval Surface Weapons Ctr  
ATTN: Code R40  
ATTN: Code F31  
ATTN: Code F34

DEPARTMENT OF THE NAVY (Continued)

Naval Weapons Ctr  
ATTN: Code 343, FKA6A2, Tech Svcs

DEPARTMENT OF THE AIR FORCE

Air Force Weapons Lab  
ATTN: SUL  
ATTN: CA  
ATTN: NYTC  
ATTN: NT  
ATTN: NTYP

Ballistic Missile Ofc  
ATTN: ENSN  
ATTN: SYDT

Deputy Chief of Staff  
Rsch, Dev, & Acq  
ATTN: AFRDQI

Space Div  
ATTN: XR, Plans  
ATTN: YEZ  
ATTN: YGJ  
ATTN: YKF  
ATTN: YKS, P. Stadler  
ATTN: YKM  
ATTN: YNV

Strategic Air Command  
ATTN: INT, E. Jacobsen

DEPARTMENT OF ENERGY

Department of Energy  
Office of Military Application  
ATTN: Ofc of Inert Fusion, S. Kahalas  
ATTN: Ofc of Inert Fusion, T. Godlove  
ATTN: Ofc of Inert Fusion, C. Hilland

OTHER GOVERNMENT AGENCY

Central Intelligence Agency  
ATTN: OSWR/NED

DEPARTMENT OF ENERGY CONTRACTORS

University of California  
Lawrence Livermore National Lab  
ATTN: Tech Info Dept, Library  
ATTN: L-545, J. Nuckolls  
ATTN: L-47, L. Wouters  
ATTN: L-153  
ATTN: L-153, D. Meeker  
ATTN: W. Pickles, L-401

Sandia National Lab  
ATTN: G. Yonas  
ATTN: Tech Lib, 3141  
ATTN: J. Powell  
ATTN: M. Clauser, Org 5241  
ATTN: G. Kuswa, Org 5240  
ATTN: D. Allen, Org 9336

DEPARTMENT OF ENERGY CONTRACTORS (Continued)

Los Alamos National Lab  
ATTN: MS222, J. Brownell

DEPARTMENT OF DEFENSE CONTRACTORS

Advanced Research & Applications Corp  
ATTN: R. Armistead

Aerospace Corp  
ATTN: V. Josephson  
ATTN: S. Bower  
ATTN: Tech Info Svcs

BDM Corp  
ATTN: Corporate Library

BDM Corp  
ATTN: L. Hoeft

Boeing Co  
ATTN: Aerospace Library

Dikewood  
ATTN: Tech Lib for L. Davis

EG&G Wash Analytical Svcs Ctr, Inc  
ATTN: Library

General Electric Co  
ATTN: J. Peden  
ATTN: H. O'Donnell

IRT Corp  
ATTN: R. Mertz

JAYCOR  
ATTN: E. Wenaas

JAYCOR  
ATTN: E. Alcaraz  
ATTN: R. Sullivan  
4 cy ATTN: J. Guillory  
4 cy ATTN: R. Terry

Kaman Sciences Corp  
ATTN: S. Face

Kaman Tempo  
ATTN: DASIAC

DEPARTMENT OF DEFENSE CONTRACTORS (Continued)

Lockheed Missiles & Space Co, Inc  
ATTN: L. Chase

Lockheed Missiles & Space Co, Inc  
ATTN: S. Taimuty, Dept 81-74/154

Maxwell Labs, Inc  
ATTN: A. Koib  
ATTN: D. Tanimoto  
ATTN: A. Miller  
ATTN: D. Cole

McDonnell Douglas Corp  
ATTN: S. Schneider

Mission Rsch Corp  
ATTN: W. Hart  
ATTN: C. Longmire

Mission Rsch Corp  
ATTN: B. Godfrey

Mission Rsch Corp, San Diego  
ATTN: B. Passenheim

Pacific-Sierra Rsch Corp  
ATTN: H. Brode, Chairman SAGE  
ATTN: L. Schlessinger

Physics International Co  
ATTN: C. Gilman  
ATTN: C. Stallings  
ATTN: G. Frazier

R & D Associates  
ATTN: P. Hias  
ATTN: A. Latter

R & D Associates  
ATTN: P. Turchi

S-CUBED  
ATTN: A. Wilson

Sciences Applications, Inc  
ATTN: K. Sites

TRW Electronics & Defense Sector  
ATTN: Tech Info Ctr  
ATTN: D. Clement

**DAT  
ILM**